NOVEL DESIGN STRATEGIES TO REDUCE THE FOREIGN BODY RESPONSE TO CENTRAL NERVOUS SYSTEM IMPLANTS

by

John Lawrence Skousen

A dissertation submitted to the faculty of
The University of Utah
in partial fulfillment of the requirements for the degree of

Doctor of Philosophy

Department of Bioengineering

The University of Utah

May 2013

The University of Utah Graduate School

STATEMENT OF DISSERTATION APPROVAL

The dissertation of **John Lawrence Skousen**

has been approved by the following supervisory committee members:

Patrick Tresco	, Chair	**08/01/2012** Date Approved
Richard Normann	, Member	**08/01/2012** Date Approved
Ian Harvey	, Member	Date Approved
Robert Hitchcock	, Member	**08/01/2012** Date Approved
Bradley Greger	, Member	**08/01/2012** Date Approved

and by **Patrick Tresco**, Chair of the Department of **Bioengineering**

and by Charles A. Wight, Dean of The Graduate School.

ABSTRACT

Multiple studies have shown the potential for using implantable microelectrode arrays to record consciously modulated neural signals and to restore volitional control of external devices to patients suffering from various nervous system and motor disorders. However, despite the promising potential of this technology, achieving widespread clinical application requires improving recording consistency and quality over a clinically relevant time frame.

There is near consensus in the field that the foreign body response (FBR) that the brain mounts against implanted devices contributes to the observed recording instability. Available evidence suggests that pro-inflammatory and cytotoxic soluble factors secreted by reactive macrophages/microglia at the device-tissue interface mediate the cellular-level changes underlying the FBR. Based on this assumption, we hypothesize that implant designs that passively reduce the activation of these cells and the concentrations of their released soluble factors surrounding the implant will reduce the severity of the FBR.

To explore this hypothesis we have studied the FBR to a series of novel test devices based on single-shank, Michigan-style microelectrode arrays. These devices have modified architectures and altered constitutive properties intended

to reduce macrophage activation and/or the impact of their secreted factors. To facilitate the design and testing of these devices, we first created a series of three-dimensional (3-D) finite element simulations to predict the distributions of various macrophage-secreted factors around virtual device designs with altered architectures and permeability (Chapter 2). Building on predictions from these models, we have tested the efficacy of reducing the amount of device surface area presented for macrophage interaction/activation in altering the brain FBR (Chapter 3). Furthermore, we also examined the efficacy of increasing device permeability in altering the brain FBR by incorporating coatings that serve as cytokine sinks to passively absorb pro-inflammatory factors into the device and away from adjacent brain tissue (Chapter 4). In the final portion of this dissertation we move from these passive methods of limiting the extent and impact of activated inflammatory cells and describe the creation of extracellular matrix (ECM) based device coatings to bioactively reduce the FBR and drive improved healing and integration into tissue (Chapter 5).

TABLE OF CONTENTS

LIST OF ABBREVIATIONS

3-D	Three-Dimensional
BBB	Blood Brain Barrier
BCI	Brain Computer Interface
BMI	Brain Machine Interface
CA-1	Cornu Ammonis 1
CD-68	Center of Differentiation-68
CNS	Central Nervous System
CSF	Cerebral Spinal Fluid
DBS	Deep Brain Stimulation
DG	Dentate Gyrus
ECM	Extracellular Matrix
FBR	Foreign Body Response
GFAP	Glial Fibrillary Acidic Protein
IBA-1	Ionized Calcium Binding Adaptor Molecule 1
MCP-1	Monocyte Chemotractant Protein-1
MEA	Michigan Electrode Array
MS	Multiple Sclerosis
PU	Polyurethane
SCI	Spinal Cord Injury
TBI	Traumatic Brian Injury
TNF-α	Tumor Necrosis Factor – alpha
UEA	Utah Electrode Array

ACKNOWLEDGMENTS

I would like to acknowledge my advisor, Dr. Patrick Tresco, who provided tremendous guidance and financial support during my graduate studies. I also want to thank my advisory committee members: Dr. Richard Normann, Dr. Bradley Greger, Dr. Robert Hitchcock and Dr. Ian Harvey for their support as well as their insightful suggestions and questions that have improved this work and pushed me forward. Additionally, I would also like to thank other members of the Keck Center for Tissue Engineering for their help and support during my studies including Dr. Fan-Wei Meng, Dr. Jeff Wolchock, Dr. Brent Winslow, Dr. Elena Budko, Dr. Braden Leung, Dr. Ben Christiansen, Robert Oakes, Nick Nolta as well as the many undergraduates and high school students who have come through the lab as volunteers. Finally, I would like to thank my family for their support including my parents, Don and Carol Skousen. I especially want to express my gratitude for my fantastic wife and editor Laura (and our crazy dog Pepper) for putting up with everything that comes along with graduate school and research over the years and helping me to pursue my goals and interests.

CHAPTER 1

INTRODUCTION

1.1 The impact of CNS injures, diseases and disorders

Diseases and disorders of the central nervous system (CNS) as well as traumatic injury of these structures are among the most debilitating conditions afflicting patients in our healthcare system. Among these conditions are a number of neurodegenerative conditions such as Parkinson's disease, Alzheimer's disease and multiple sclerosis (MS) that affect over five million patients in the US [1-9]. Congenital disorders such as hydrocephalous, a buildup of excess cerebral spinal fluid (CSF) in the brain, affect over 700 thousand patients [10, 11]. Additionally traumatic brain injury (TBI) and spinal cord injury (SCI) impact over five million [12-14] and 250 thousand patients, respectively [15, 16]. Each of these injured populations and their families has physical, social and emotional components of their lives affected through resulting conditions such as dementia, incontinence, or partial to full paralysis. Combined, these conditions directly impact over 50 million individuals in the US alone with an annual impact of over $400 billion to our economy when direct costs and indirect costs such as lost wages and productivity are taken into account. Table 1-1 summarizes the causes of these conditions and their subsequent impact.

Table 1-1: Overview of common CNS related conditions.

Condition	Population Size	Estimated Direct & Indirect Costs	Causes & Pathology
Parkinson's	350k	$24B	Loss of dopamine-secreting cells
Alzheimer's	5M	$100B	Accumulation of Beta-amyloid protein
MS	350k	$7B	Myelin degradation and white matter deterioration
Hydrocephalous	700k	$1B	Ventricular accumulation of CSF
TBI	5M	$76B	Traumatic injury to various brain regions
SCI	250k	$65B	Traumatic injury to various spinal cord structures

Related Symptoms	Current & Experimental Treatment Options	References
Tremor, rigidity, and bradykinesia	Various medications and deep brain stimulation	[1-3, 17-20]
Cognitive and memory deterioration, dementia, insominia	Various medications	[4-6, 21-27]
Muscle weakness and spasm, bowel dysfunction, vision loss	IFB-1a injections and infusions of Natalizumab	[7-9, 28-34]
Elev. intracranial pressure, herniation, CNS degradation and death	Drainage shunting	[10, 11, 35-41]
Various physical, cognitive, social, and emotional effects	Hemostatic agents as well as regenerative medicine techniques	[12-14, 42-45]
Full to partial paralysis below injury site	Enzymatic cleavage of inhibitory molecules as well as bridging devices	[15, 16, 46]

1.2 Medical devices and biomaterials used in CNS treatments

With such a large impact on both the direct patient population as well as our economy, a number of medical devices and therapeutics have been commercialized or are currently under investigation and development for treating CNS diseases and disorders. Of these devices, deep brain stimulation (DBS) electrodes are one of the most commercially and clinically successful devices to date with over 35,000 devices having been implanted worldwide. Deep brain stimulating devices are commonly used in the treatment of motor dysfunction associated with Parkinson's disease. These devices are composed of a bilateral array of stimulating electrodes that are placed in the thalamus or basal ganglia and are connected to an impulse generator that is generally placed below the clavicle or in some cases, the abdomen. DBS electrodes are also being investigated for use in treating chronic pain [47], obesity, depression [48] and obsessive-compulsive disorder [48]. Treatment of other conditions entails shifting the leads to other brain regions such as the periaqueductal gray matter for treating nociceptive pain, and the internal capsule or ventral posterolateral nucleus for treating neuropathic pain.

Another set of clinically approved devices for CNS treatments are drainage shunts used to divert excess CSF from the brain of hydrocephalous patients. Shunts have changed little since their original design in 1955. These devices consist of three main components: a ventricular catheter placed in the ventricles, a one-way valve to control pressure within the brain and lastly, a distal

catheter to divert the excess CSF to an alternative cavity in the body such as the abdomen [36, 49].

Perhaps the ultimate goal of SCI injury treatment is to develop spinal cord bridging devices. These devices are intended to induce and guide the repair and regeneration of injured spinal cord tissues with the end goal of restoring normal function to SCI patients. Devices that have been investigated for this purpose include aligned polymer fibers, and more recently, engineered cell and extracellular matrix (ECM) constructs [50-59]. While a number of these types of devices have been used to improve functional regeneration through short peripheral nerve gaps, they have shown little success at improving functional regeneration in the damaged spinal cord.

An alternative area of research focused on restoring some level of independence to both patients suffering from SCI as well as limb amputation is the field of brain machine or brain computer interfaces (BMIs or BCIs, this first designation will be used throughout this manuscript). In these applications, a recording device is used to extract volitional intent in the form of consciously modulated neuronal signals from healthy portions of the nervous system. Using a variety of signal processing algorithms these signals can then be used to drive an external device such as a neuroprosthesis or a computer [60-62].

While functional information can be gained by nonpenetrating recording electrodes placed externally on the scalp or subdurally on the brain surface [63], many researchers believe that recording devices that penetrate into specific regions of nervous tissue will likely provide the most useful control signals for

these types of systems. A number of devices have been designed for this purpose, including insulated microwires and microwire arrays which consist of insulated wires with exposed conducting tips for electrical interaction with the surrounding tissue [64, 65], and silicon based systems such as the Utah Electrode Array (UEA) that consists of an array of insulated doped silicon tines with exposed recording tips [66, 67] and the Michigan-style electrode array (MEA) which is an insulated planar array with multiple exposed recording sites located along a planar silicon shank [68-70]. Figure 1-1 offers examples of these penetrating microelectrode-recording devices.

1.3 Biocompatibility concerns of current and investigational treatments

While a number of the devices discussed above are used clinically there is room for improvement and innovation with all of these devices. One of the largest areas where engineers and developers can improve is device biocompatibility.

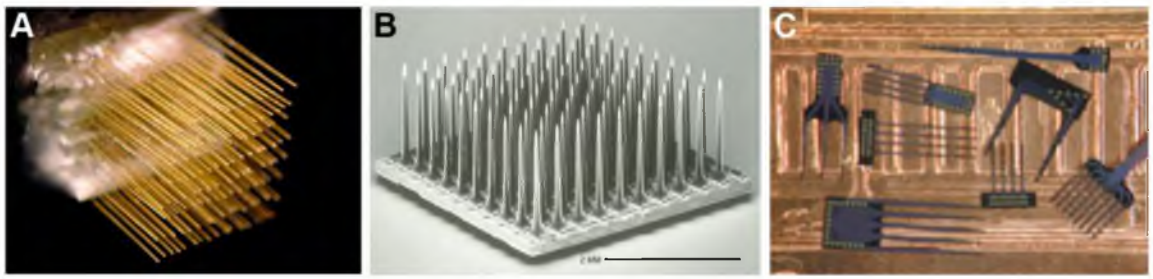

Figure 1-1: Representative images of a variety of microelectrode recording arrays including (A) a microwire array similar to those produced by FHC and other companies, (B) a 10x10 UEA produced by Blackrock Microsystems and (C) a variety of single and multi-shank planar MI-style devices made by Neuronexus now a subsidiary of Big Batch Incorporated.

The most widely cited definition of biocompatibility originated at the 1986 consensus conference on biomaterials held in Chester, UK. Under this definition biocompatibility is: "the ability of a material to perform with an appropriate host response in a specific application." This definition first refers to the requirement that the device is able to perform its designed function over the intended lifetime of the device. Secondly, this definition requires that the device not elicit an inappropriate host response in a given application that outweighs the intended function of the device. A new standard of biocompatibility has arisen with the increased understanding that we now have about the local and systemic impact of the host response as well as insights into how to modify this response. Ratner in his *Biocompatibility Manifesto* put forth a new definition for this critical device attribute in which he states that biocompatibility in a large number of cases may be better defined by clarifying the appropriate host response as "non-fibrotic wound healing, reconstruction and tissue integration [71]." Along with this refined definition, Ratner also proposed a new alternative classification, that of biotolerability, which describes the traditional set of chronic inflammation, fibrous encapsulation and other associated responses that we have observed around traditional devices used in the clinic today.

All devices used for treating CNS diseases induce chronic inflammation at the device/tissue interface and become encapsulated in fibrous tissue. Together these host responses to chronic device implantation are termed the foreign body response (FBR). This FBR can lead to both device dysfunction as well as other undesired local and systemic host responses that may outweigh the benefits of

device implantation. For example, a number of groups have shown that the fibrous encapsulation of DBS electrodes induces increased tissue impedance, which may limit device function over time and may necessitate premature device removal [72-80]. The biocompatibility of these devices comes into question further based on evidence indicating that chronic inflammation associated with DBS implantation leads to cognitive deficits in DBS recipients compared to those who do not receive a DBS [81-85]. While the risk benefit ratio of these devices may be acceptable to some patients and their physicians, it is clear that methods to reduce the FBR to these devices and improve their biocompatibility would be desirable.

Another set of devices with major biocompatibility concerns are hydrocephalous shunts. A staggering 40% of shunts become nonfunctional within two years after placement necessitating device replacement [86]. While device-associated infections do account for a portion of these failures, by and large the majority of failures are due to FBR related obstruction and occlusion of the drainage path [36, 87-90]. Beyond directly impacting device function, the impact of the FBR is further amplified as the shunt-associated FBR also has been implicated in observed long-term cognitive deficits in shunt recipients [91-93].

Beyond these clinically approved devices, a number of investigational devices have had their success and path to clinical application hampered by the FBR. For example, a number of methods have been investigated for spinal cord injury repair [50-59]. However, nearly all of these methods have failed to achieve reproducible and functional SCI repair. These failures have been attributed to the

inflammatory FBR that prevents direct neuronal contact with generally haptic mediated guidance cues.

1.4 The biocompatibility of microelectrode arrays

Numerous studies have shown that using implanted microelectrode arrays, consciously modulated neural signals can be recorded in both animal subjects as well as human patients for periods of time ranging from months to multiple years, and that these recorded signals can be used to control a number of external devices [94-97]. Figures 1-2 and 1-3 give a historical summary of the longest recording durations reported in the literature for various types of implant as well as various animal models, respectively. Despite these promising results, achieving widespread clinical application of this technology requires both increasing the overall recording lifetime to a clinically relevant time frame as well as improving recording quality and consistency to maximize the amount of useable information extracted for neural interface applications [98-102].

A recent conference report by Baresse et al. as well as, yet unpublished, findings from our lab suggest that there are two major failure mechanisms limiting the overall lifetime of these devices [103]. These mechanisms include mechanical failures of the wire bundles and head stages currently used on commercially available devices as well as loss of integrity in the devices' insulating layer(s). Further development and adoption of reliable wireless recording technology should prove a key first step in limiting mechanical failures of wire bundles and mounted head stages. To address the loss of insulation integrity there are two pathways where designers could focus their efforts. These

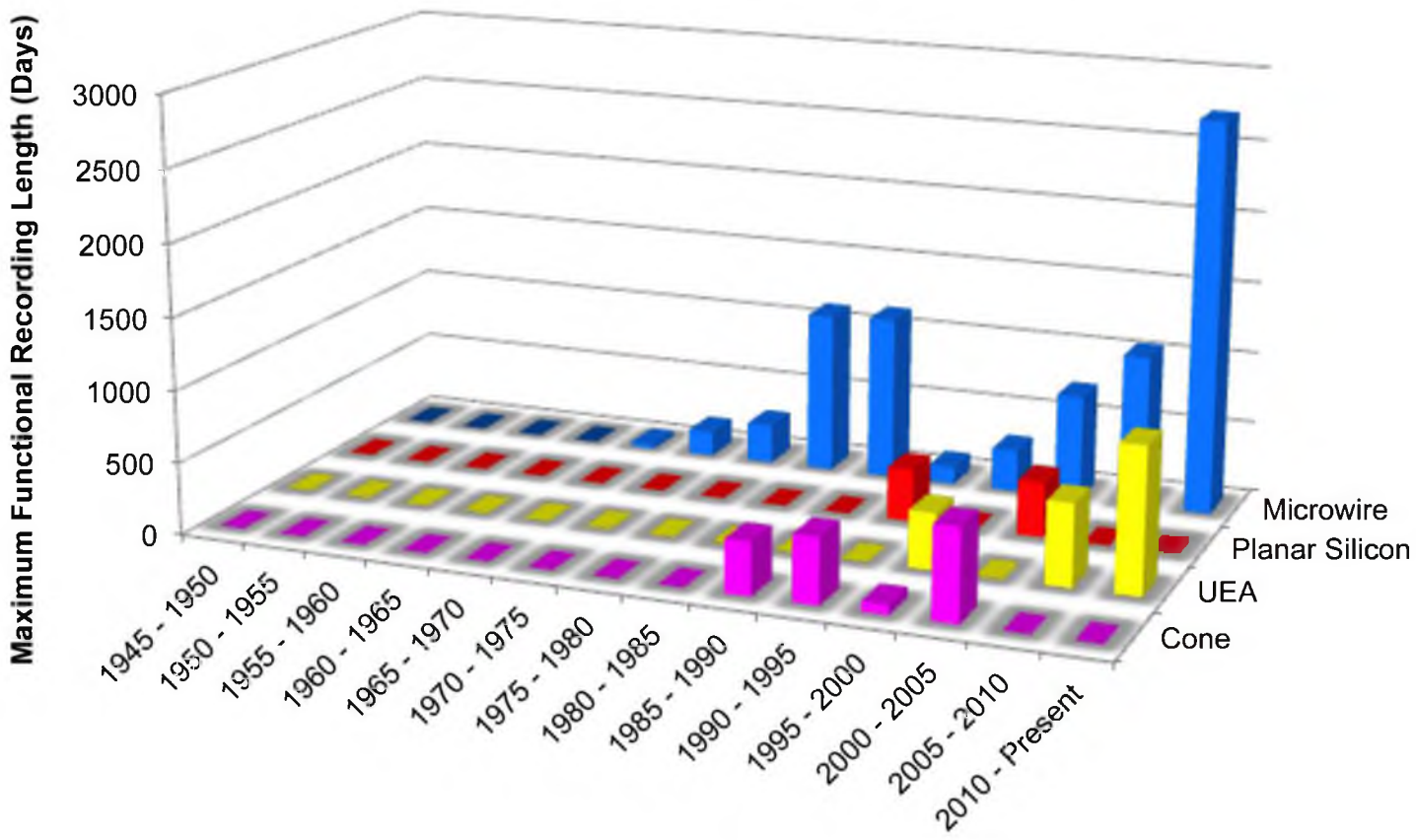

Figure 1-2: Maximum recording longevity reported in the literature for various electrode types by half decade. Longevity refers to the ability of at least one channel in any given device to record compound action potentials.

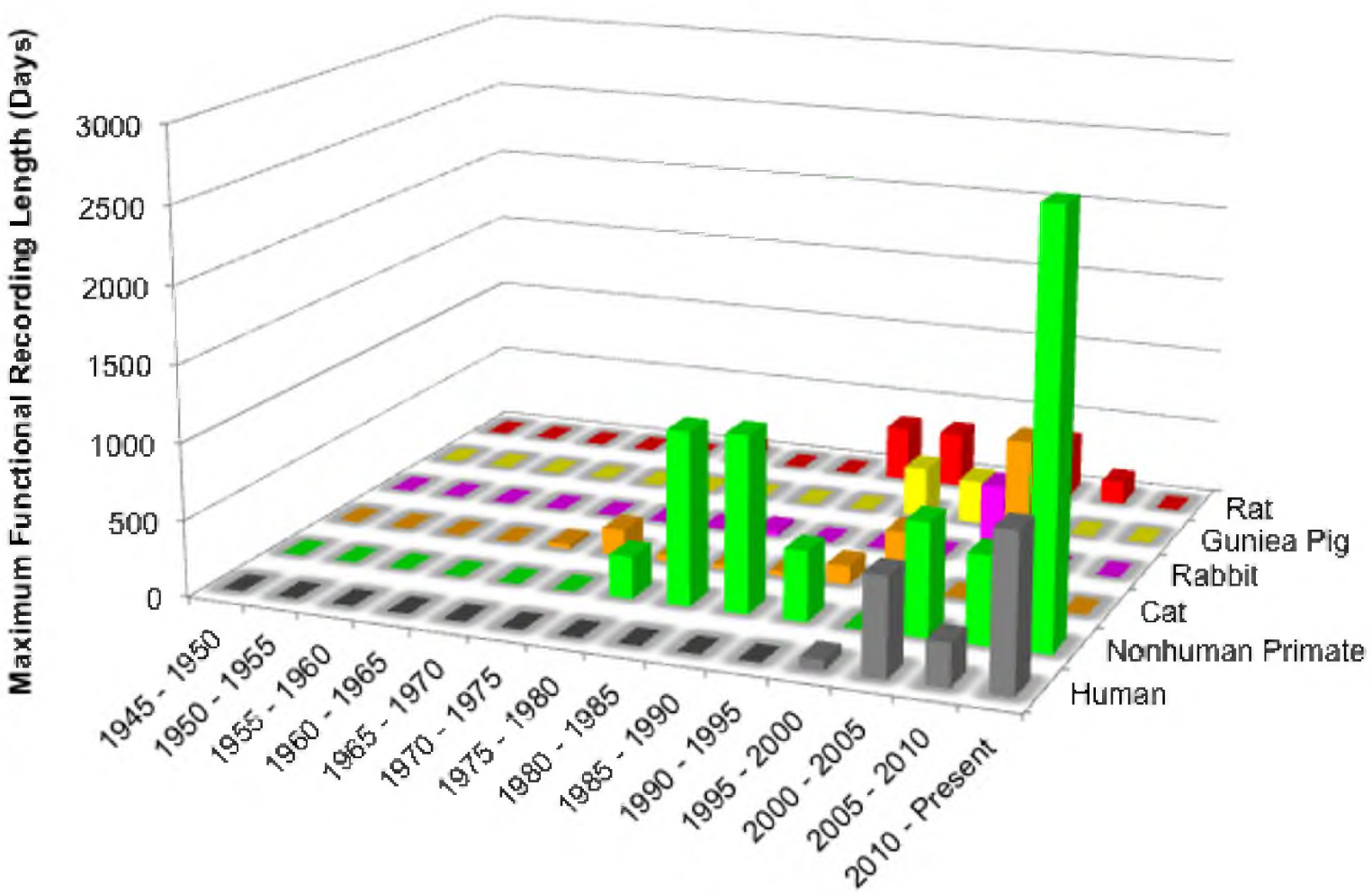

Figure 1-3: Maximum recording longevity reported in the literature for various animal models or successful human trials. The longest recording durations have been reported in large animal models such as non-human primates and human patients.

involve either developing insulating materials that can withstand the harsh *in vivo* environment created by the brain FBR (extremely low local pH and high concentrations of oxidizing agents) or developing new devices that limit the FBR itself to reduce these harsh conditions to a point where traditional materials will suffice.

With regards to recording consistency and quality, the correlation between the FBR and device function remains unclear. However, there is increasing evidence suggesting that the FBR may be a primary hurdle that we need to overcome to improve the average quantity and usefulness of the signals we are recording. Rennekar et al. first demonstrated the correlation between the FBR on recording consistency by examining the effects of minocycline administration on the quality and longevity of chronic multi-channel microwire neural implants in rat auditory cortex [104]. Minocycline, a tetracycline derivative, is an anti-inflammatory drug known to down regulate macrophage activation and has been shown to have neuroprotective and neurorestorative effects in a number of inflammatory models. In control animals the authors observed a decrease in mean cohort signal to noise ratio (SNR) over the first month of implantation as well as a reduction in the number of channels that detected driven single unit activity. In contrast, rats that received an oral minocycline treatment showed a significant improvement in both SNR and the number of channels that recorded stimulus-driven activity.

Based on the role the FBR appears to play in both long-term performance as well as recording consistency/quality, understanding this set of responses and

developing techniques to reduce them are critical to achieving the promise of BMI technology. Over 65 years of studies have described consistent, stereotypic features of the brain FBR that occur irrespective of the type of implant, species studied, or implantation method [105]. Figures 1-4 and 1-5 give a historical summary of this FBR literature by breaking down where this information comes from based on type of implant as well as animal model. Figure 1-6 shows representative images of the stereotypic organization of the FBR to implanted planar MI-style electrodes and cylindrical microwire devices.

Due to the dense and, in many cases, highly vascularized nature of nervous tissue, medical device implantation inevitably causes injury. Following this initial iatrogenic injury, a number of acute cascades and processes are initiated to induce wound closure and promote tissue remodeling. The initial event is initiation of the coagulation cascade to form a provisional matrix in the area of damage and restore vascular integrity [106]. During this period of time a number of other events ensue including activation of the complement system, which can induce cell death through formation of the membrane attack complex as well as initiate local inflammatory events through the alternative arm of the cascade [107]. While much is known about these events and their role in injury and device implantation models, in other tissue compartments and with other devices, to date there has been little effort to describe these events for microelectrodes implanted in the CNS. The majority of what we know about the FBR to implanted microelectrodes has focused on later time points ranging from 1-16 weeks post-implantation and has come from end-point histological examination.

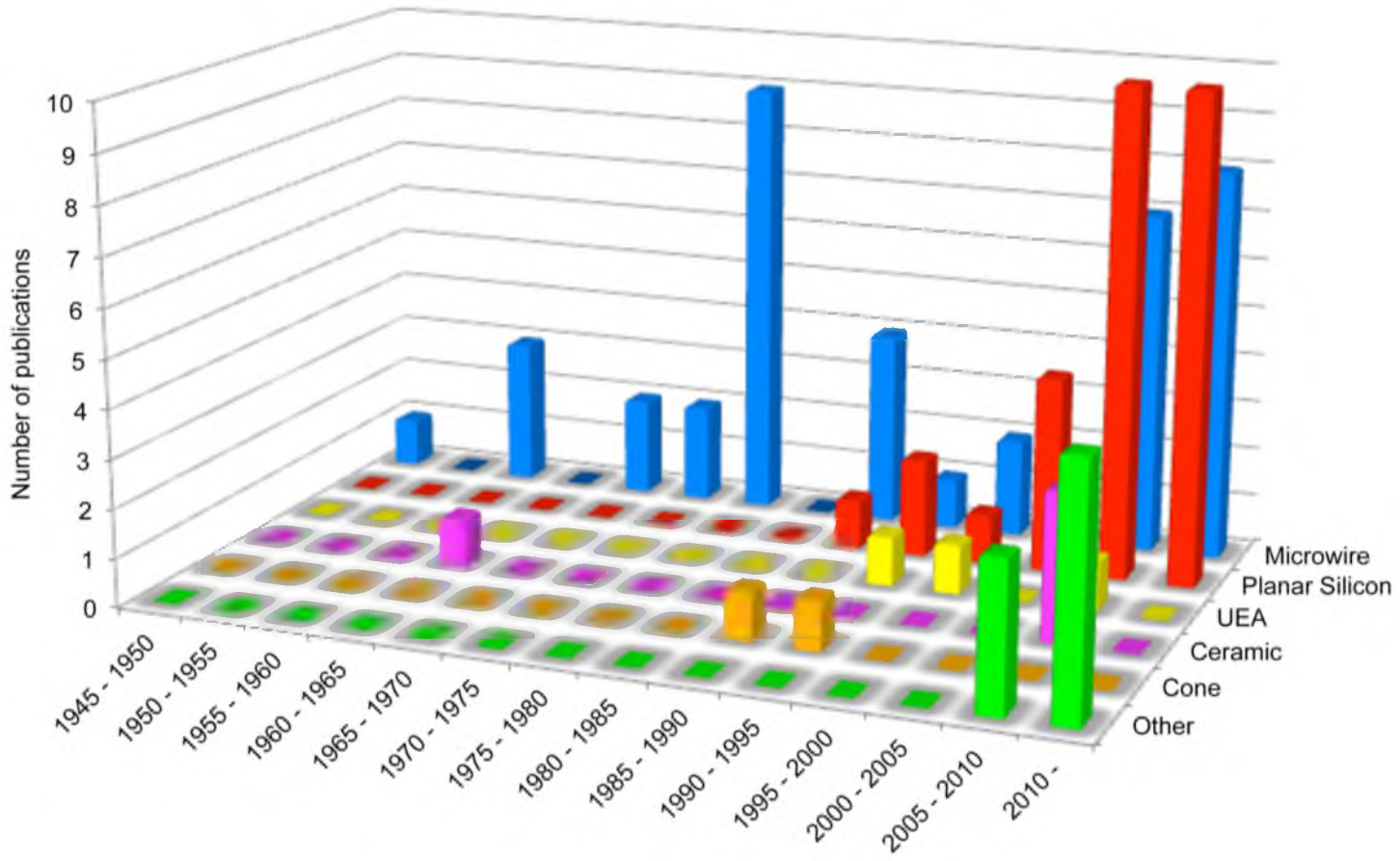

Figure 1-4: Historical breakdown of the electrode FBR literature (88 sources), by electrode type and half decade. Microwires have had the most consistent analysis over time. However, there has been a surge of interest in the FBR to planar MI-style microelectrodes in recent years.

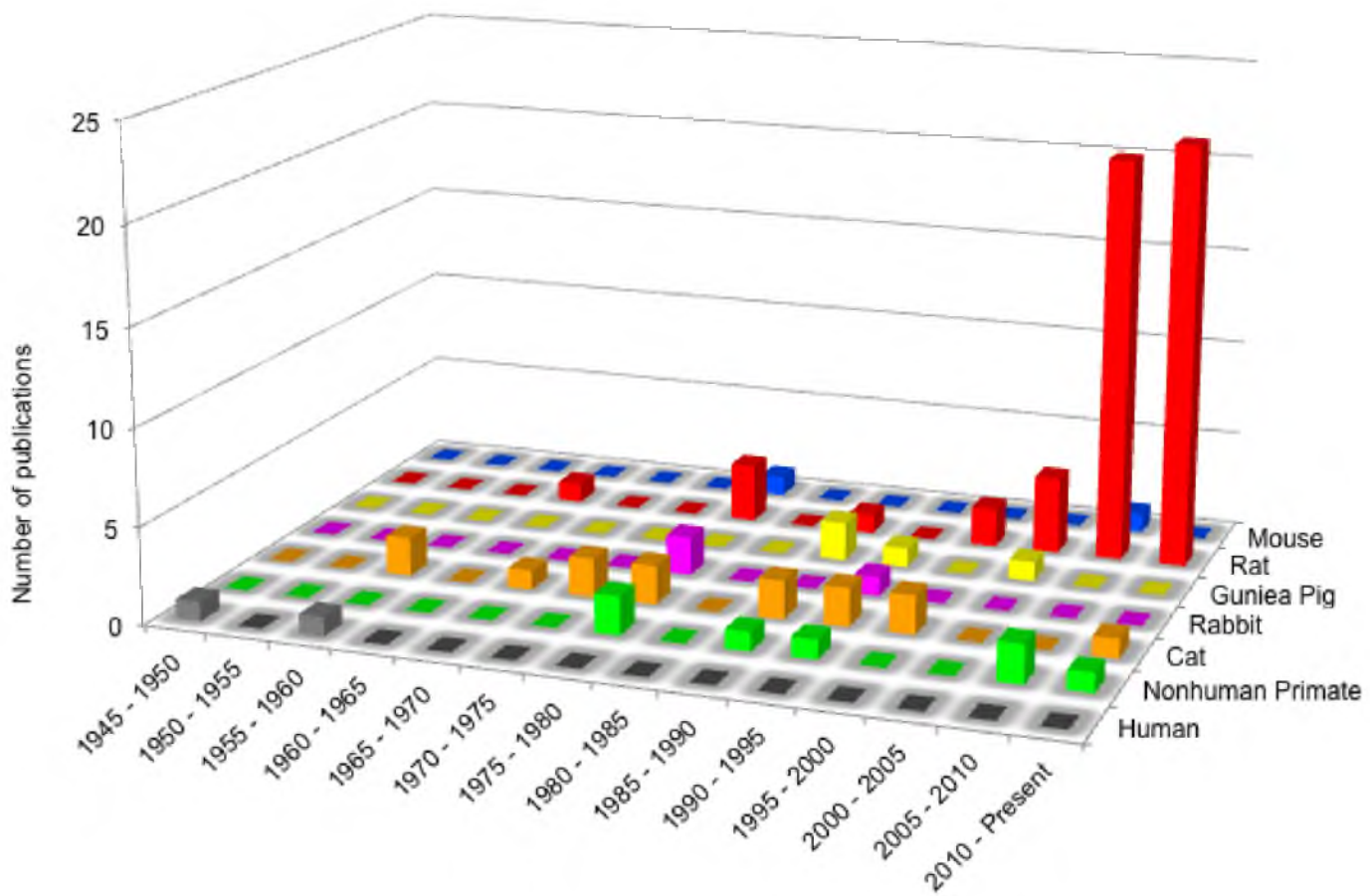

Figure 1-5: Historical breakdown of the electrode FBR literature (88 sources), by animal model and half decade. An overwhelming majority of recent studies have been performed in rat models. This is an interesting trend as almost all studies describing recording over extended durations have been performed in larger animals such as nonhuman primates or in human patients.

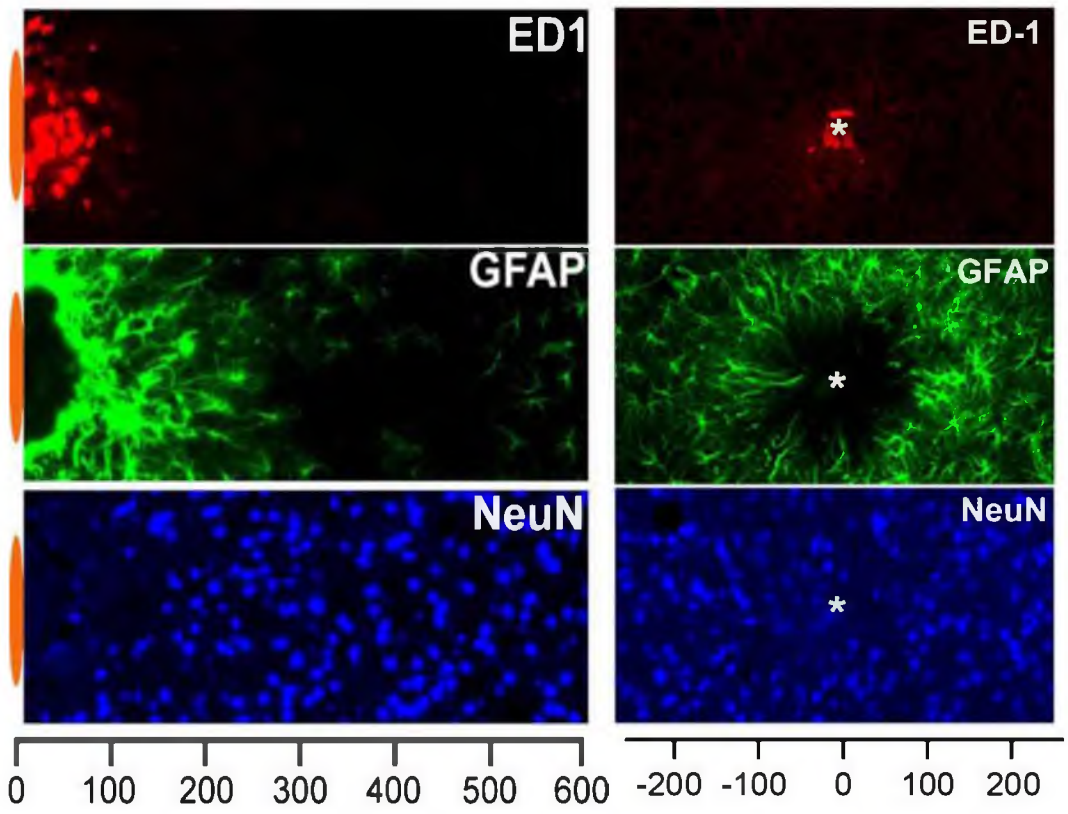

Figure 1-6: Representative images depicting the stereotypic organization of the brain FBR surrounding a planar MI-style microelectrode (left) and a cylindrical microwire (right) after four and 12-week implantation periods respectively. The response to both styles of devices is characterized by activated microglia/macrophages (CD-68) at the device interface surrounded by a minimally overlapping layer of hypertrophic astrocytes (GFAP). This gliotic region also contains a reduced number of NeuN+ neuronal cell bodies. The distance shown on scale bars beneath the images is in microns. Only one side of the response to the planar MI-style microelectrode is shown. Adapted from Biran et al. 2005 and Winslow and Tresco 2010 [108, 109].

Similar to the response in the rest of the body, a key feature of the brain FBR is persistent inflammation at the biotic-abiotic interface signaled by biomarkers (such as CD-68) for activated microglia and extravasated blood-born macrophages [108-111]. These cells play a primary role in phagocytizing damaged or dead cells and clearing residual debris left from the initial iatrogenic injury as well as subsequent chronic events [112]. Following phagocytosis, these cells are known to act as antigen presenting cells in a variety of disease and pathological states [113-118]. While yet unproven, this body of knowledge indicates that ongoing macrophage trafficking to and from the vasculature system may perpetuate blood brain barrier dysfunction and provide a persistent stimulus for the FBR via extravasated fibrinogen, complement factors and other blood products, which adsorb to the device surface.

In addition, multiple studies have shown that activated microglia and macrophages release a plethora of pro-inflammatory/cytotoxic molecules, which can damage healthy bystander cells such as neurons [108, 119-124]. Furthermore, previous work from our lab has shown that adherent-cells, retrieved on explanted devices secrete both tumor necrosis factor-alpha (TNF-α) and monocyte chemotactic protein-1 (MCP-1, Figure 1-7) [108]. TNF-α can have direct toxic effects on neurons and oligodendrocytes; while, MCP-1 is a chemokine involved in opening the blood brain barrier (BBB) and recruiting new macrophages to sites of injury and inflammation [119, 120, 124-132].

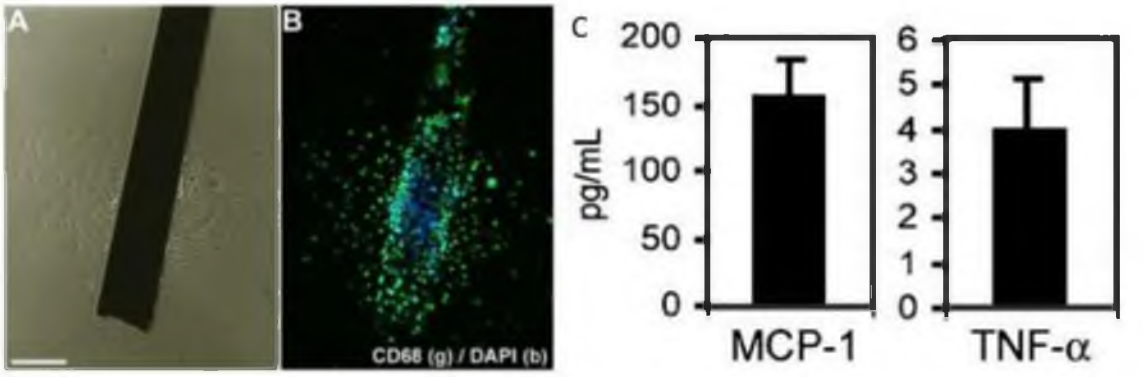

Figure 1-7: (A) Representative phase-contrast image of an explanted microelectrode after one week of culture shows cells with a migratory phenotype. (B) Fluorescence image for the same panel as (A) showing that the majority of these cells are CD68+(green) macrophages. (C) Representative data (mean + SEM) of MCP-1 and TNF-α concentrations in conditioned medium harvested from explanted microelectrodes after the first 24hrs following retrieval in serum-free culture. Scale bar = 200μm. Adapted from Biran & Tresco 2005 [108].

Surrounding this inflammatory core, a region consisting of hypertrophic astrocytes as well as infiltrating fibroblasts and meningeal cells has been observed [105, 108-111, 133-140]. In healthy brain tissue, astrocytes regulate the local microenvironment by sequestering a number of neurotransmitters and ions as well as maintaining the BBB, isolating the cellular and ionic milieu of brain and supporting vasculature from one another [141-144]. Following injury, astrocytes increase the number and size of their cellular processes. These hypertrophic astrocytes are believed to play a similar role to that of reactive fibroblasts in the FBR in other tissue compartments, where they create a dense scar-like layer that limits volume transmission [145]. Many believe that this diffusion barrier may play a beneficial role in restricting the impact of macrophage secreted factors on the surrounding tissue [146-149]; however, it may also

increase the tissue's impedance to small ion transport, potentially limiting recording function.

Associated with this region of inflammation and reactive gliosis, studies also have described a decrease in the local nerve fiber and neuronal cell body densities surrounding implanted devices [105, 108, 136, 140]. While a significant number of neurons remain within the recording range of these devices, the overall decrease in neuronal density (approximately 50-60%) indicates that the environment may no longer be ideal for promoting neuronal health and function. Clearly any compromise of this target cell population may influence device function.

From quantitative work performed in our lab, we know that this chronic inflammation and neuronal loss are associated with the continual presence of the implant and are not solely a result of iatrogenic injury related to device implantation as we have shown that these phenomena do not accompany stab wound injuries made with identical recording devices [108].

In recent years we have gained further insight into the time course of the FBR. Recent studies from our lab examined the time course of the FBR to both planar MI-arrays and single microwires at 2, 4 and 12 weeks post-implantation [109, 111]. These studies showed activated macrophages present at all time points regardless of microelectrode type. This finding is further corroborated by the presence of activated macrophages surrounding DBS electrodes up to 2 years postimplantation [73-80, 150]. We did observe changes in the spatial distribution of these inflammatory cells over time, with a more dispersed,

activated macrophage distribution at 2 weeks compared to both 4 and 12 weeks. We observed no progression in the spatial distribution of reactive astrocytes or neuronal loss as a function of time over this indwelling period. These findings do not support several previous FBR associated recording failure mechanisms, including progressive increases in astrocyte encapsulation or progressive neuronal loss within the recording zone.

New observations from our lab have opened other potential explanations as to how the FBR could influence recording. As observed in many neurodegenerative disorders, we have found that the local BBB and myelin integrity are compromised in the tissue immediately surrounding an implanted device [109, 111]. These findings suggest that an altered local ionic milieu leading to neuronal silencing, decreased neuronal conduction, and/or compromised synaptic stability could all influence recording instability [151-153]. While we have not studied the progression of these phenomena over time, it is important to note that neuroinflammtory diseases such as MS exhibit BBB dysfunction and myelin disruption that are quite transitory [154, 155]. This fact adds credence to their possible role in recording inconsistency.

The impact of the FBR is not limited to the tissue immediately surrounding the implanted device. In, as of yet, unpublished work from our lab we have documented that chronic electrode implantation is accompanied by decreased neurogenesis in the subventricular zone of the dentate gyrus (DG). We observed this decrease in both microelectrodes implanted into CA1 of the hippocampus (a structure closely associated with the DG) as well as devices implanted solely in

regions of the cortex away from either the hippocampus or DG. Similar to our findings regarding BBB dysfunction, decreases in neurogenesis have been observed in neuroinflammatory diseases such as Alzheimer's disease [156]. In these conditions it is widely believed that these phenomena are caused by activated macrophages/microglia and their released soluble factors [157].

1.5 Previous efforts to improve the biocompatibility of microelectrodes

Despite our increased understanding of the brain's response to microelectrode implantation, whether it influences recording consistency, and how this might occur, it is still unclear if the goal of seamless integration into nervous tissue is possible and whether the FBR can be modulated by intentionally manipulating constitutive properties of the implant. A number of groups have investigated possible methods for improving the FBR, which have been met primarily with minor to moderate success.

There are a number of important facts to consider when comparing and analyzing findings from these studies. First, in almost all cases the devices were removed from tissue prior to analysis. As we have shown in our lab, device removal disrupts the tissue interface by removing adherent tissue and may influence data interpretation [108-111], especially for coatings that may improve cell attachment. Different groups also use a variety of different markers to describe the same cellular and molecular features of the FBR. An example of this is the use of pan-macrophage markers such as OX-42 and IBA-1 versus markers for activated macrophages such as CD-68. There are also large to subtle differences in the methods used to image and quantify these changes that can

lead to differences in interpretation. Additionally, a number of groups present optimistic conclusions about the level of FBR reduction that are not shown by their representative figures or their quantitative metrics.

1.5.1 Altering device geometry and architecture

Szarwoski et al. conducted the first study investigating the potential of changing device architecture and geometry to alter the FBR [139]. In this study the authors studied the FBR to a variety of devices with different cross sectional areas, tip geometries, and surface roughness and concluded that the tissue response was independent of these electrode properties. We believe that their results and conclusions stem from the fact that while their devices were different in a number of parameters, that in fact, these slight differences were too minimal to induce changes in the FBR. These overly broad conclusions have since been contradicted in several recent studies looking at either planar or cylindrical devices as well as published work from our lab, which will be further discussed in Chapters 2 and 3 [136, 140, 158].

Of these contradicting studies, both Stice et al. and Thelin et al. provided evidence that changing device geometry and reducing presented surface area impacts the FBR [140, 158]. In these studies, both groups independently found significant differences in classic hallmarks of the FBR between microwires of different diameters. These groups hypothesized that reducing the initial iatrogenic injury by presenting a smaller cross-sectional area drove their results. However, this hypothesis is confounded due to differences between both the presented surface area and curvature of the disparate sized microwires. To

elucidate a mechanistic understanding of the driving features of the FBR that can lead to improved device design and clinical impact, further effort must be taken to isolate design variables that could influence the FBR. The impacts of these improvements in the FBR have not been investigated on device function to date.

In a further contradicting study, Seymour and Kipke found significant differences in both the neuronal and non-neuronal cell responses between a parylene-C based electrode's larger shank and an adjoining thin lateral platform designed with a variety of different sized subcellular lattice architectures [136]. In this work the authors used devices with identical penetrating profiles to remove the impact of the extent of iatrogenic injury on their findings. Seymour and Kipke originally hypothesized that presenting a structure below a critical surface area would result in a reduction in the FBR. While their findings did support this hypothesis, due to insignificant differences in the FBR to their lattice elements of different sizes, the group chose to adopt the theory of mechanical differences between the thin adjoining lattices and the larger primary solid shanks as the explanation of their results. While we acknowledge that mechanics may play a role in the FBR, as we will explain in Chapters 2 and 3, we believe that their original hypothesis may be the more accurate explanation as there were likely insufficient size differences between their small lattice elements to cause significant changes in the FBR surrounding these structures.

1.5.2 Mechanical mismatch and brain micromotion

Along with Seymour and Kipke, a number of other groups have investigated the hypothesis that brain micromotion in combination with the mechanical

mismatch between the stiff electrode array materials and the softer brain tissue may induce shear and compressive forces that perpetuate the FBR, damage nearby cells, and induce relative displacement of the electrode recording site to cortical tissue. Goldstein and Salcman first put this idea forth in 1973, though the most cited work for this hypothesis is Edell et al. in 1992 [133, 159].

Based on this hypothesis a number of groups have investigated the use of softer materials to better match the mechanical properties of the brain and minimize forces exerted on the tissue, attenuating inflammation and repetitive tissue damage. For example, Harris et al. has shown that implantation of a nanocomposite microprobe with a Young's modulus of 33MPa into a rat cortex for up to eight weeks demonstrated increased cell density at the biotic/abiotic interface and a lack of tissue necrosis [160, 161]. While these findings indicate that better mechanical matching may indeed improve the FBR, confounding factors also exist for these materials, which make arriving at a definitive conclusion difficult. One of these factors is the fact that many of these materials absorb a significant amount of water upon implantation and may also act as permeable sinks, improving clearance of macrophage-released factors from the surrounding tissue. This theory will be further described in Chapters 2 and 4.

One important finding from our lab that adds to this body of literature is the fact that implants that are anchored to the skull have a more severe FBR than free-floating implants [110, 162]. This finding has led to several groups pursuing free-floating devices that may limit mechanical strains on tissue at the biotic/abiotic interface. It should be noted that all of the work in this dissertation

used devices that were fixed to the skull, and that despite this added hurdle that our strategies were still able to reduce the FBR which will be discussed further in Chapters 3 and 4.

1.5.3 Preventing cell adhesion

An alternative strategy to reduce the FBR that we investigated was the use of coatings that prevented cell adhesion to minimize activation of macrophages at the device surface [109, 163]. To test this hypothesis we compared the FBR of planar silicon microelectrodes that had a uniform coating of parylene C, which prevented cell attachment in vitro, to that of identical uncoated devices. Interestingly, we found no significant difference in the FBR to the parylene C coated devices at 2, 4 or 12 weeks compared to control uncoated devices. This finding indicated that cell adhesion is not necessary to drive the FBR or that close association of the electrode with brain tissue at the biotic/abiotic interface is sufficient to allow inflammatory cell invasion and persistent residence immediately surrounding the device. To our knowledge no type of inert coating has been shown to reduce the FBR in any other tissue or implant model.

1.5.4 Incorporating bioactive coatings

In contrast to our results using inert coatings, a number of groups have shown that bioactive coatings can be used to alter the FBR to microelectrodes. One bioactive coating strategy that has been effective in altering the FBR is work by He et al. [164]. In this study the authors showed that coating the device with the extracellular matrix (ECM) protein laminin (LN) alters the traditional

microglia/macrophage and astrocytic response to implanted planar silicon arrays. Specifically, they observed an approximate 60% increase in CD-68 expression (described as a marker for activated macrophages) near LN-coated devices compared with uncoated devices one day post-implantation. However, after four weeks of implantation, the authors observed an approximate 20% reduction in CD-68 expression along with an approximate 50% reduction in GFAP expression surrounding the coated compared to uncoated devices. The authors concluded that their LN coatings had a stimulatory effect on early-phase microglia activation that improved early wound healing and the subsequent integration of the devices into tissue.

Another bioactive coating that has shown great potential is work by Azemi et al. [165, 166]. In this study the authors covalently immobilized the extracellular matrix, neural adhesion protein L1 to the surface of MI-style microelectrodes and compared the tissue response between coated and uncoated devices implanted in the rat cortex for one, four and eight weeks. In contrast to uncoated devices that exhibit a typical FBR, the L1 coated probes showed little neuronal loss, significantly increased axonal density relative to background, as well as lower activation of microglia and astrocyte hypertrophy. These findings provide further evidence for the usefulness of bioactive intervention strategies based on the ECM. An alternative bioactive strategy based on harvesting the extracellular matrix from immature astrocytes and glial-precursor cells will be discussed in Chapter 5.

Though not specifically a study examining bioactive coatings, another theory that builds from an understanding of the ECM is work done by Moxon et al. [167-169]. These researchers examined the impact of presenting a roughened, porous silicon surface, which was designed to better mimic the nanostructured and fibrous nature of the extracellular matrix on the FBR. Implantation of nano-porous surfaces was found to induce less glial activation and to slightly improve neuronal density near the device. However, these findings have only been examined out to one week post-implantation and their lasting impact on the FBR is unclear.

1.5.5 Delivery of anti-inflammatory agents

Building off Rennekar's work that administered the anti-inflammatory drug minocycline and saw improvements in recording performance [104], Zhong and Bellamkonda developed probe coatings that locally released the anti-inflammatory drug dexamethasone (DEX) [170]. DEX coatings significantly reduced both activated macrophage and hypertrophic astrocyte reactivity one-week postimplantation compared to uncoated controls. Interestingly, at four weeks postimplantation there was no significant difference in the reactivity between coated and uncoated cohorts for these markers. This discrepancy may have been due to exhaustion of the drug source between these time frames. If this were the case, it would signify that a chronic anti-inflammatory regimen might be needed to reduce the FBR through the lifetime of the implanted device.

1.6 A new focus: Device design to limit the impact of activated macrophages and their secreted factors to improve the biocompatibility of microelectrode arrays

Despite some cases describing measured improvements in the FBR to implanted microelectrodes, this body of published work has been limited by a lack of hypothesis-driven testing based on a mechanistic understanding of the FBR. Without a knowledge regarding the cellular or molecular mechanism by which their design changes altered the FBR, translating and optimizing these approaches will be difficult. The work described herein is based on this desire to offer designers new tools and better strategies for reducing the FBR to improve device function and patient care that are based on a guiding-mechanistic understanding of the FBR.

When searching for cellular and molecular mechanisms that device designers can manipulate to improve the FBR, it becomes evident that pro-inflammatory and cytotoxic soluble factors secreted by reactive macrophages/microglia at the device-tissue interface are the most likely mediators of the cellular-level changes underlying the FBR. Based on this assumption, we hypothesize that implant designs that passively reduce macrophage activation or the concentrations of their released soluble factors surrounding the implant will reduce the severity of the FBR.

To explore this broader hypothesis and mechanism we have investigated a number of methods for reducing either the quantity and activation state of macrophages at the device interface or the distribution of their secreted factors

through the use of passive design changes and the incorporation of bioactive coatings. To guide our passive design changes, we first created a series of 3-D finite element simulations to predict the distributions of various macrophage-secreted factors around virtual device designs (Chapter 2). Based on predictions from these models we have examined both the impact of simple architectural changes that reduce the number of inflammatory cells at the device interface (Chapter 3), as well as incorporation of passive permeable coatings to reduce the impact of their secreted factors (Chapter 4). Lastly we have developed new techniques to integrate ECM harvested from young immature astrocytes and glial precursor cells that have been shown to play a key role in down regulating macrophage activity in healthy tissue (Chapter 5).

CHAPTER 2

TOWARDS INFORMED DEVICE DESIGN: MODELING THE FOREIGN BODY RESPONSE TO DEVICES IMPLANTED IN THE CNS

2.1 Introduction

Numerous studies have shown the potential for using implanted microelectrode arrays to drive brain machine interface (BMI) applications for the rehabilitation of spinal cord injury (SCI) patients and those suffering limb amputation [94-97, 171]. Despite these promising results, achieving widespread clinical application of this technology requires improving recording consistency and quality as well as extending the lifetime of these devices to a clinically relevant time frame. It is widely accepted that one of the greatest challenges that we need to overcome to improve recording quality and device lifetime is the foreign body response (FBR) against implanted microelectrodes.

Numerous studies have described consistent, stereotypic features of the brain FBR that occur irrespective of the type of implant, species studied, or implantation method. The foremost hallmark of the brain FBR, as well as the FBR in other tissues, is persistent inflammation at the biotic-abiotic interface signaled

by biomarkers for activated macrophages and resident microglia [108, 109, 111, 137]. Surrounding this inflammatory core, a region consisting of hypertrophic astrocytes, fibroblasts, and meningeal cells has been observed [108-111, 133, 134, 136-139, 172]. Associated with this region of inflammation and reactive gliosis, local nerve fiber and neuronal cell body densities are also decreased [105, 108-111, 133, 135, 137, 138]. These findings lead us to believe that the FBR to implanted devices may affect recording quality by electrically isolating the device from healthy viable neurons [108].

Additionally, when we examine the FBR to various microelectrode designs it becomes apparent that the FBR mirrors the geometry and architecture of the implanted device. Multiple studies have noted the fact that surrounding traditional planar MI-style devices that are approximately 100μm wide by 12μm thick, there is minimal impact surrounding the thin lateral edges of the device compared to the broad planar faces [108-111]. In contrast, cylindrical microwire devices usually have a more uniform, concentric, circular-shaped FBR [111]. In addition, the FBR to chronically implanted Utah Electrode Arrays (UEAs), that have a much more complex architecture, shows a gradient of severity as a function of depth from the cortical surface, with a severe reaction that spans the area underneath the base of the array near the top of the cortex down to a minimal reaction near the recording tips that is isolated to each penetrating tine. For images of the FBR to planar MI-style microelectrodes and microwire devices refer to Figure 1-7 in the previous chapter. The FBR to the UEA is shown here in Figure 2-1.

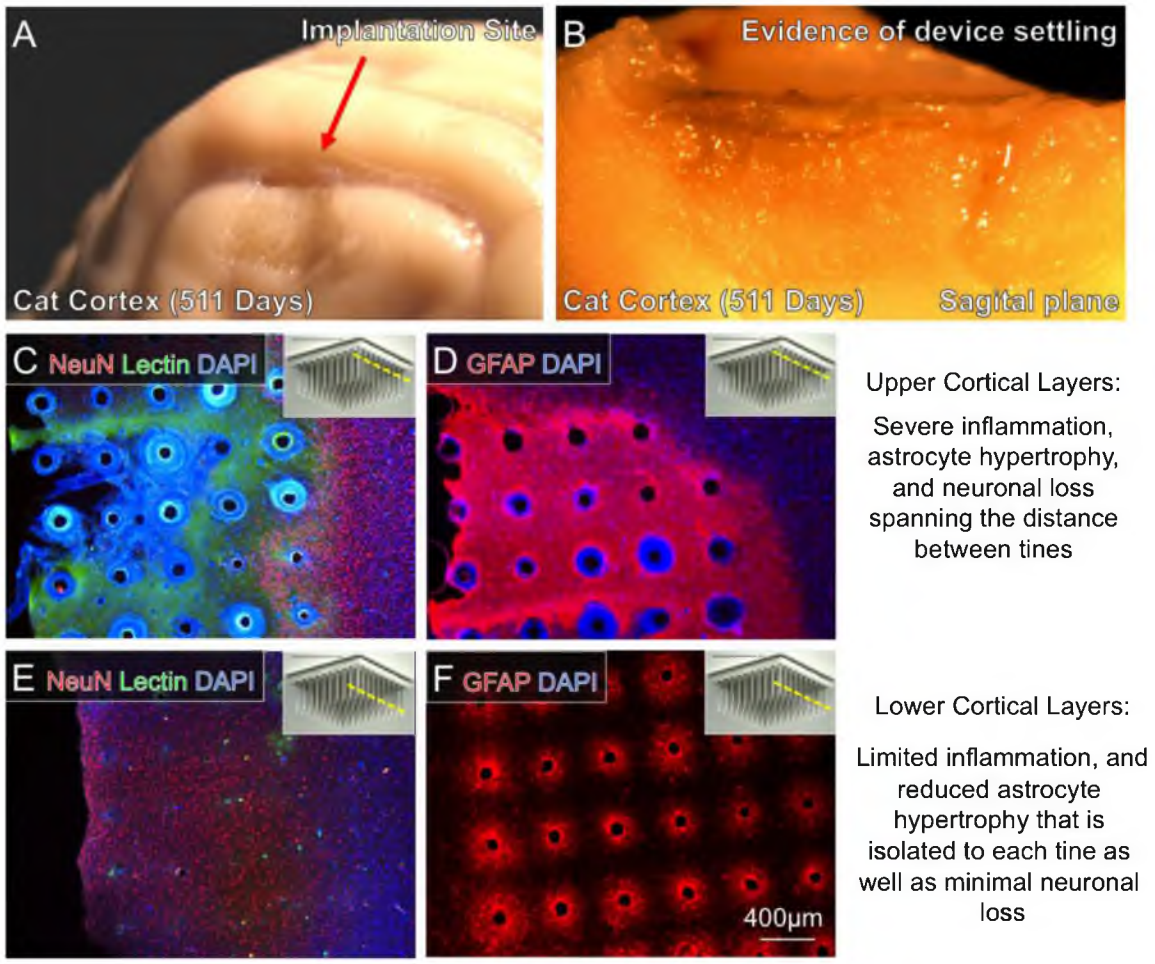

Figure 2-1: (A & B) Representative gross level images of a cat cortex chronically implanted with an UEA showing signs of tissue erosion and device settling. (C-F) Representative horizontal sections show a graded response in the neuronal (NeuN – red), macrophage (Lectin – green), astrocyte (GFAP – red) and overall cellular reactions (DAPI – blue) to the implanted UEA with a more severe reaction directly underneath the base of the array compared to that observed at the recording tips.

Despite our increased understanding of the CNS's foreign body response to chronically implanted devices, it is still unclear if the goal of seamless integration into the nervous system is possible and whether device designers can modulate specific aspects of the FBR by intentionally manipulating implant architecture or other constitutive properties [133, 136, 139]. Based on increasing evidence that macrophages and their released soluble factors play a key role in driving and shaping the cellular level features of the brain FBR, our group hypothesizes that implant designs that reduce the concentrations of these soluble factors adjacent to implanted devices will limit the severity of the FBR. However, to date, little effort in the field has been directed at studying the distribution of macrophage-released soluble factors surrounding implanted devices and, to our knowledge, no one has explored how device design can be altered to minimize their distribution and subsequent impact on surrounding tissue.

To address this need, we have developed a computational model to predict the steady-state distribution of macrophage-released soluble factors surrounding traditional and novel device designs. Due to the difficulty of analyzing the spatial distribution of macrophage-released factors in tissue, we validated the usefulness of our models and our underlying hypothesis using a number of indirect methods. In the first of these indirect methods, we investigated whether our model and hypothesis could explain differences in the shape and structure of the FBR to a variety of implanted microelectrodes with different architectures including planar MI-style arrays, cylindrical microwires and more complex devices like the UEA. To further our validation efforts we tested whether our

model could explain the reduced FBR seen around semipermeable hollow fiber membranes (HFMs). Based on findings from these models, we present two potential design strategies to minimize the concentration/impact of macrophage-released factors in tissue surrounding implanted devices, namely (1) decreasing the amount of device surface area for macrophage interaction/activation and (2) incorporating permeable coatings to act as cytokine sinks to improve clearance of macrophage-released factors.

2.2 Methods

2.2.1 COMSOL model physical layout

3-D virtual devices were created using COMSOL Multiphysics (COMSOL Group, Stockholm, SE). The models created included traditional microelectrode designs such as planar MI-style microelectrodes, cylindrical microwires, and the more complex Utah Electrode Arrays (UEAs). We also modeled a semipermeable HFM to investigate whether our model could help elucidate why these devices have a significantly reduced FBR compared to other devices implanted in the CNS. Additionally, novel designs with altered architectures and incorporation of thick permeable coatings were created.

Surrounding these constructs, a concentric, scaled copy of the original construct was added to mimic the macrophage layer found surrounding all traditional devices implanted into the CNS. This macrophage layer acted as the source of cytokine production in the model. A further rectangular block acted as the surrounding brain tissue where diffusion and clearance of macrophage released factors occurred. Figure 2-2 shows the different regions involved in the

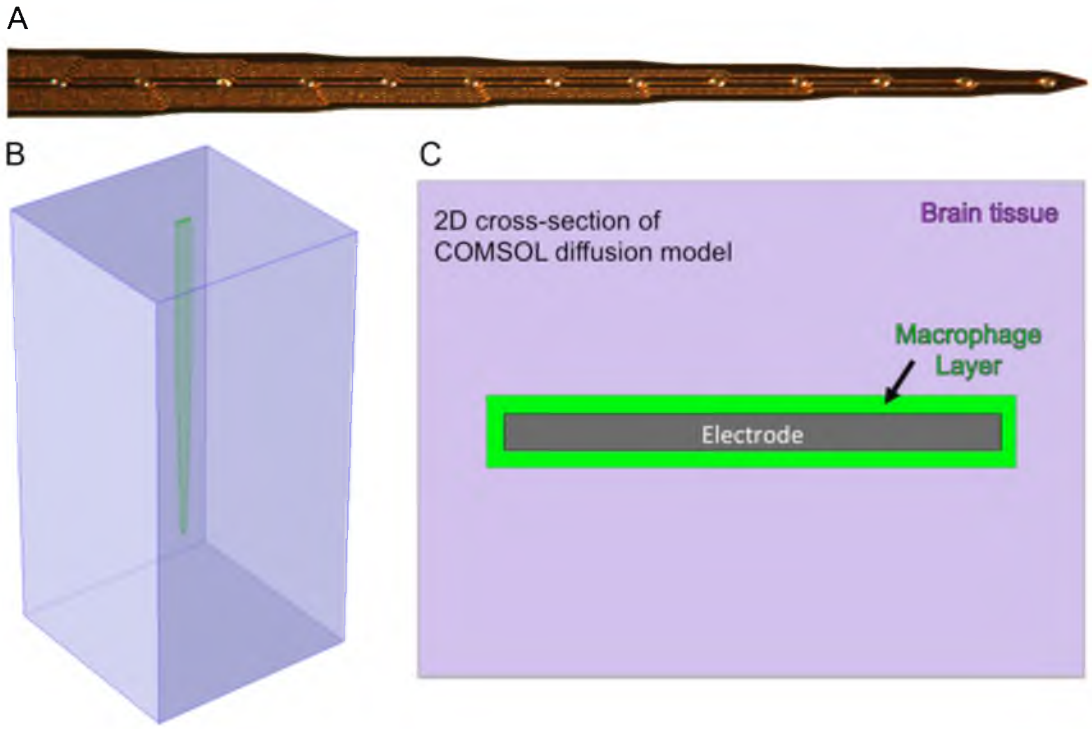

Figure 2-2: (A) Representative image of a planar, tapering MI-style microelectrode. Electrode tapers from approximately 200µm at the base to 33µm at the last taper before the sharp tip. (B) 3-D planar tapering MI-style microelectrode model created within COMSOL. (C) Cross section of the MI model. At the center of the model is the impermeable electrode (grey). Surrounding this is a concentric macrophage layer (green) that acts as the source of cytokine production in the model. Diffusion and clearance of these cytokines occurs in this layer as well as the surrounding brain tissue (purple). Similar models were created for the other impermeable electrodes including cylindrical microwires, 10x10 UEA, 4x4 UEA, and lattice MI microelectrodes.

FE models for a planar MI-style microelectrode array. Similar regions were included in the cylindrical microwire and UEA models. Figure 2-3 illustrates the regions involved in the semipermeable HFM model.

2.2.2 Simulating macrophage-released factor distributions

We modeled soluble factor production from the macrophage layer via a zero-order reaction using reported literature values for macrophage production of TNF-α and MCP-1 in vitro (Table 2-1) [108, 173, 174].

We modeled diffusion of macrophage-released factors through brain tissue as well as the permeable HFM and alginate coatings via isotropic diffusion, where the flux of solute from a given point is governed by its local diffusivity and concentration gradient (Eq. 2-1). The apparent diffusivity of TNF-α and MCP-1 in cortical brain tissue, cerebral spinal fluid, the HFM wall and our permeable, alginate-hydrogel coating is shown in Table 2-1. We based these values on findings from the literature as well as previous cortical diffusion experiments conducted in our lab for molecules of similar size diffusing from a hollow fiber membrane system [108, 173-180]. We assumed an isotropic diffusivity for cortical tissue based on work by Vorisek and Sykova [178, 179]. We chose to use an apparent diffusivity value in place of standard diffusivity to account for the impact of tortuosity and other confounding variables on the transport of macrophage-released soluble factors through tissue and our various materials.

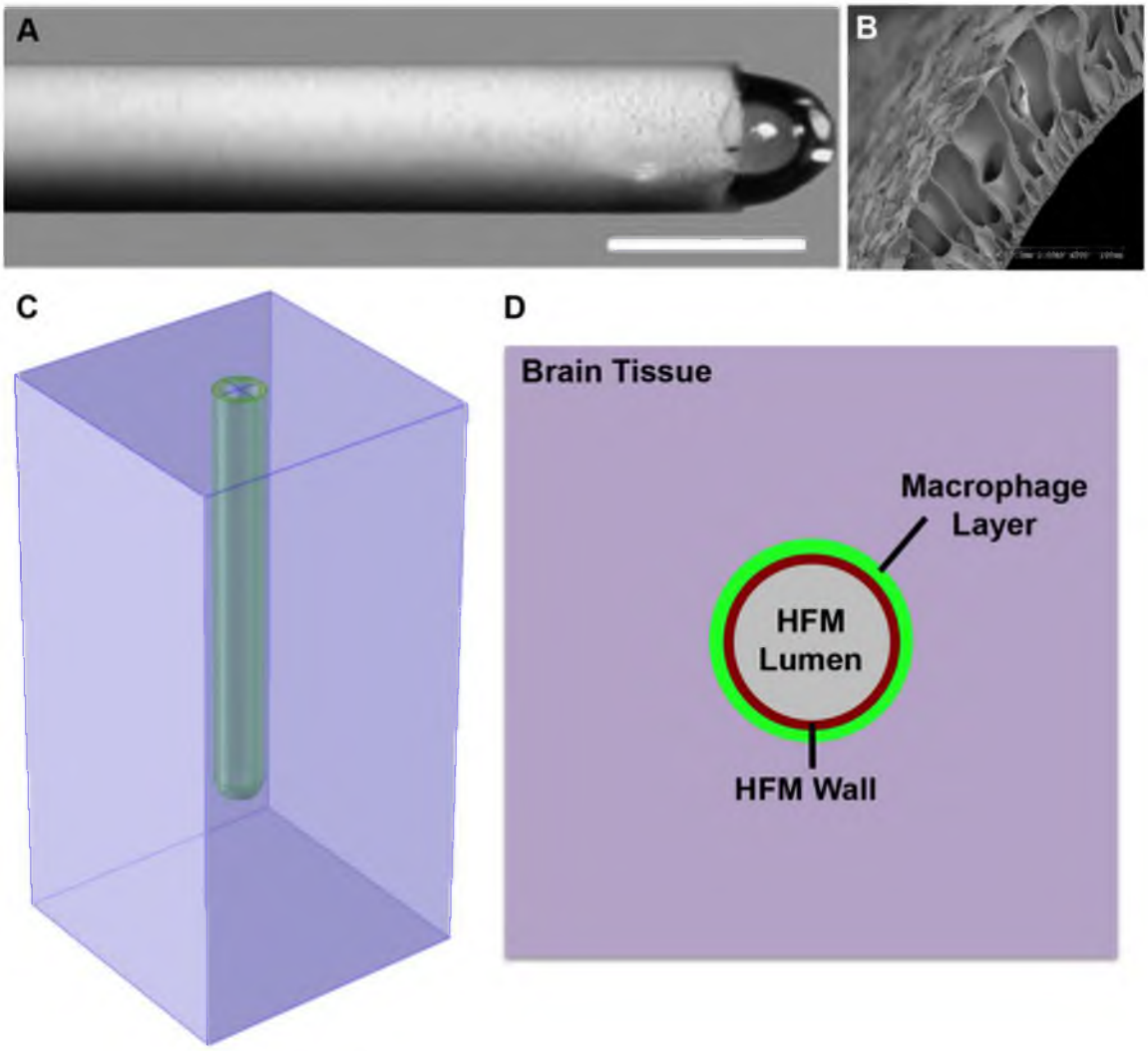

Figure 2-3: (A) Representative image of a PAN-PVC HFM. (B) Cross section of the HFM showing the porosity of HFM wall with large micron scale pores near the outer surface of the HFM and nanoscale pores on the inner surface. The size of these inner nanopores determines the HFM's exclusion size. (C) 3-D HFM model created within COMSOL. (D) Cross section of the HFM model. The key difference between this model and the various microelectrode models is the inclusion of a permeable HFM wall layer and an inner lumen filled with CSF in place of the solid impermeable electrode material used in the other models. Scale bar shown in A = 500µm. Scale bar shown in B = 100µm.

The clearance/degradation of macrophage-released soluble factors in brain tissue and permeable coatings was modeled via first order elimination (Eq. 2-2). The elimination rate constant, k, for different soluble factors of interest is derived from Eq. 3 and reported literature values for the half-lives ($t_{1/2}$) of said factors (Table 2-1) [173, 174].

2.2.3 Assumptions

A no-flux boundary condition was incorporated for all solid device surfaces as well as the upper surface of the brain tissue block in our 3-D models. We applied an open boundary to the five remaining faces of the tissue block with an initial zero mol x L^{-1} concentration outside of the block.

Table 2-1: Summary of model parameters for TNF-α and MCP-1.

	Production Rate (mol×L^{-1}×s^{-1})	Apparent Diffusivity in cortical tissue ($m^2 \times s^{-1}$)	Apparent Diffusivity in CSF ($m^2 \times s^{-1}$)	Apparent Diffusivity in alg. ($m^2 \times s^{-1}$)	Half-life (min)	Refs
TNF-α	1.60 x 10^{-13}	1.54 x 10^{-11}	3.70 x 10^{-11}	3.12 x 10^{-11}	25	[108, 173-180]
MCP-1	5.92 x 10^{-12}	2.22 x 10^{-11}	5.23 x 10^{-11}	4.41 x 10^{-11}	45	

Eq. 2-1 – Isotropic, steady state diffusion governed by:

$$\nabla\cdot(-D_j \nabla c_j) = R_j$$
$$\mathbf{N}_j = -D_j \nabla c_j$$

Eq. 2-2 – Soluble factor clearance and degradation:

$$C_t = C_0 * e^{-kt}$$

Eq. 2-3 – Relation of elimination rate constant and half-life:

$$k = \frac{\ln 2}{t_{1/2}}$$

2.2.4 Finite element meshing

To eliminate the effect of mesh quality and size on the results, simulations were performed with a variety of different mesh resolutions. Meshes that were finer than the size range determined to affect our results were used in all simulations.

2.3 Results and discussion

To validate our models as well as to examine their usefulness, we first investigated whether they could predict and explain common observations surrounding traditional microelectrode implants including planar MI-style microelectrodes and cylindrical microwires. The predicted distribution of macrophage-released soluble factors from our model for a traditional planar MI-style array is shown in Figure 2-4. This model predicted a distribution of macrophage-released factors that had a similar shape to the device's geometry as well as the typical FBR that has been documented surrounding these devices [108-110]. The greatest predicted concentration of released factors at any given depth was located at the center of the device where the greatest summation of soluble gradients from nearby macrophage sources could occur. There was a reduction in concentration along the thin 12μm wide lateral edges of the device compared to that at the center of the broad face. This finding provides a mechanism to explain common observations that the FBR is less severe along the thin lateral edges of MI style devices [108, 109, 136].

Similarly, our model for the cylindrical microwire devices predicted a distribution that coincided well with the documented structure and shape of the

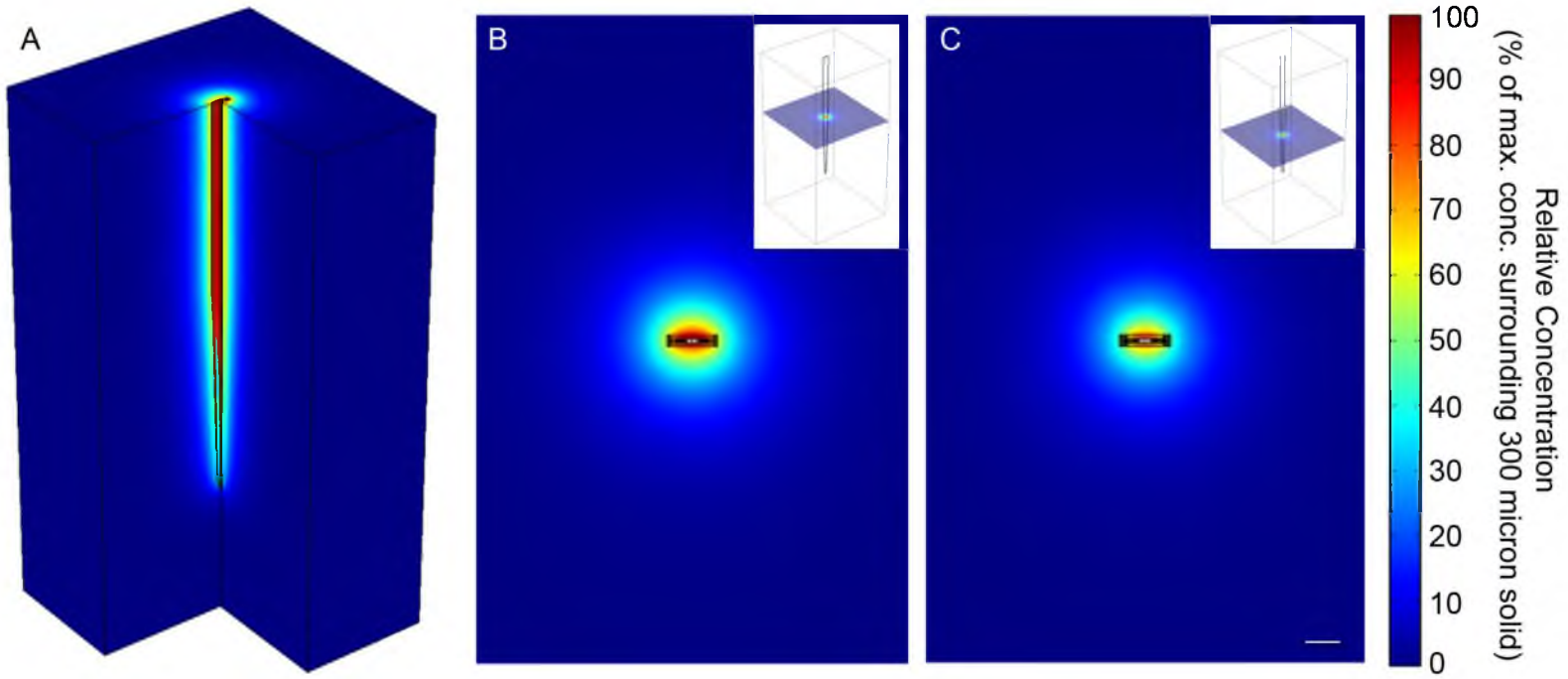

Figure 2-4: (A) Isotropic surface model showing the predicted TNF-α distribution surrounding a planar, tapering MI-style microelectrode. (B & C) Horizontal cross sections showing the predicted TNF-α distribution at depths of 750 and 1500µm, respectively. As the tapering electrode shank decreases in size, the predicted distribution lessens, indicating that the amount of presented surface area impacts the predicted cytokine distribution. Simulated cytokine levels are relative to the peak concentration surrounding the uncoated 300µm solid array in Figure 2-8A. Scale bar = 100µm.

FBR to these cylindrical devices (Figure 2-5). Moreover, our model predicted a reduced concentration of these factors surrounding the implanted device compared to the planar MI array. This reduction agrees well with our observations that there is a reduced FBR to this size of microwire device. compared to planar MI-devices when implanted using identical methods in our lab [108, 109, 111, 136].

As described in the introduction to this chapter, the FBR response to the UEA shows a gradient of severity as a function of depth from the cortical surface. Under the base of the array there is nearly complete loss of neurons, hypertrophic astrocytes that span the distance between tines and intense hypercellularity, indicative of a severe inflammatory reaction. These indicators of the FBR are significantly greater than that seen around single planar MI implants. In contrast to this severe response near the base, there is only minimal neuronal loss, astrocyte hypertrophy and hypercellularity near the recording tips with the overall response near any tine's recording tip being less than that surrounding traditional planar MI-devices.

Our UEA model (shown in Figure 2-6) shows a similar gradient with extremely high concentrations of soluble factors under the base of the array and in the upper cortical regions with significantly reduced concentrations near the recording tips of each electrode tine. Excitingly, when compared to our planar MI-array models, the predicted concentrations of macrophage-released factors underneath the base of the array and at the tines follow a similar relative pattern as the differences in classic hallmarks of FBR between these devices.

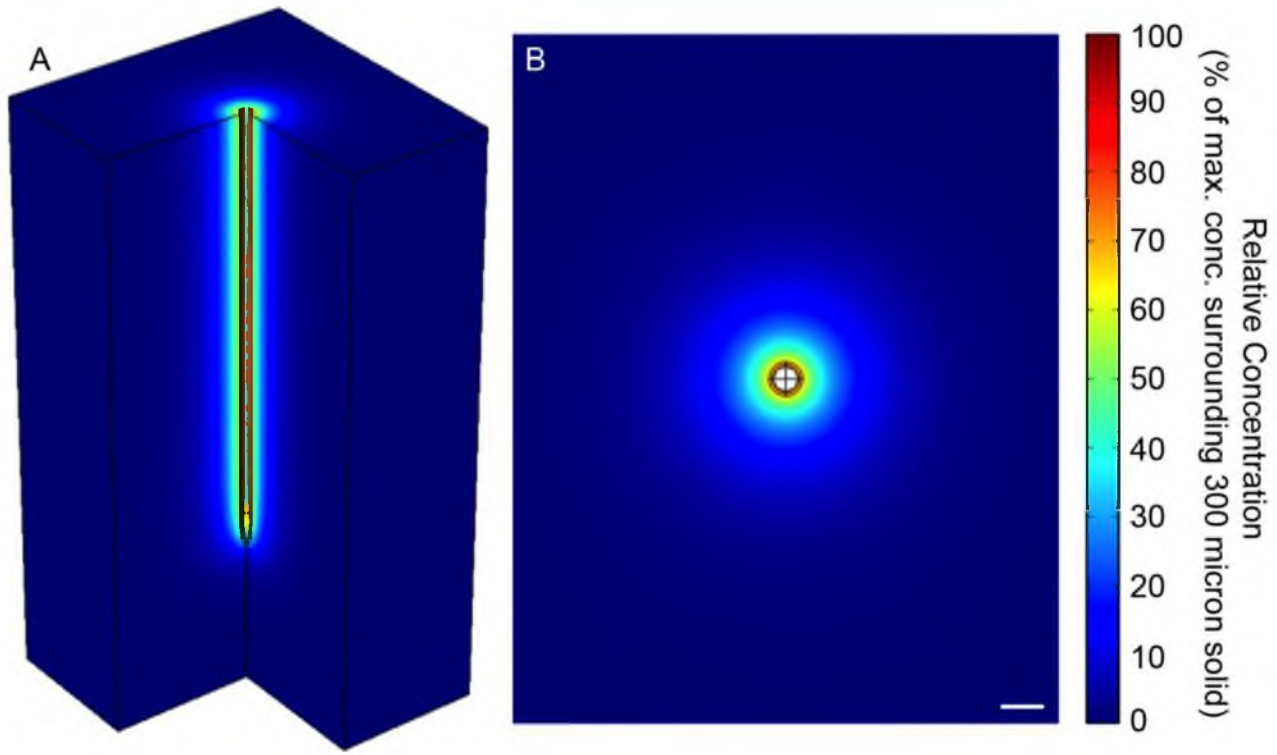

Figure 2-5: (A) Isotropic surface model showing the predicted TNF-α distribution surrounding a 75μm cylindrical microwire array similar to that used in Winslow & Tresco 2010 [111]. (B) Horizontal cross section showing the predicted TNF-α distribution at a depth of 750μm. The predicted distribution surrounding microwire is reduced by roughly 20% that of a tapering MI-style device at a similar depth. This finding again, indicates that the amount of presented surface area impacts the predicted cytokine distribution. Simulated cytokine levels are relative to the peak concentration surrounding the uncoated 300μm solid array in Figure 2-9A. Scale bar = 100μm.

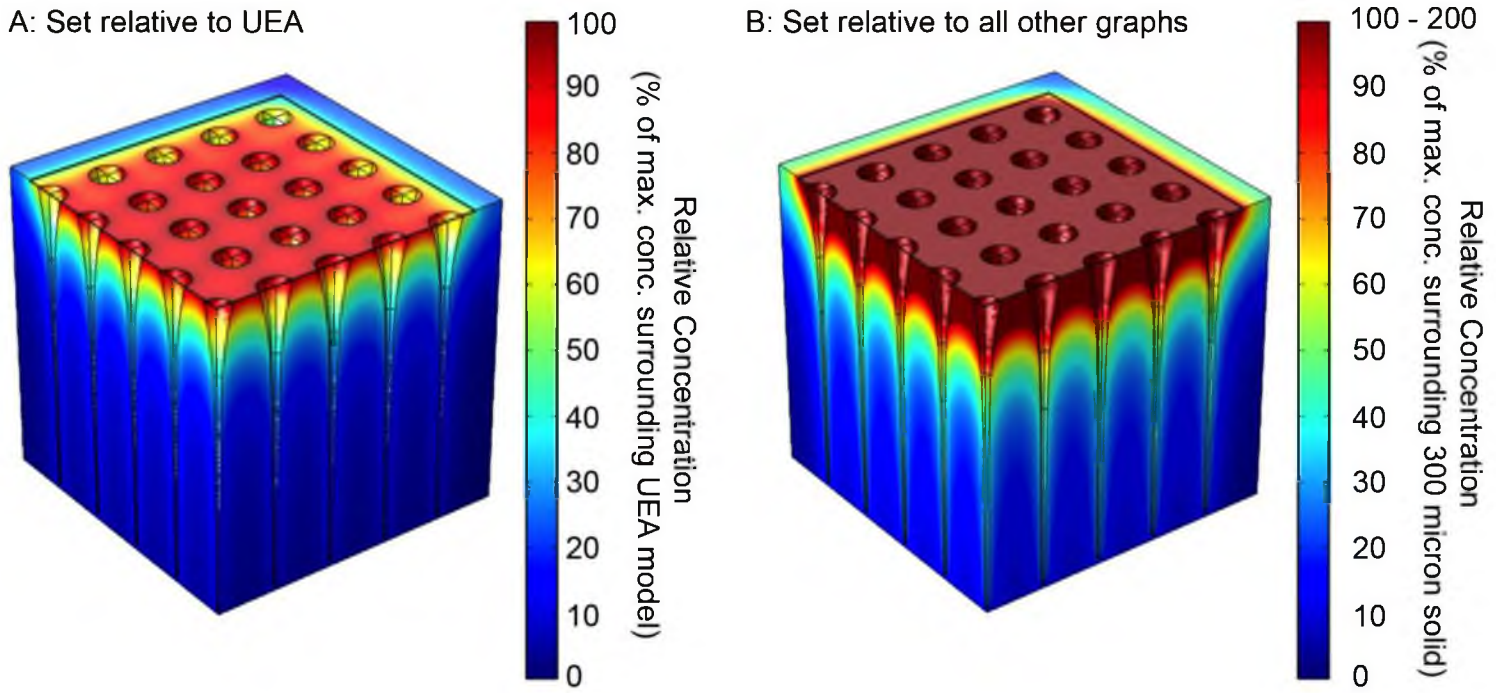

Figure 2-6: (A & B) Isotropic surface model showing the predicted TNF-α distribution surrounding a 10x10 UEA with 2mm long tines and 400µm tine spacing. Only 25% of the device is depicted to enable viewing the relative concentration as a function of depth in the center of the array of tines. The relative concentration in (A) is set relative to the maximum concentration surrounding the UEA in this model to illustrate differences between the predicted concentrations underneath the base of the device and at the tine tips. This predicted maximum concentration is roughly twice that of the maximum surrounding the tapering MI-style device. To facilitate comparison of the UEA model with all other models in this work, we have set the relative concentration in (B) to the same maximum as the other models. By doing this, all areas above the maximum concentration surrounding the uncoated 300µm solid array in Figure 2-9A are shown in deep red (100-200% scale).

Beyond these traditional recording devices we also wanted to examine the usefulness of our models by testing to see whether they could explain the significantly low FBR that we have observed surrounding implanted semi-permeable HFMs. Despite having a larger penetrating profile, our HFM models had maximum concentrations at the device interface that were roughly 55% that of the maximum surrounding the planar-MI array model (Figure 2-7). However, making the HFM wall impermeable resulted in a near doubling of the predicted concentration making the maximum similar to that adjacent to the planar MI device (data not shown). These findings indicate that the permeable nature of the HFM was responsible for the predicted decrease in soluble factor concentration and provide a mechanism to explain the minimal FBR surrounding these devices when compared to other traditional devices implanted in the CNS.

Additionally, our modeling also predicts that reducing presented surface area or incorporating a permeable sink coating, such as a hydrogel, will improve clearance of macrophage-released factors from the surrounding tissue and may reduce the FBR. Figures 2-8 and 2-9 compare the predicted distributions for an uncoated planar 300μm-wide solid device to a lattice device with the same penetrating profile but reduced surface area and an identical solid device with a 400μm-thick permeable coating.

In this work we have assumed that the majority of pro-inflammatory cytokines are created by activated macrophages. However, it has been suggested that other cell types involved with the brain FBR can also produce

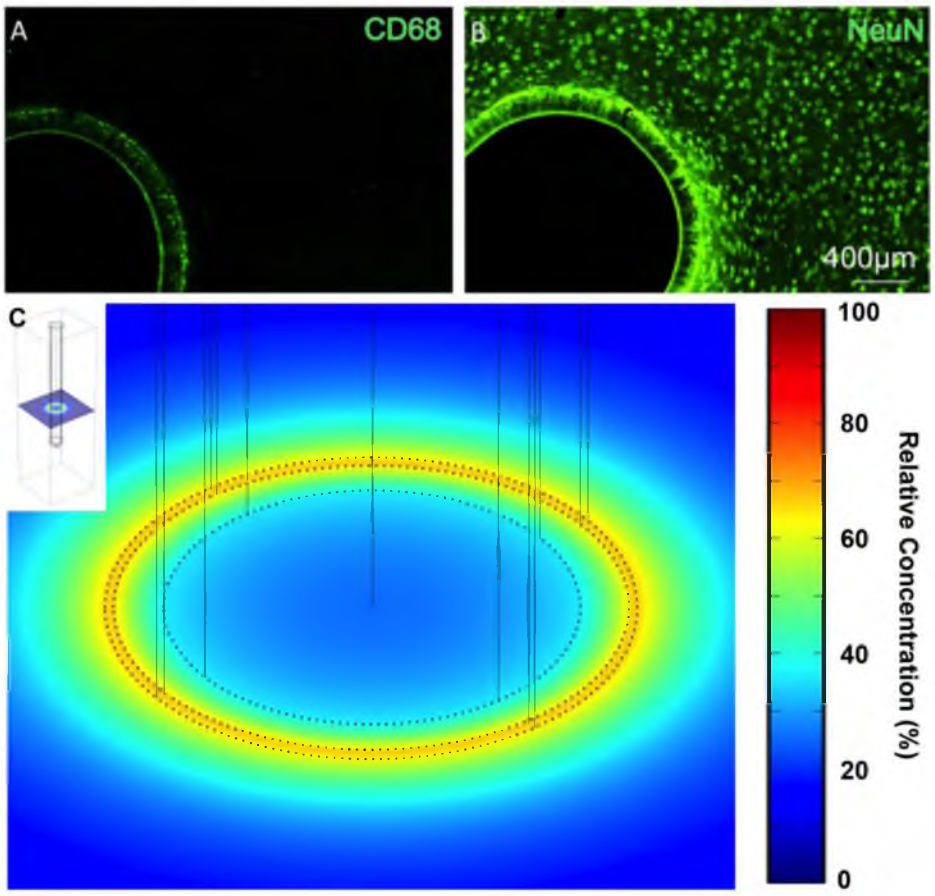

Figure 2-7: (A-B) Representative 12-week horizontal sections showing (A) CD68 (ED-1) and (B) NeuN immunoreactivity surrounding an implanted HFM. The PAN-PVC HFM autofluoresces to some degree in both A & B. We observed few ED-1+ cells and little neuronal loss adjacent to the HFM devices compared to that surrounding traditional microelectrode designs. (A) Predicted TNF-α distribution surrounding a simulated HFM with an outer diameter of 820μm and wall thickness of 80μm. Simulated cytokine levels are relative to the peak concentration surrounding the uncoated 300μm solid array in Figure 2-5A.

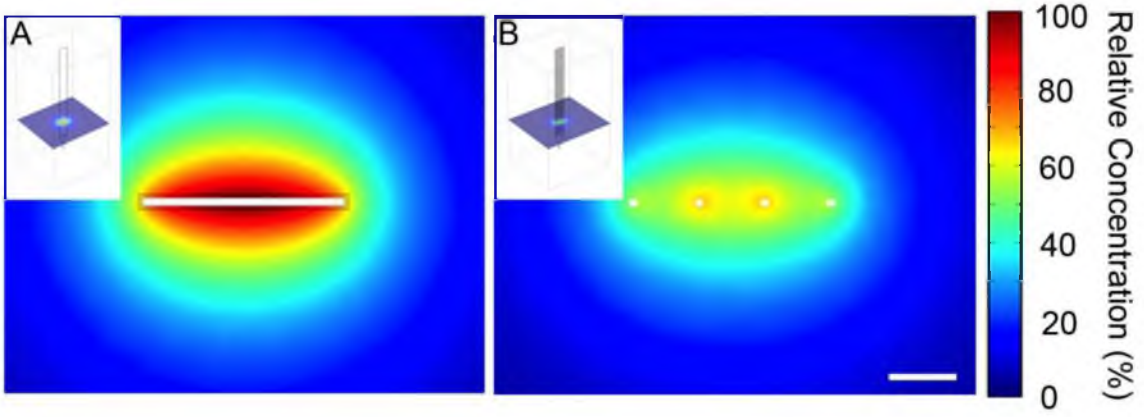

Figure 2-8: 2-D slices showing the predicted TNF-α distribution in cortical layer V surrounding (A) 300μm-wide solid and (B) lattice microelectrode arrays with identical penetrating profiles. Concentrations are set relative to the peak concentration surrounding the solid device. Decreasing the surface area that is exposed to macrophages by using this lattice structure decreases the peak concentration of released TNFα surrounding the lattice device by roughly 40%.

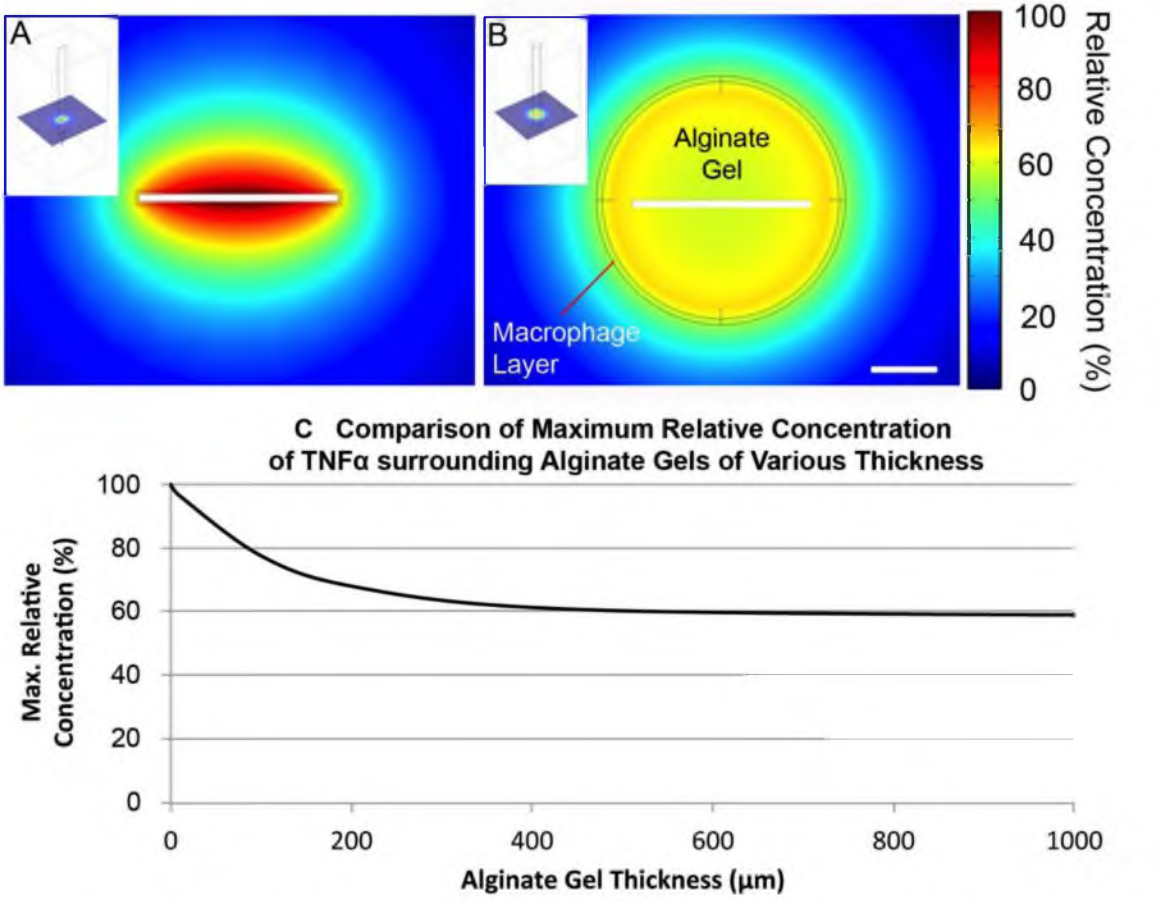

Figure 2-9: 2-D slices showing the predicted TNF-α distribution surrounding (A) an uncoated 300µm-wide solid microelectrode and (B) an identical microelectrode with a 400µm-thick alginate hydrogel coating. Concentrations are set relative to the peak concentration surrounding the solid device. Despite having a larger surface area, providing a new transport pathway with the permeable hydrogel coating reduces the released soluble factor concentration surrounding the coated device by roughly 40% (400µm thick gel). For this strategy to be effective the coating must be thick enough to passively entrap the soluble factors until they have had sufficient time to become passivated by hydrolysis and other degradation mechanisms. This is demonstrated in (C) by comparing the maximum concentration of TNF-α at the device/tissue interface for coatings of various thicknesses.

these molecules to a lesser degree [181]. Histopathological studies from our lab and others have shown that these cells form a syncytium surrounding the layer of activated macrophages at the device-tissue interface. An expanded source region would impact the distributions of proi-nflammatory factors as predicted by our models. Nevertheless, by predicting solely the impact of macrophages, our model does elucidate the high importance of these cells in the FBR and allows the investigation of strategies targeted at manipulating this cell population.

While our results provide a first pass validation of the model, more in depth validation by measuring in vivo cytokine distributions surrounding implanted devices is needed to improve the accuracy of our results. We are currently investigating a number of methods to measure and profile cytokine distribution in tissue, including immunohistochemically labeling cytokines of interest as well as detecting cytokine mass fragments using imaging MALDI mass spectroscopy. Once more fully established, these methods for profiling cytokine distributions in tissue will provide information to validate our diffusion models and improve the accuracy of their predictions.

2.4 Conclusion

In this study, to better understand the potential impact of macrophage-released factors on the cellular-level changes underlying the FBR, we created computational models to predict the steady-state distribution of these factors surrounding implanted devices. Due to the difficulty of analyzing the spatial distribution of macrophage released factors in tissue, we validated the usefulness of our models and our underlying hypothesis by verifying that they could explain

differences in the shape and structure of the FBR to a variety of implanted devices. In addition, we utilized our models to investigate a number of potential strategies to reduce the distribution FBR including (1) decreasing the amount of device surface area for macrophage interaction/activation and (2) incorporating permeable coatings to act as cytokine sinks to improve clearance of macrophage-released factors. Findings from these models further validate our hypothesis that macrophage-released soluble factors play a key role in driving and shaping the cellular level features of the brain FBR. Additionally, our findings indicate that implant designs that reduce the concentrations of these soluble factors adjacent to implanted devices limit the severity of the FBR.

CHAPTER 3

REDUCING SURFACE AREA WHILE MAINTAINING PENETRATING PROFILE LOWERS THE BRAIN FOREIGN BODY RESPONSE TO CHRONICALLY IMPLANTED SILICON MICROELECTRODE ARRAYS

3.1 Introduction

Numerous studies have shown that using implanted microelectrode arrays, consciously modulated neural signals can be recorded in both animal subjects as well as human patients for periods of time ranging from months to multiple years and that these recorded signals can be used to control a number of external devices [94-97, 171]. Despite these promising results, achieving widespread clinical application of this technology requires improving recording consistency over a clinically relevant time frame. A widely accepted theory in the field is that the foreign body response (FBR) that the brain mounts against implanted microelectrodes contributes to the observed recording instability, currently limiting clinical application.

Since the original work by Collias and Manuelidis [105], over 60 years of studies have described consistent, stereotypic features of the brain FBR that occur irrespective of the type of implant, species studied, or implantation method. A key feature of the FBR is persistent inflammation at the biotic-abiotic interface signaled by biomarkers for activated microglia and macrophages [108, 109, 111, 137]. Surrounding this, a region consisting of hypertrophic astrocytes, fibroblasts, and meningeal cells has been observed [108-111, 133, 134, 136-139, 172]. Associated with the region of inflammation and reactive gliosis, studies also have described a decrease in the local nerve fiber and neuronal cell body densities surrounding implanted devices [105, 108-111, 133, 135, 137, 138]. We have shown that persistent inflammation and neuronal loss does not accompany stab wound injuries made with recording devices, indicating that these responses are associated with the continual presence of the implant and are not solely a result of iatrogenic injury accompanying device implantation [108].

More recent studies from our lab have built upon these observations and have shown that, as observed in many neurodegenerative disorders, the local blood brain barrier (BBB) is compromised and decreased myelination is observed in the tissue immediately surrounding the recording device [109, 111]. These findings suggest new possible mechanisms for the observed recording instability including an altered local ionic milieu leading to neuronal silencing, decreased neuronal conduction, and/or compromised synaptic stability. Furthermore, our findings using single shaft recording devices did not support several previous hypotheses for FBR associated recording failure mechanisms, including

progressive increases in astrocyte encapsulation or progressive neuronal loss within the recording zone, indicating that, at least for certain recording device designs, neuroinflammatory sequelae are a more likely candidate for causing chronic recording inconsistency.

Notwithstanding our increased understanding of the brain's response to microelectrodes and how it might influence recording consistency, it is still unclear if the electrode designers can sufficiently manipulate constitutive properties of the implant to modulate specific aspects of the FBR and achieve the goal of seamless integration into nervous tissue [133, 136, 139]. We hypothesize that the chronic tissue reaction to implanted electrodes is primarily modulated by the sustained delivery of bioactive factors that are released into the adjacent tissue by activated macrophages at the device/tissue interface. Additionally, if macrophage released factors shape the tissue reaction, then we believe that implant architectures that reduce the number of activated macrophages at the interface should reduce the magnitude of the foreign body response and improve biocompatibility. To begin testing this hypothesis, using quantitative immunohistochemical methods, we studied the brain tissue reaction to planar silicon microelectrode arrays with identical penetrating profiles but different amounts of exposed surface implanted chronically in the rat brain.

3.2 Methods

3.2.1 Microelectrodes

Silicon microelectrode arrays were supplied by the Center for Wireless Integrated Microsystems at the University of Michigan. Both styles of microelectrodes had identical penetrating profiles with shanks that were 300μm wide x 12μm thick and 3.45mm in length including a tapered tip (Figure 3-1). Surface area measurements were calculated from SolidWork (Dassault Systèmes SolidWorks Corp., Concord, MA) models of the implanted portion of the two styles of microelectrode arrays. To facilitate handling, the microelectrodes were attached to a 0.25mm diameter stainless steel wire with a UV-curable, medical-grade adhesive (MD-1187-M, Dymax, Torrington, CT) at the bond pads. All electrodes were cleaned by immersion in 70% ethanol and rinsed several times in sterile DI water, followed by sterilization with ethylene oxide. Sterilized samples were allowed to outgas for at least 48hrs prior to implantation.

3.2.2 Animal surgery

All procedures involving animals were conducted in accordance with the University of Utah Institutional Animal Care and Use Committee (IACUC). Methods used were similar to those described previously [109, 111]. Briefly, male Sprague Dawley rats (225-250g, n=4 solid, n=5 lattice) were anesthetized via an intraperitoneal injection of ketamine (65mg/kg), xylazine (7.5mg/kg) and acepromazine (0.5mg/kg). Animals' heads were shaved and disinfected with 70% IPA and betadyne prior to being transferred to a stereotactic frame. A

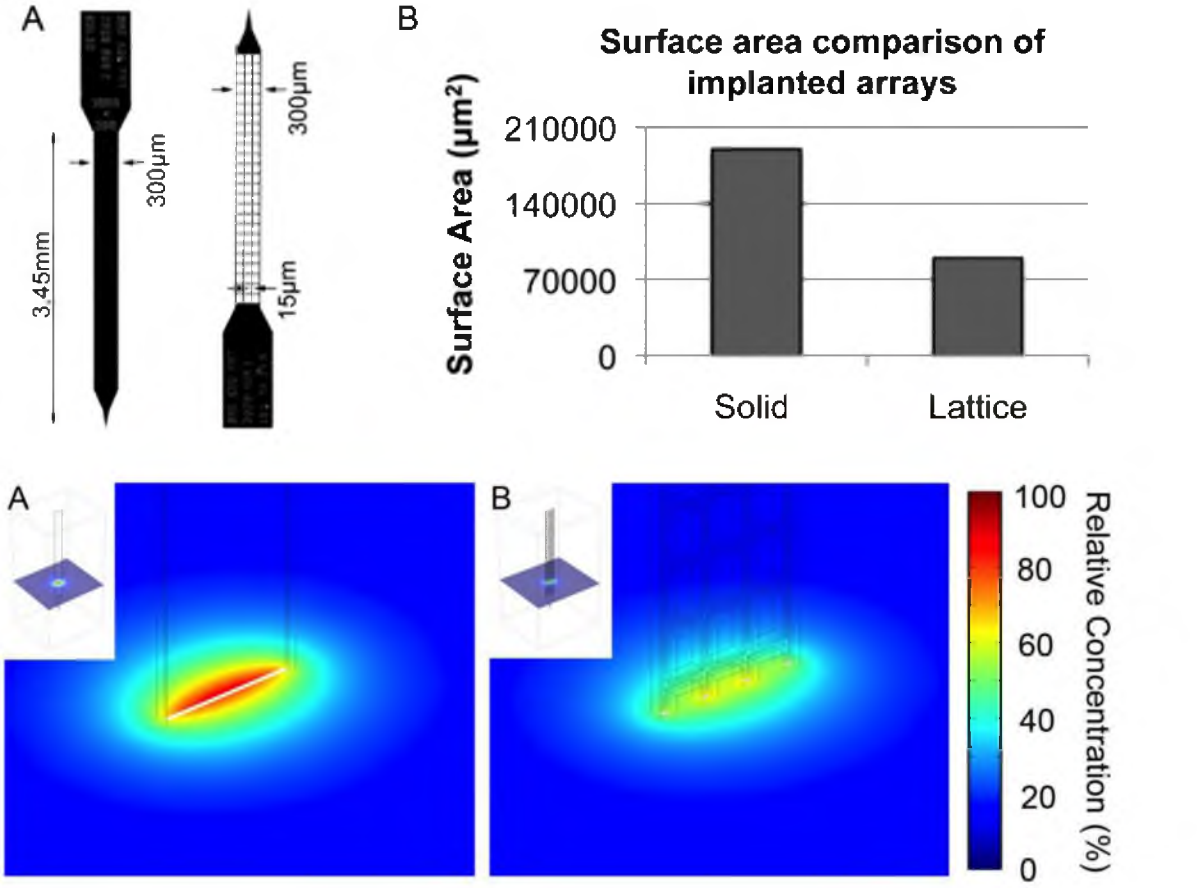

Figure 3-1: (A) Representative images of the 300µm-wide planar solid and 300µm-wide planar lattice microelectrode arrays used in the study. Both styles of electrodes were 12µm thick. (B) Calculated surface area exposed to brain microenvironment when implanted to a depth of 3mm that includes all surface areas measurements including all edges of the lattice. (C & D) 2-D slices showing the predicted TNF-α distribution in cortical layer V surrounding (C) 300µm-wide solid and (D) lattice microelectrode arrays with identical penetrating profiles. Concentrations are set relative to the peak concentration surrounding the solid device.

midline incision, extending the length of the skull, was made along with a 3mm diameter burr hole at -3.2mm of bregma, and 2.0mm lateral to bregma under stereotactic control. A single microelectrode array was stereotactically implanted into each animal with the 300µm-wide faces oriented rostral-caudal, to a depth of 3mm from the top of the cortex, penetrating CA1 of the hippocampus. Electrodes were then fixed to the skull with a custom-fabricated polyurethane grommet using a UV curable, medical-grade adhesive [110, 162].

3.2.3 Euthanasia and tissue processing

At eight weeks postimplantation, animals were terminally anesthetized via an IP injection of ketamine (70mg/kg) and xylazine (30mg/kg) then transcardially perfused with PBS at 50ml/min followed by 4% paraformaldehyde in PBS. Following perfusion fixation, solid electrodes were carefully retrieved from tissue using microdissection forceps while fine surgical scissors were used to cut through the lattice electrodes and release them from their polyurethane grommets, leaving the lattice electrode shanks embedded in brain tissue throughout all subsequent processing steps. Retrieved brains were postfixed with 4% paraformaldehyde for 24hrs at 4°C. Brains were then equilibrated in 30% sucrose. Following equilibration, brains were serially sectioned in the horizontal plane at 30µm thickness with a cryostat (Leica Microsystems, Bannockburn, IL).

3.2.4 Immunohistochemistry

Serial sections were processed using indirect immunohistochemistry for CD68 (ED-1, 0.5mg/ml, AbD Serotec, Raleigh, NC) to assess activated

microglia/macrophages, rat IgG (2.0mg/ml, Southern Biotech, Birmingham, AL) for blood brain barrier dysfunction, GFAP (2.4mg/ml, DAKO, Carpinteria, CA) for astrocytes, and NeuN (2.0mg/ml, Millipore, Billerica, MA) for neuronal nuclei using previously published conditions [109, 111]. In brief, antibodies were diluted in a blocking solution consisting of 4% (v/v) goat serum (Invitrogen, Carlsbad CA), 0.5% (v/v) Triton-X 100, and 0.1% (w/v) sodium azide. Free-floating tissue sections were batch treated for 1hr in blocking solution at room temperature, followed by incubation with primary antibodies overnight at 4°C. After three rinses in PBS at room temperature to remove excess antibody (1hr/rinse), appropriate fluorescently labeled secondary antibodies were applied in block for 1hr at room temperature, followed by three washes in PBS (1hr/rinse). All sections were also counterstained with DAPI (10mM) to identify cell nuclei. Tissue sections were mounted on microscope slides with Fluormount-G (Southern Biotech), and cover-slipped.

3.2.5 Quantitative analysis

Fluorescent images of tissue sections from Layers III - VI of the cortex were captured with a Coolsnap digital camera and a Nikon Eclipse E600 microscope, using identical exposure times and conditions which were optimized for each immunomarker. All fluorescent images were lightfield corrected and background subtracted using primary controls prior to quantification [108].

The staining intensity for each immunomarker was quantified, averaged, and compared using a custom LabView-based image analysis program (National Instruments, Austin TX) as described previously [109, 111, 162]. In brief,

fluorescent intensity as a function of distance from the implant site is extracted using a horizontal array of line profiles spanning the implant site. At each point along the lines, an anti-alias pixel extraction algorithm was used to derive the pixel intensity of the line profile arrays per section. The intensity profiles for a given immunomarker from one section for each layer, III – VI, was averaged to obtain an average intensity profile for a given animal. The average intensity profile for a given animal was then averaged with other animal profiles receiving the same type of implant to obtain an average intensity profile for each cohort (solid or lattice).

In order to quantify changes in neuronal cell body distribution in the presumptive recording zone and in the tissue surrounding the device, the density of neuronal nuclei was calculated by counting the number of NeuN/Dapi+ cells in discrete bins every 50μm from the device interface out to 500μm in what appeared to be normal, undisturbed tissue. The number of neuronal nuclei per bin was then divided by the bin area to determine the average neuronal nuclear density as an estimate of the number of neuronal cell bodies surrounding the device.

3.2.6 Statistical analysis

The area under the curve of each average intensity profile for each immunomarker as well as the average neuronal nuclear density at 50μm intervals from the device interface was compared across cohorts (n=4 for solids and 5 for lattices) using one-way ANOVA and Tukey post-hoc tests (SPSS, IBM, Somers NY), with significance considered at $p < 0.05$. All data are Mean ± Std Dev.

3.3 Results

Consistent with previous reports, explanted 300μm solid microelectrodes had minimal cell attachment (data not shown). These cells were primarily $CD68^+$ with small numbers of $GFAP^+$ cells present. We did not observe any $NeuN^+$ cells attached to explanted microelectrodes. We did, however, observe $DAPI^+$ nuclei that were not associated with either $CD68^+$ or $GFAP^+$ immunoreactivity, indicating the presence of further cell types. We observed no disruption of the tissue interface surrounding sectioned silicon lattice microelectrodes that remained embedded in tissue. Previously, we observed significant amounts of tissue that was immunohistochemically positive for CD68, GFAP, NF200 and MAP-2 associated with other explanted lattice electrode designs.

CD68, a lysosomal enzyme found in activated mononuclear phagocytes, was used to identify microglia/macrophage activation near the implant site of 300μm solid and lattice microelectrode arrays. We observed $CD68^+$ immunoreactivity surrounding both styles of microelectrodes (Figure 3-2A and C). Despite having a larger penetrating profile than previously studied planar solid microelectrode arrays, the distribution of $CD68^+$ tissue surrounding 300μm solid arrays was similar to that described previously [108, 109]. Punctate $CD68^+$ immunoreactivity was primarily localized adjacent to, and within, the electrode track. Immunoreactivity was greatest along the 300μm face of the planar electrode, as opposed to the 12μm edges (Figure 3-2A). For lattice electrodes, we observed punctate $CD68^+$ immunoreactivity primarily at the interface of the 15μm x 12μm silicon ribs and to a lesser extent, spanning the distance between

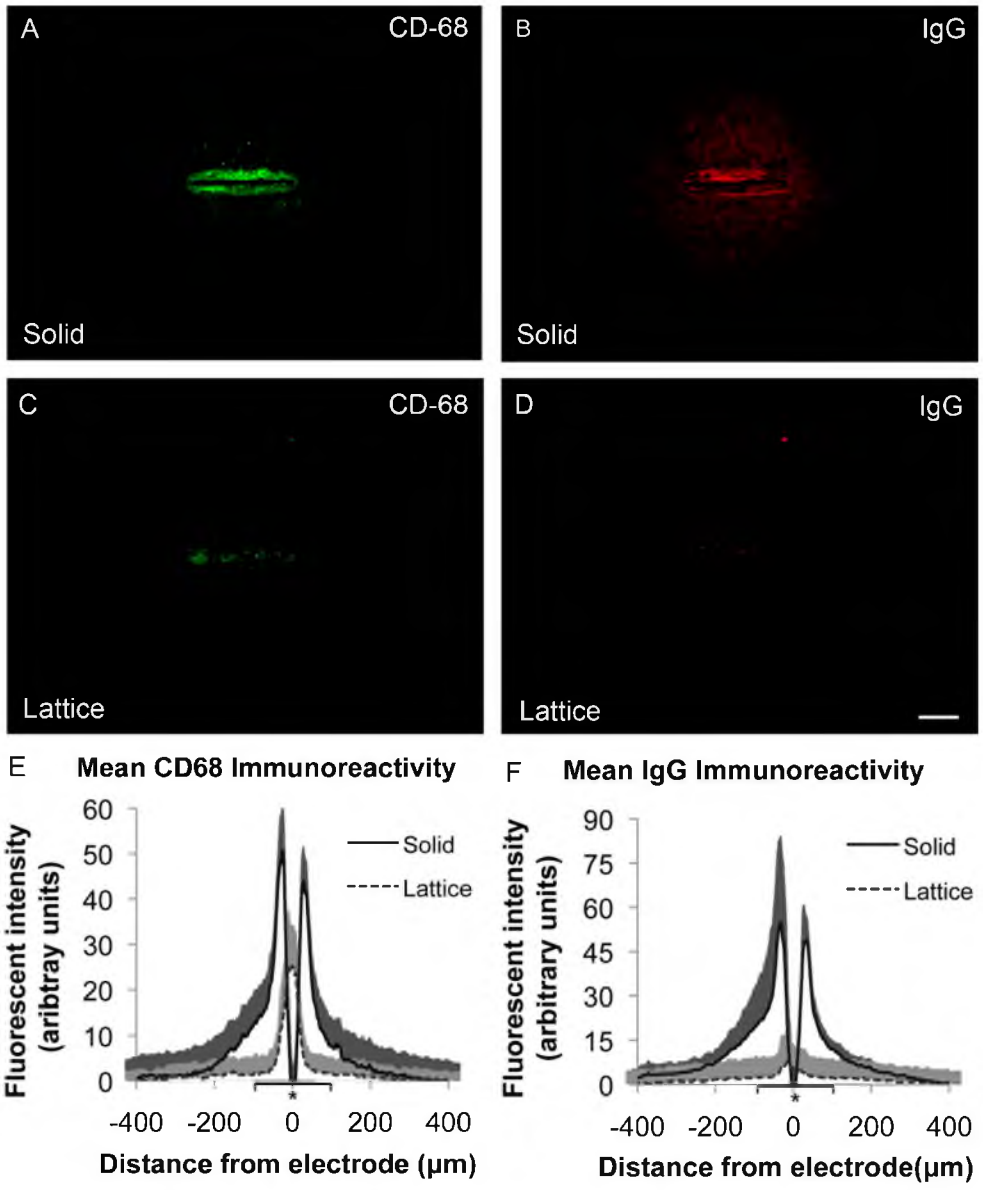

Figure 3-2: Chronic macrophage/microglial response and estimate of blood brain barrier dysfunction adjacent to implanted solid and lattice silicon microelectrode arrays. (A & C) Representative horizontal sections showing CD68 immunoreactivity to (A) 300µm planar solid and (C) 300µm planar lattice arrays. (B and D) Representative horizontal sections through the implantation tract of a 300µm planar, solid shank array (B) and a 300µm planar lattice array (D) showing the distribution of IgG. (E and F) The results of a quantitative image analysis showing that lattice silicon microelectrode arrays with reduced surface area had a significantly reduced macrophage activation and blood brain barrier leakiness to IgG within the presumptive recording zone or first 100µm from the center of the electrode. (*) denotes significant difference with $p<0.05$. Data shown as mean +/- StdDev. Scale bar = 100µm.

ribs (Figure 3-2C). When the relative intensity profiles for CD68 were compared, we observed a significant reduction in immunoreactivity surrounding the 300μm lattice arrays within the first 0-50 and 50-100μm (Figure 3-2E) compared to solid controls.

To assess blood brain barrier dysfunction associated with microelectrode implantation, sections were reacted with antisera against rat IgG. In an uninjured rat cortex, IgG is restricted to the vasculature and removed upon perfusing the animal [152, 153]. However, in cases of blood brain barrier dysfunction, IgG leaks through the vasculature and remains in tissue after perfusion [151]. Figure 3-2B and D show representative images of the IgG immunoreactivity surrounding solid and lattice electrodes, respectively. Lattice micorelectrode arrays showed significantly reduced blood brain barrier dysfunction within the first 100μm from the center of the electrode compared to solid controls (Figure 3-2F).

The astrocyte specific intermediate filament marker GFAP was used to identify astrocytic hypertrophy surrounding implanted devices. Figure 3-3 shows representative images and quantitative analysis of GFAP immunoreactivity near solid and lattice microelectrode arrays. Similar to previous findings, both designs showed diffuse astrocytic hypertrophy near the device [109, 110]. We observed a significant amount of $GFAP^+$ tissue ingrowth through the lattice architecture. Except for this ingrowth, no significant differences were observed in the GFAP immunoreactivity between the two designs.

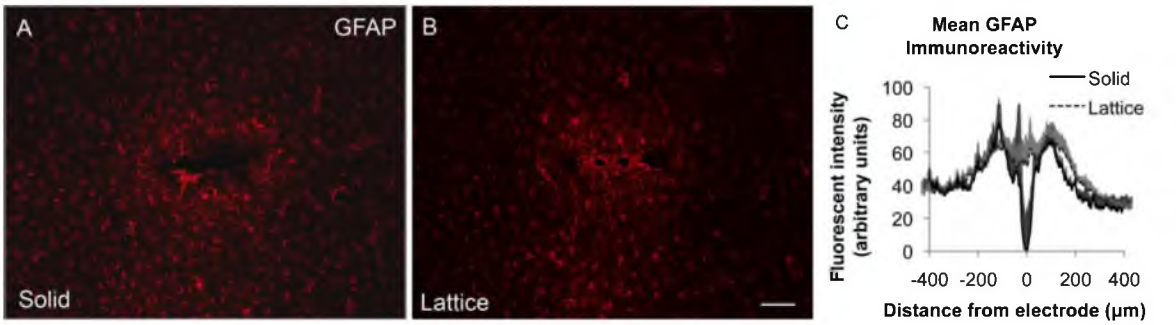

Figure 3-3: Chronic astrocyte response to implanted silicon microelectrode arrays. (A & B) Representative horizontal sections showing GFAP immunoreactivity adjacent to (A) 300μm planar solid and (B) 300μm planar lattice arrays. (C) The results of a quantitative image analysis showing that both designs exhibited astroytic hypertrophy surrounding the device, which differed in the significant amount of tissue ingrowth through the lattice architecture. Data shown as mean +/- StdDev. Scale bar = 100μm.

Antibodies against NeuN were used to examine the density of neuronal cell bodies near implanted devices. Representative images for NeuN immunoreactivity surrounding solid and lattice arrays are shown in Figure 3-4A and B. The density of neuronal nuclei surrounding both styles of devices was quantified in discrete bins every 50μm from the implant site through manual counting and is shown in Figure 3-4C. As observed previously, there was a significant reduction in neuronal cell body density compared to the density in uninjured tissue of approximately 60% and 10% surrounding 300μm solid arrays within the first 50 and 100μm respectively. In contrast, there was significantly less reduction, roughly 10%, surrounding lattice arrays within the first 50μm and no observable reduction between 50-100μm compared to uninjured tissue [108-111].

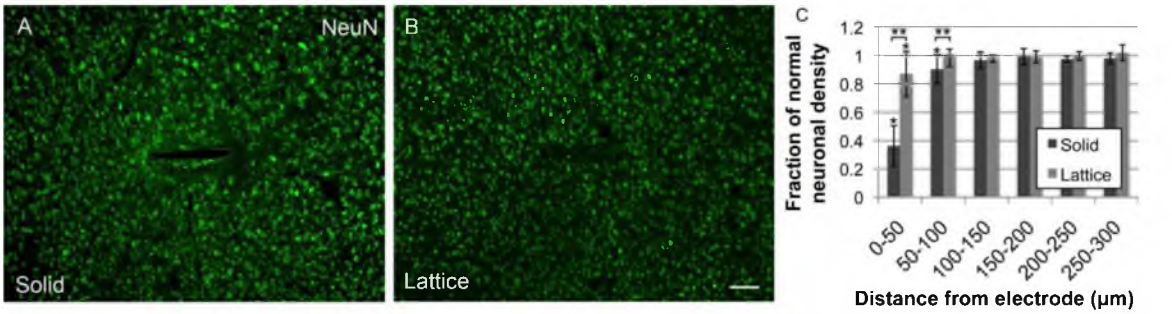

Figure 3-4: Representative horizontal images of NeuN$^+$ nuclei around (A) solid and (B) lattice microelectrodes. (C) Neuronal density is plotted as a function of 50-μm bins from 0 to 250 μm from the microelectrode interface. Values were normalized to the average density of NeuN$^+$ neurons observed in normal tissue 400-500μm from the electrode interface, and are therefore expressed as fraction of control. (*) Denotes significant difference compared to normal neuronal density and (**) denotes differences between solid and lattice cohorts. Both comparisons are $p<0.05$. Data shown as mean +/- StdDev. Scale bar = 100μm.

3.4 Discussion

In this study we demonstrate that altering the exposed surface area of an implanted microelectrode array while maintaining a similar penetrating profile is sufficient to significantly change the classic hallmarks of the chronic FBR including reducing the degree of inflammation, blood brain barrier leakiness and the amount of neuronal cell body loss. Our findings are supported by several recent studies looking at either planar or cylindrical devices [136, 140, 158]. Seymour and Kipke found significant differences in the neuronal and non-neuronal cell response between a parylene-based electrode's larger shank and an adjoining thin lateral platform connected to the main shaft while both Stice et al. and Thelin et al. found significant differences in classic hallmarks of the foreign body response between microwires of different diameters. Our results agree with these observations, and disagree with Szarowski et al. who studied the FBR to a variety of devices with different cross sectional areas, geometries,

and roughnesses and concluded that the tissue response was independent of electrode properties [139]. In contrast to the study by Seymor and Kipke, here we used quantitative methods to investigate specific cellular and molecular features of the FBR rather than quantifying all non-neuronal cells as a single category, which allows us to determine which aspects of the brain FBR are affected by changes in implant architecture. Furthermore by studying the response to two planar devices with identical penetrating profiles we have also negated the influence of implant curvature and the extent of iatrogenic injury that is unavoidable when comparing cylindrical microwire devices of different diameters.

As described earlier, a key feature of the FBR to conventional microelectrode array designs is persistent inflammation at the biotic-abiotic interface signaled by biomarkers for activated microglia and macrophages [108-111, 137]. This observation is also supported by studies showing persistent inflammation surrounding other devices implanted into the central and peripheral nervous systems including Deep Brain Stimulating electrodes [72-80], numerous designs of hydrocephalic shunts [87-90] and peripheral nerve electrodes [182]. In this study we observed a similar pattern of inflammation eight weeks after implantation, a time point when recording inconsistency has been reported. The observation is signaled by similar $CD68^+$ immunoreactivity, surrounding 300μm-wide, planar, solid silicon microelectrode arrays to that described around smaller, 100μm-wide, planar, solid silicon microelectrode arrays [108-111].

The planar, silicon, lattice microelectrode arrays used here had identical penetrating profiles but exhibited significantly less inflammation-related

biomarker distribution in the tissue surrounding the implanted arrays compared to solid shank designs. This finding is supported by in vivo work from Sanders et al. showing that single small-diameter polymer fibers elicit minimal macrophage encapsulation [183]. Additionally, Seymor and Kipke's work showed qualitative differences between macrophage morphology and the amount of CD11b immunoreactivity surrounding different surface geometries contained within the same implant [136]. Sanders et al. suggested that the minimal encapsulation observed in their model may have been caused by a threshold surface area effect, or a critical surface curvature where below a certain threshold of cell–material contact or above a critical curvature, there is insufficient mechanotransduction to induce macrophage activation. Seymor and Kipke also proposed that a critical surface area concept may play a role in their results but favored the theory of mechanical property differences between the adjoining lattice and the primary solid shank as the explanation. We favor a critical surface area concept model. However, we do not believe that differences in mechanics between solid and lattice designs play as large of a role as attributed previously due to the similarity in findings between the soft, flexible parylene/SU-8 based structures used by Seymor and Kipke and our silicon based arrays that are orders of magnitude stiffer.

Our findings support the theory that the FBR is driven by macrophage-secreted factors. Moreover, differences between the FBR to our solid and lattice devices can be explained by our model described in Chapter 2 (Figure 2-8 and Figure 3-1), that takes into account the quantity of soluble factors released by

inflammatory cells interacting with the device surface along with soluble factor diffusive distribution and clearance at the biotic/abiotic interface. Available evidence indicates that these macrophage-secreted soluble factors are responsible for neuronal loss and blood brain barrier dysfunction caused by a mixture of released pro-inflammatory and cytoxic cytokines such as IL-1B, IL-6, and TNF-α. While the cytophysiological sensitivity of adjacent neurons and glial cell types to these and other macrophage-secreted factors has begun to be established, the finer features of the picture are still emerging.

Another specific feature of the brain FBR that we examined in this work was blood brain barrier integrity. Recent studies from our lab have described disruption of blood brain barrier integrity, indicated by the presence of autologous IgG in the brain parenchyma, surrounding both microwire and planar silicon recording devices [109, 111]. Under normal conditions autologous IgG is excluded from the brain parenchyma but has been observed following BBB disruption [151-153]. This disruption of the BBB alters the local ionic milieu and may influence chronic recording consistency through neuronal silencing or alterations in conduction velocity. Similar to previous studies from our group, we observed significant BBB disruption, indicated by the presence of autologous IgG in the brain parenchyma, surrounding solid arrays with significantly less disruption, surrounding planar lattice microelectrodes with reduced surface area.

In accordance with our previous findings, the observed immunoreactivity for autologous IgG surrounding both styles of implanted arrays roughly colocalized with CD68 immunoreactivity [109, 111]. This observation and that of

decreased BBB disruption surrounding the lattice implants that also exhibited reduced macrophage activation, further support our idea that macrophage-released factors and macrophage trafficking to and from the implant though adjacent post-capillary venules [184, 185] may underlie changes in BBB integrity, as well as explain some observations labeled as recording inconsistency.

Consistent with previous studies of neuronal viability surrounding recording devices, we observed a reduction in neuronal nuclei within the recoding zone surrounding solid arrays [105, 109-111, 133, 135, 137, 138, 186]. We found a more normal distribution of neuronal nuclei surrounding the lattice microelectrode arrays compared to solid devices of the same size and shape. This observation of reduced neuronal loss surrounding implants with reduced macrophage activation also supports our group's hypothesis that implant design can be used to reduce the amount of macrophage activation at the biotic-abiotic interface and reduce the impact of their released factors, which should improve recording consistency and the lifetime of implanted microelectrode arrays.

Of interest was our observation that, except for astrocytic integration through the lattice structure, we found no significant difference between the relative GFAP intensity between the two designs studied. The relative intensity and spatial distribution of GFAP immunoreactivity was similar to that seen with other types of devices implanted in the CNS [134]. Astrocyte hypertrophy surrounding implanted microelectrodes has been put forward as a major contributor to chronic recording inconsistencies and failure [100]. Previous work from our lab using single microwires and single shaft, planar silicon

microelectrode arrays indicated that the spatial distribution of GFAP does not increase with time over the indwelling period and did not support the "increase in astrogliosis over time hypothesis" as a dominant or general biologically-related failure mechanism for this type of microelectrode recording device [109, 111]. It is not clear if this observation will hold for multishaft penetrating arrays with more complicated geometries.

With regards to the observed integration of astrocytes through the device, Seymor and Kipke have suggested that this response may better anchor lattice architectures in place [136]. However, it should also be noted that complications might arise from the significant amount of tissue integrated through the lattice structure if the device ever needs to be explanted due to infection or other adverse clinical events, especially with larger multishank devices. Therefore, further efforts may be needed to find alternative methods other than open lattice architectures to reduce device-associated inflammation while preventing significant tissue ingrowth and the complication associated with implant retrieval should that be necessary.

3.5 Conclusion

In this study we show that it is possible for electrode developers to modulate specific aspects of the brain tissue FBR by intentionally manipulating the shape of the implant. The results of our work also support our theory that the FBR to implanted electrode arrays, and likely other devices, can be explained by the persistence of activated macrophages at the biotic-abiotic interface, which act as a sustained delivery source of bioactive agents that diffuse into the adjacent

tissue and shape other features of the FBR including recruitment of macrophages, BBB dysfunction, local areas of demyelination, and a sustained reduction in the local number of neuronal cell bodies. Furthermore, our findings suggest that one method to improve recording consistency and lifetime of implanted microelectrode arrays is to design implants that reduce the amount of macrophage activation at the biotic-abiotic interface and/or improve the clearance or impact of their released factors. These results assist in further validating the usefulness of predictive models, described in Chapter 2, to drive future device designs that integrate into the body and avoid the FBR.

CHAPTER 4

PERMEABLE CYTOKINE SINKS: A NEW APPROACH TO PASSIVELY REDUCE INFLAMMATION SURROUDING BIOMEDICAL DEVICES IMPLANTED IN THE CNS

4.1 Introduction

All chronic indwelling, biomedical devices implanted in the CNS would benefit from approaches that reduce chronic neuroinflammation at the brain tissue-device interface including hydrocephalic shunts, drug delivery systems, nerve regeneration substrates, deep brain stimulating (DBS) electrodes and chronic recording devices. Not only does persistent inflammation affect the function and viability of nearby tissue, but recent evidence suggests that it may impact cognitive function by reducing neurogenesis at more distant sites in the brain [81-85, 91-93]. Available evidence indicates that macrophage-secreted factors at the biotic-abiotic interface are likely responsible for the negative inflammatory sequelae.

Based on this assumption, implant designs that reduce the concentration and impact of inflammatory soluble factors should reduce gliosis, blood brain barrier (BBB) dysfunction, loss of neural cells and their more distant impact on

neurogenesis. To explore this hypothesis, we studied the chronic brain tissue response to planar, solid silicon microelectrode arrays with thick hydrogel coatings (cytokine permeability sinks) designed to passively absorb pro-inflammatory factors (released by reactive immune cells) into the device and away from adjacent brain tissue. Based on the fact that such molecules have a short biological half-life [173, 174], even absorbing these molecules into the permeable coatings for a short period of time will reduce their impact on the surrounding tissue. Using quantitative immunohistochemical approaches the FBR to these devices was compared to that surrounding uncoated cohorts as well as arrays with a thin nanoscale hydrogel coating, serving as a surface chemistry and functional sink control.

4.2 Methods

4.2.1 Microelectrodes:

Solid 300μm wide silicon microelectrode arrays, identical to those used in Chapter 3, were supplied by the Center for Wireless Integrated Microsystems at the University of Michigan. To facilitate handling, we attached the microelectrodes to a 0.25mm diameter stainless steel wire with a UV-curable, medical-grade adhesive (MD-1187-M, Dymax, Torrington, CT). We cleaned all electrodes by immersion in 70% ethanol followed by several rinses in sterile DI water. Following cleaning, we sterilized the devices with ethylene oxide. Sterilized samples were allowed to outgas for at least 48hrs prior to functionalization or implantation. An example electrode is shown in Figure 4-1.

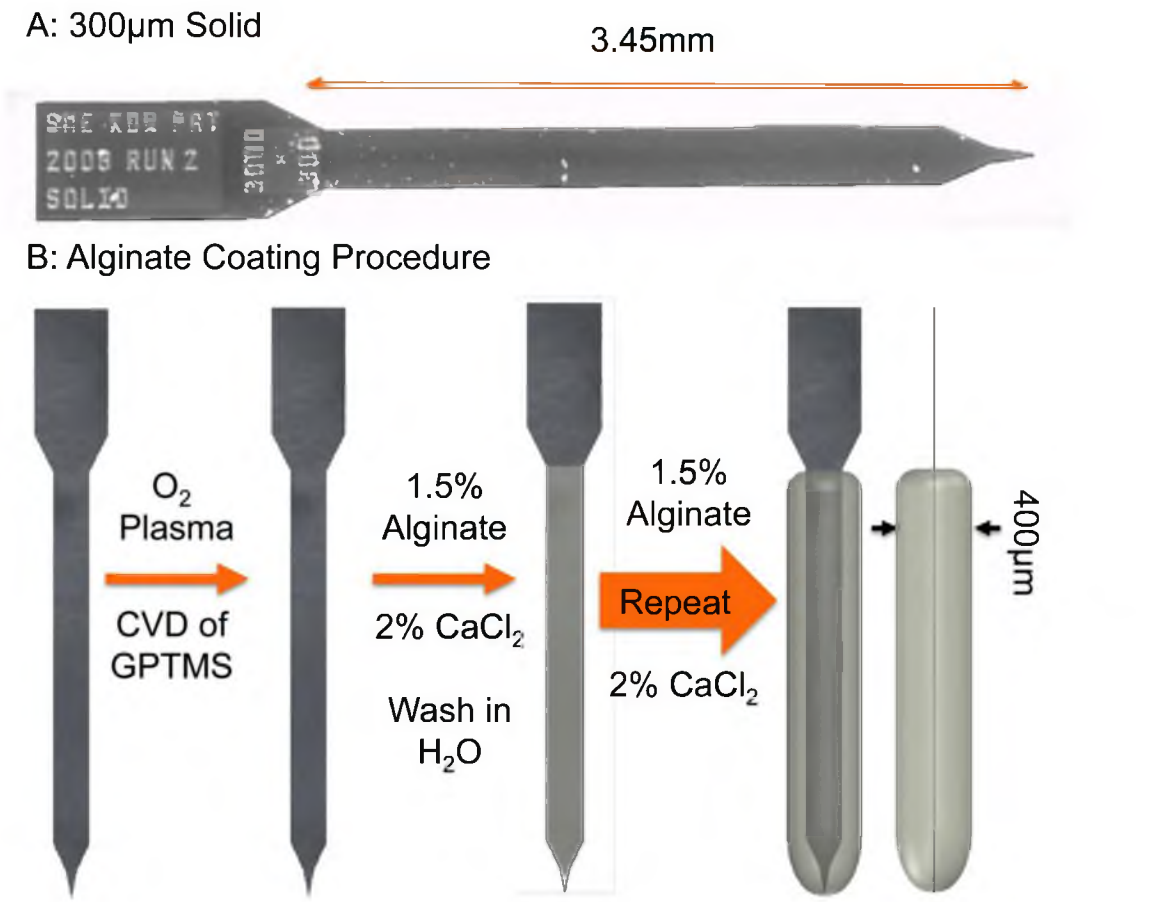

Figure 4-1: (A) Representative image of the 300µm-wide, 12µm-thick, planar microelectrode used in this study. (B) Overview of our procedure for coating the device with a nanoscale and a 400µm-thick alginate coating. To improve integrity of the nanoscale coating we covalently coupled the polysaccharide to the electrode surface using silane chemistry. The divalent cation Ca^{2+} was used to induce gelation in the negatively charged alginate. Approximately 20 cycles through our coating scheme was necessary to achieve the desired gel thickness of 400µm.

4.2.2 Alginate hydrogel coating

To couple our alginate-hydrogel to the surface of the electrodes we first functionalized the surface with an epoxy-silane (3glycidoxypropyl-trimethoxy-silane) via a sterile chemical vapor deposition at 120°C in a N_2 atmosphere for 18hrs [187, 188]. After functionalization we repetitively dipped the electrodes in a sterile 1.5% (w/v) sodium alginate/DI H_2O solution followed by immersion in a sterile 2% (w/v) $CaCl_2$/DI H_2O solution until the desired coating thickness was achieved. This calcium concentration was used to match the concentration within cerebral spinal fluid (CSF), better ensuring that the coating would not degrade or change volume due to calcium flux following implantation. The coating scheme is diagramed in Figure 4-1. We confirmed the presence and thickness of the nanoscale alginate coatings using X-ray photoelectron spectroscopy (XPS) and ellipsometry, respectively. For the thicker alginate coating the gel thickness (≈400μm diameter through the 300μm wide face) was measured via light microscopy. This thickness was determined based on findings from our predictive models described in Chapter 2. Figure 4-2 reviews our modeling predictions for these devices as well as comparing the overall presented surface area and the number of activated macrophages expected at the device interface.

4.2.3 Animal surgery

We implanted three cohorts including an uncoated 300μm-wide solid, a solid with a nanoscale alginate coating (surface chemistry control), and a solid with a 400μm-thick alginate coating. N=8 animals per group with each animal receiving only a single implant.

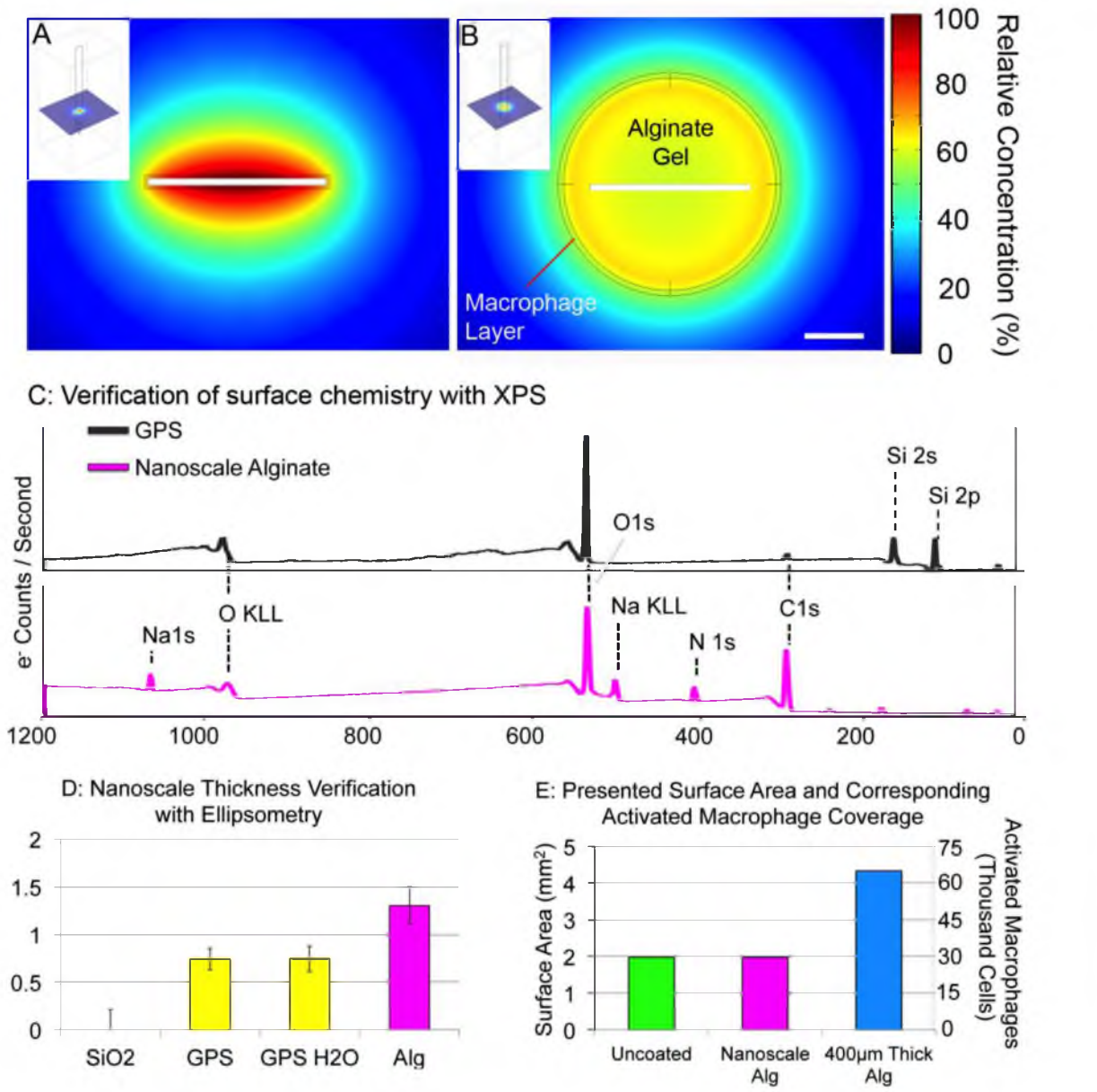

Figure 4-2: (A & B) Relative TNF-α distribution surrounding (A) an uncoated 300µm solid array (a near identical distribution was observed around solid array with a nanoscale alginate coating) and (B) a 400µm thick alginate coated solid. (C) To verify changes in the surface chemistry we used XPS. Following functionalization with alginate we measured an increase in the relative amount of carbon and a decrease in the amount of silicon on the device surface. We also observed new peaks corresponding to sodium and nitrogen in our alginate coatings. (D) To measure the nanoscale alginate coating's thickness we used ellipsometry. (E) Comparison of the presented surface area and the expected activated macrophage coverage for the various electrode cohorts studied.

4.2.4 Euthanasia and tissue preparation

Methods used were similar to those described in Chapter 3 with minor differences. At 16 weeks postimplantation, we terminally anesthetized our animals via 5% isoflurane administration then transcardially-perfused the animals with PBS at 50ml/min followed by fixation with 4% paraformaldehyde in PBS. Following perfusion fixation all electrodes were cut free from their polyurethane grommets, leaving the electrode shanks embedded in brain tissue throughout all subsequent processing steps. Retrieved brains were postfixed with 4% paraformaldehyde for 24hrs at 4°C. Brains were then equilibrated in 30% sucrose. Following equilibration, brains were serially sectioned in the horizontal plane at 30μm thickness with a cryostat (Leica Microsystems, Bannockburn, IL).

4.2.5 Immunohistochemistry

Serial sections were processed using indirect immunohistochemistry for CD68 (ED-1, 0.5mg/ml, AbD Serotec, Raleigh, NC) to assess activated microglia/macrophages, IBA-1 (0.5mg/ml, Wako, Richmond, VA) for all macrophages/microglia regardless of activation state, rat IgG (2.0mg/ml, Southern Biotech, Birmingham, AL) for blood brain barrier dysfunction, GFAP (2.4mg/ml, DAKO, Carpinteria, CA) for astrocytes, and NeuN (2.0mg/ml, Millipore, Billerica, MA) for neuronal nuclei using previously published conditions [189]. In brief, antibodies were diluted in a blocking solution consisting of 4% (v/v) goat serum (Invitrogen, Carlsbad CA), 0.5% (v/v) Triton-X 100, and 0.1% (w/v) sodium azide. Free-floating tissue sections were batch treated overnight in blocking solution at room temperature, followed by overnight incubation with primary

antibodies also at room temperature. After three rinses in 1xPBS at room temperature to remove excess antibody (1hr/rinse), appropriate fluorescently labeled secondary antibodies were applied in block for 24hrs at room temperature, followed by three washes in PBS (1hr/rinse). All sections were also counterstained with DAPI (10mM) to identify cell nuclei. Tissue sections were mounted on microscope slides with Fluormount-G (Southern Biotech), and cover-slipped. Similar methods were used as described in Chapter 3 for fluorescence quantification and analysis [108-111, 189].

4.3 Results

We covalently coupled nanoscale alginate coatings to the electrode surface using silane chemistry [187, 188]. The presence of the coating was confirmed using XPS. Figure 4-2 shows representative XPS spectra for devices receiving only the silane treatment as well as both the silane and nanoscale alginate coating. Following functionalization with alginate we measured an increase in the relative amount of carbon and a decrease in the amount of silicon on the device surface. We also observed new peaks corresponding to sodium in our alginate coatings. These peaks were expected as the alginate we used in our coatings comes as a sodium salt.

To measure the nanoscale alginate coating's thickness we used ellipsometry. Figure 4-3 shows changes in coating thickness through the various stages of our coating scheme. Our measured thickness changes correspond well with similarly coupled dextran coatings [187, 188]. To create an alginate coating that was 400μm in diameter took approximately 20 cycles through our coating scheme of

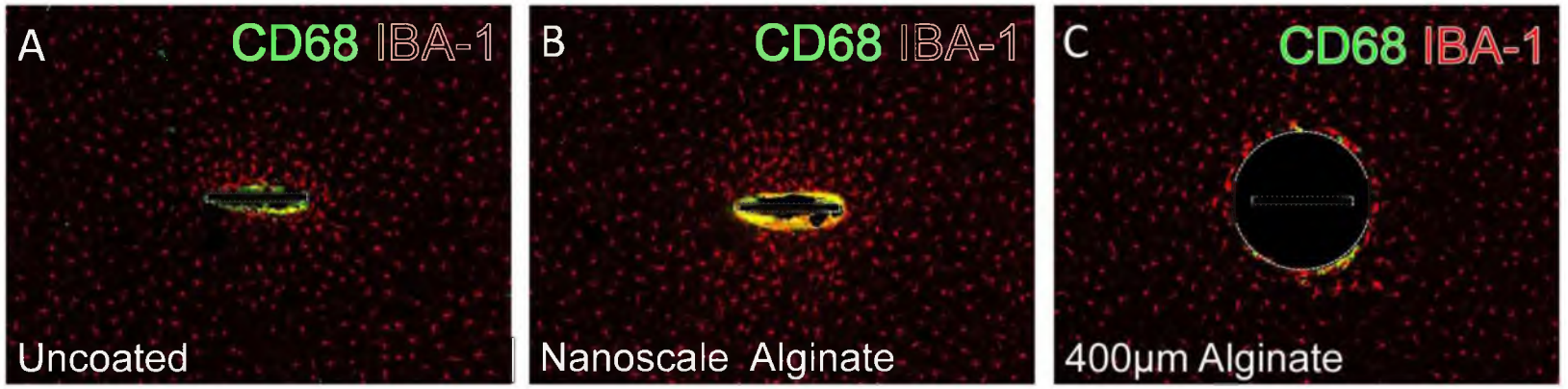

Figure 4-3: (A-C) Representative 16-week horizontal sections showing immunoreactivity for CD68 (activated macrophages) and IBA-1 (all macrophages regardless of activation state) surrounding (A) uncoated, (B) nanoscale coated and (C) 400µm thick alginate-coated solid arrays. Scale bar = 100µm.

1.5% sodium alginate followed by 2% $CaCl_2$. The final coating thickness was verified using light microscopy. The thickness of our 400μm diameter coating did not significantly change after a three month incubation at 37°C in DMEM F12 with 2% $CaCl_2$ indicating the robustness of our coating in an environment with similar Ca^{2+} concentration as the rat brain (data not shown).

In contrast to the majority of studies in the field, we left all electrodes in place following perfusion and through all subsequent processing steps including cryosectioning and immunostaining. We observed little to no disruption of the device/tissue interface in our sections indicating that our findings may provide a more accurate depiction of the interface than previous studies from our lab and others in which devices were removed prior to processing [108-111, 139].

CD68, a lysosomal enzyme found in activated mononuclear phagocytes, was used to identify microglia/macrophage activation near the implant site of our uncoated and coated 300μm solid arrays. We observed $CD68^+$ immunoreactivity surrounding all cohorts (Figure 4-3). Despite having a larger penetrating profile than previously studied planar solid microelectrode arrays, the distribution of $CD68^+$ tissue surrounding 300μm solid arrays was similar to that described previously for 100μm wide planar MI-arrays [108, 109]. Moreover, the distribution appeared similar to that surrounding identical devices implanted for eight weeks [189]. Punctate $CD68^+$ immunoreactivity primarily localized and was greatest along the 300μm face of the planar electrode, as opposed to the 12μm edges. We observed similar immunoreactivity surrounding electrodes that received a nanoscale coating of alginate. In contrast, when the gel thickness was increased

to 400μm we observed a significant decrease in $CD68^+$ immunoreactivity within the first 0-50 and 50-100μm (Figure 4-4) compared to both uncoated solids and the nanoscale coated controls.

To further assess the macrophage response surrounding these cohorts of devices we used IBA-1, a pan-macrophage marker found in the membrane of these cells (Figure 4-3). We observed an increase in $IBA\text{-}1^+$ immunoreactivity surrounding both the uncoated solids and the nanoscale controls compared to normal tissue approximately 350-400μm away from the device interface. These findings could indicate macrophage/microglial trafficking to and from the implant interface. Conversely, with devices that received a thick coating of alginate we observed a significant reduction in IBA^+ immunoreactivity compared to control tissue that was 500μm away from the interface of the thick alginate gels (Figure 4-5).

To examine blood brain barrier dysfunction associated with microelectrode implantation, sections were reacted with antisera against rat IgG. In an uninjured rat cortex, IgG is restricted to the vasculature and removed upon perfusing the animal [152, 153]. Alternatively, in cases of blood brain barrier dysfunction, IgG leaks through the vasculature and remains in tissue after perfusion [151]. Figure 4-6 shows representative images of the IgG immunoreactivity surrounding our three cohorts of implanted devices. We observed a significant reduction in blood brain barrier dysfunction within the first 100μm from device interface of our 400μm thick alginate coated devices compared to uncoated and nanoscale coated controls (Figure 4-7).

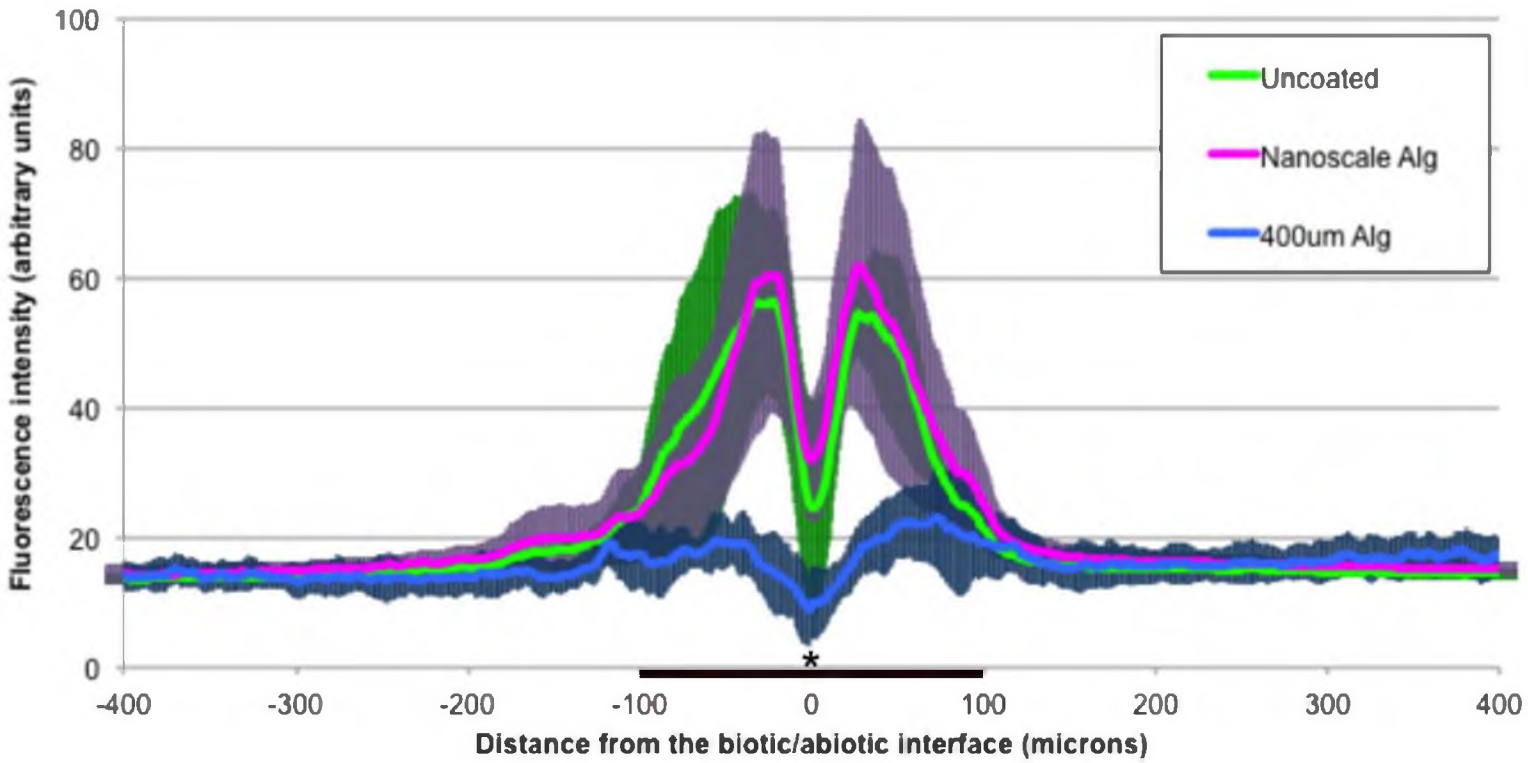

Figure 4-4: The results of quantitative image analysis showing that 400µm alginate coated device had significantly reduced $CD68^+$ immunoreactivity within the presumptive recording zone (i.e. first 100µm from the center of the electrode). (*) denotes significant difference with $p<0.05$. Data shown as mean +/- StdDev.

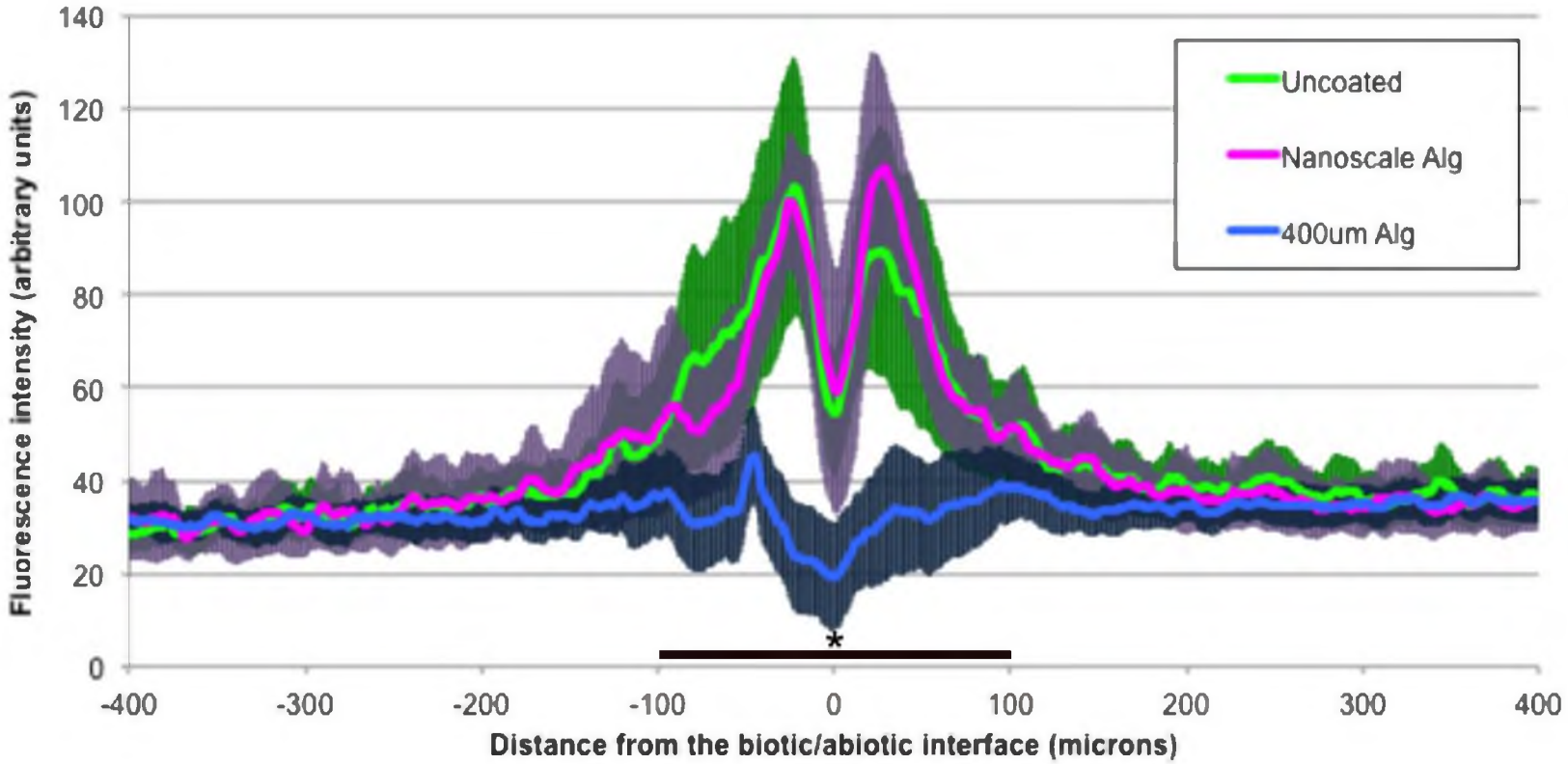

Figure 4-5: The results of quantitative image analysis showing that 400µm alginate coated device had significantly reduced IBA-1$^+$ immunoreactivity within the presumptive recording zone (i.e. first 100µm from the center of the electrode). (*) denotes significant difference with $p<0.05$. Data shown as mean +/- StdDev.

Figure 4-6: (A-C) Representative 16-week horizontal sections showing immunoreactivity for IgG (blood brain barrier dysfunction) surrounding (A) uncoated, (B) nanoscale coated and (C) 400µm thick alginate-coated solid arrays. Scale bar = 100µm.

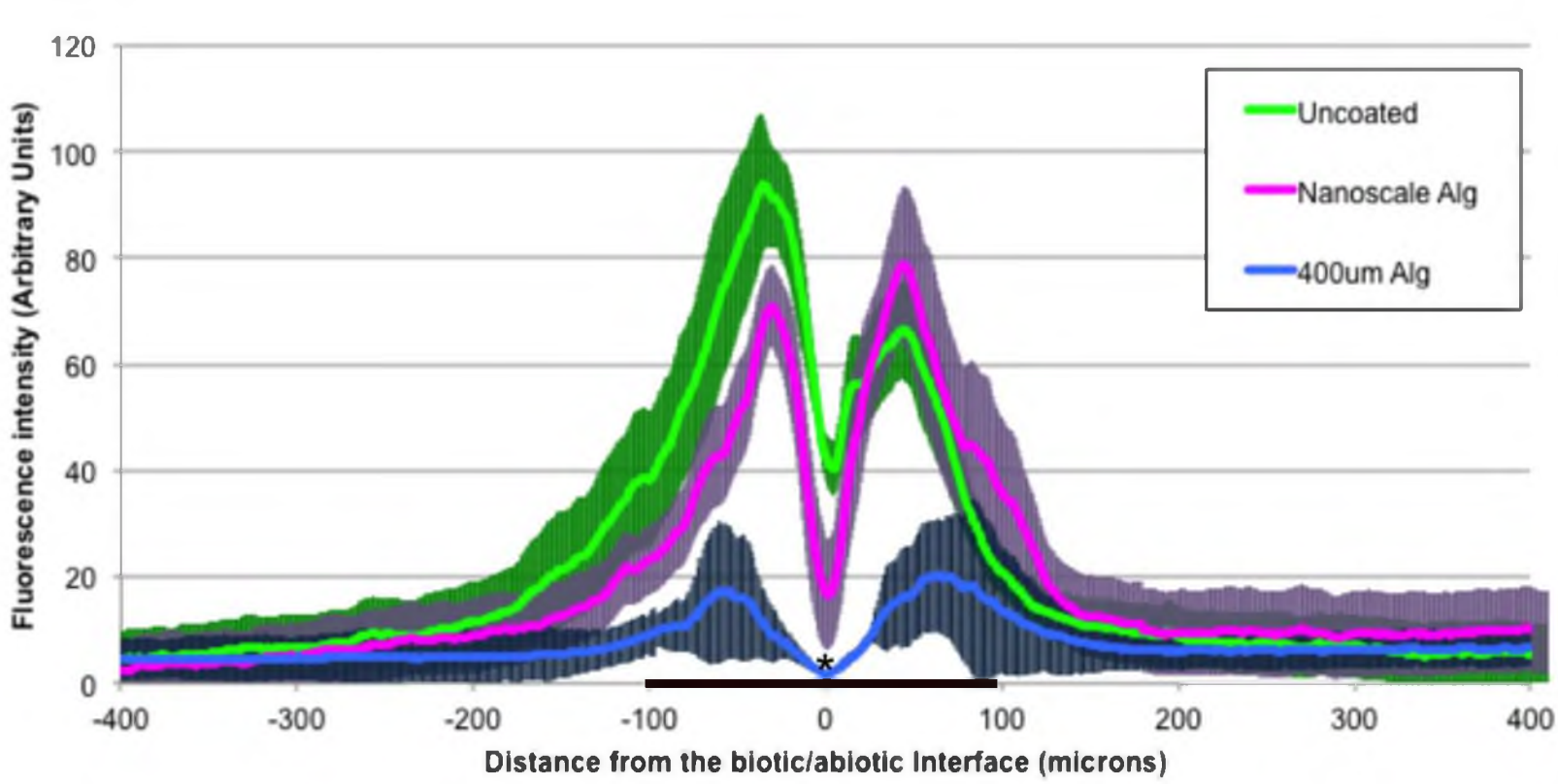

Figure 4-7: The results of a quantitative image analysis showing that 400µm alginate-coated device had significantly reduced blood brain barrier dysfunction, as assessed by positive immunoreactivity for extravasated rat IgG, within the presumptive recording zone (i.e. first 100µm from the center of the electrode). (*) denotes significant difference with $p<0.05$. Data shown as mean +/- StdDev.

The astrocyte specific intermediate filament marker GFAP was used to identify astrocytic hypertrophy surrounding implanted devices. Figure 4-8 shows representative images and quantitative analysis of GFAP immunoreactivity surrounding our three device cohorts. Similar to previous findings for identical uncoated devices after eight-weeks implantation, both uncoated and nanoscale coated devices showed diffuse astrocytic hypertrophy near the device [109, 110]. In contrast, there was a significant reduction in astrocyte hypertrophy surrounding devices that received a 400μm thick alginate coating (Figure 4-9).

Antibodies against NeuN were used to identify neuronal nuclei and to examine the density of neuronal cell bodies near implanted devices. Representative images for NeuN immunoreactivity surrounding uncoated solids as well as devices receiving a nanoscale or thick alginate coating are shown in Figure 4-10. The density of neuronal nuclei surrounding both styles of devices was quantified in discrete bins every 50μm from the implant site through manual counting. As observed previously, there was a significant reduction in neuronal cell body density compared to that in uninjured tissue of approximately 60% and 10% surrounding 300μm solid arrays within the first 50 and 100μm, respectively. A similar level of loss was observed surrounding devices receiving a nanoscale alginate coating. In contrast, there was significantly less reduction, roughly 10%, surrounding devices that received our 400μm thick alginate coating within the first 50μm from the gel interface and no observable reduction between 50-100μm compared to uninjured tissue (Figure 4-11) [110].

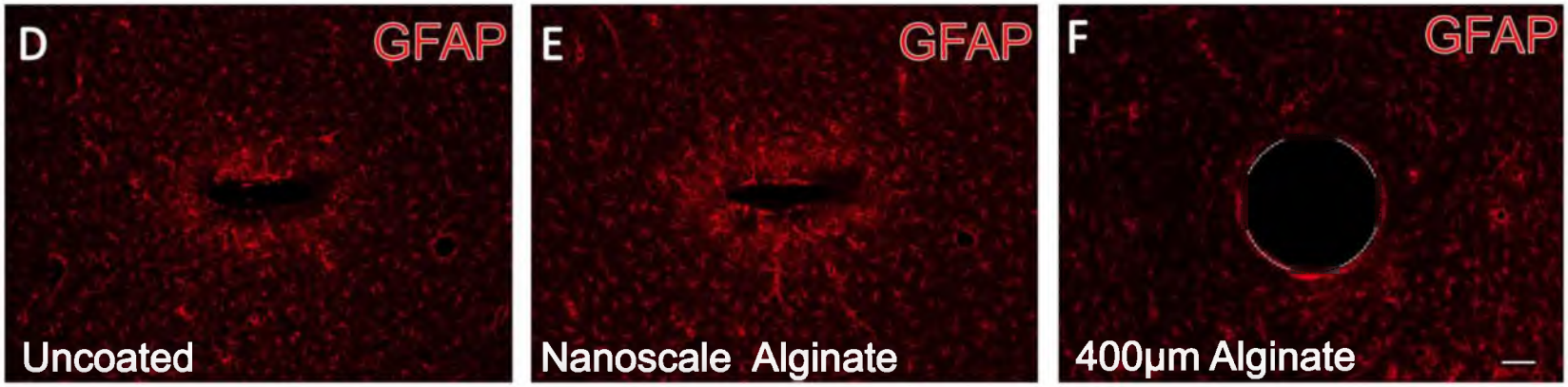

Figure 4-8: (A-C) Representative 16-week horizontal sections showing immunoreactivity for GFAP surrounding (A) uncoated, (B) nanoscale coated and (C) 400µm thick alginate-coated solid arrays. Scale bar = 100µm.

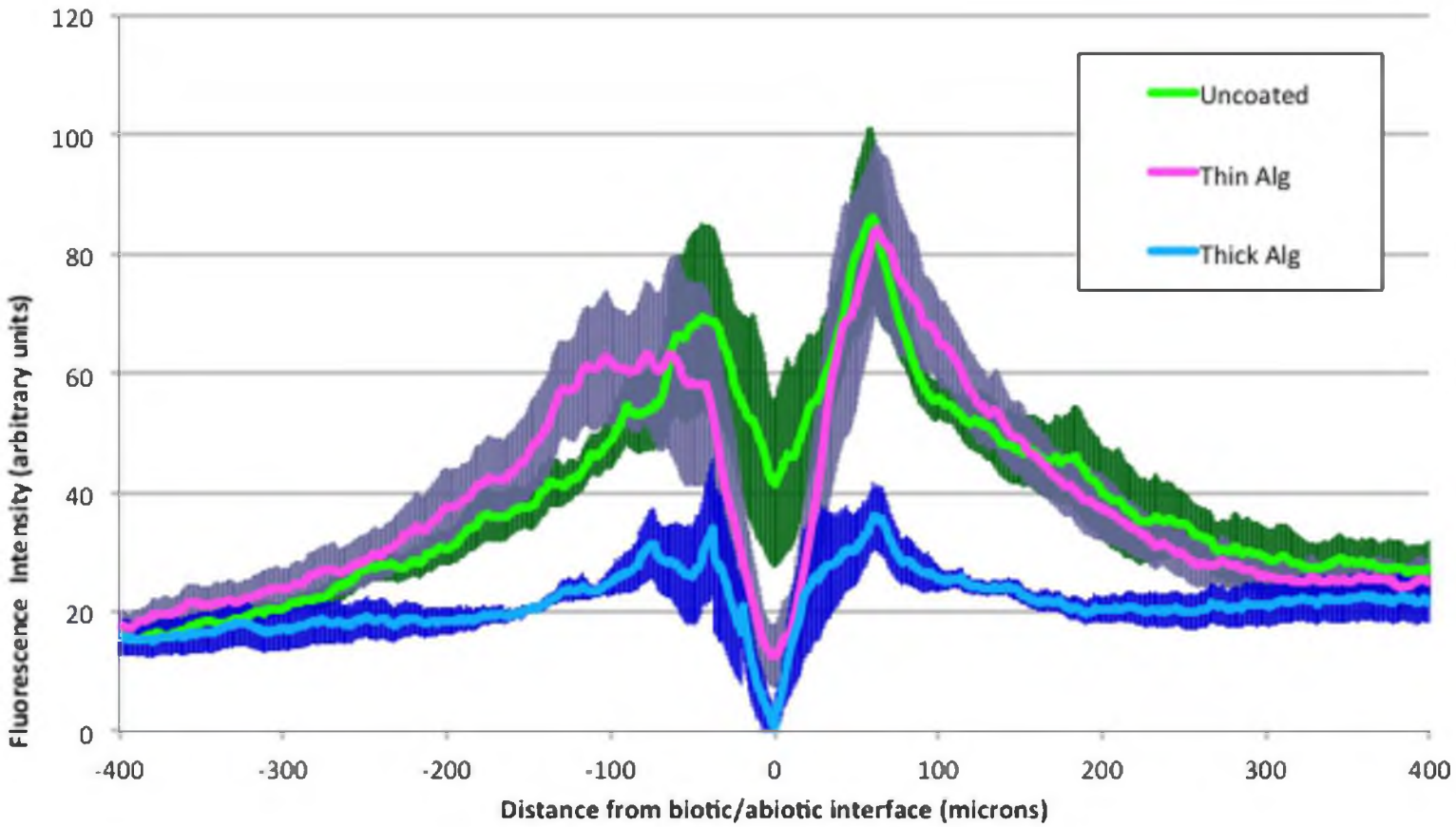

Figure 4-9: The results of a quantitative image analysis showing that 400µm alginate-coated device had significantly reduced GFAP$^+$ immunoreactivity within the presumptive recording zone (i.e. first 100µm from the center of the electrode). (*) denotes significant difference with $p<0.05$. Data shown as mean +/- StdDev.

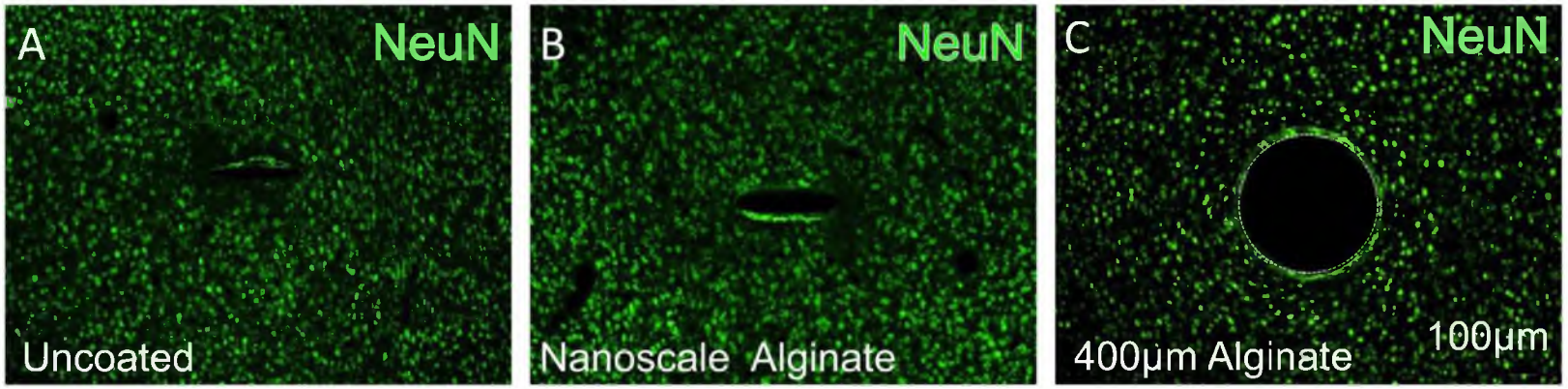

Figure 4-10: Representative horizontal images of NeuN$^+$ nuclei around (A) uncoated solids, (B) devices that received a nanoscale coating of alginate and (C) devices that received a 400µm-thick alginate coating. Scale bar = 100µm.

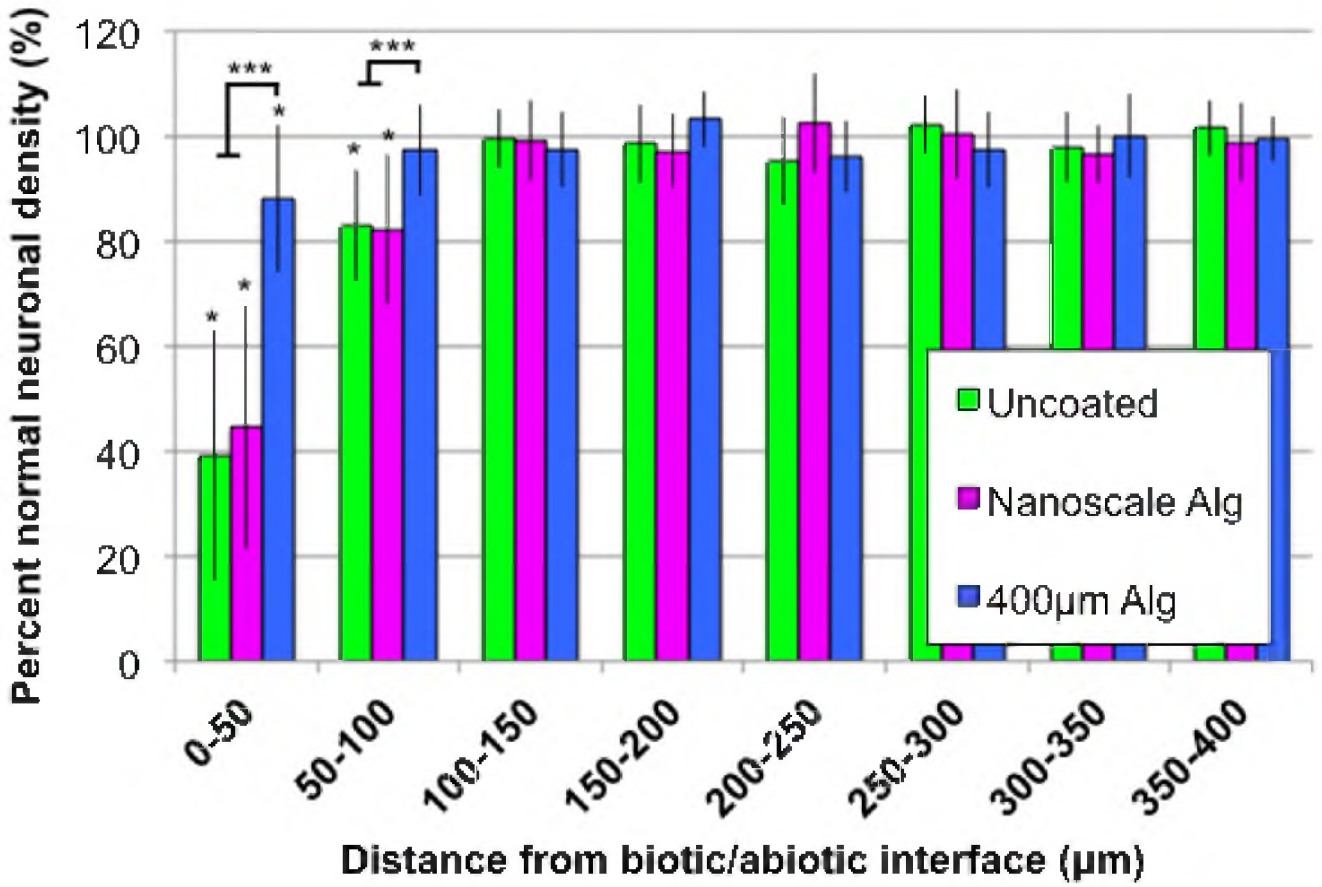

Figure 4-11: Neuronal density as a function of distance from the biotic/abiotic interface in 50-µm bins from 0 to 400µm from the microelectrode interface. Values were normalized to the average density of $NeuN^+$ neurons observed in normal tissue 350-400µm from the electrode interface, and are therefore expressed as percentage of control. (*) Denotes significant difference compared to normal neuronal density and (***) denotes differences between the 400µm alginate-coated devices and the two other cohorts (uncoated and nanoscale coated devices). Both comparisons are $p<0.05$. Data shown as mean +/- StdDev.

4.4 Discussion

In this study we demonstrate that incorporating a permeable cytokine sink coating surrounding an implanted microelectrode array is sufficient to significantly change classic hallmarks of the chronic FBR including reducing the degree of inflammation, decreasing blood brain barrier dysfunction, limiting myelin degradation, decreasing astrocyte hypertrophy, and reducing the degree of neuronal loss. Our findings are supported by results from a number of studies that investigated a variety of semipermeable cell encapsulation devices and small metabolite sensors implanted in various tissues. For example, in our lab we have found a reduced FBR surrounding semipermeable hollow fiber membranes (HFMs), a type of cell encapsulation technology that is composed of a porous polymer wall structure surrounding a hollow lumen (see Figure 2-8) [177]. Additionally, work by La Flame et al. showed a similar reduction in the FBR, as well as complement activation, to stiff silicon and metal membranes with a similar nanoporous structure to our HFM systems used in novel implantable glucose sensor designs and cell encapsulation constructs [190, 191]. While all of these studies using semipermeable materials describe a reduction in inflammation and the FBR, our current study is the first to describe a common driving mechanism for how this could be occurring based on their role as cytokine sinks that passively reduce the distribution of macrophage-released factors in the surrounding tissue.

As stated previously in this work, a number of theories have been put forward to describe the driving mechanisms that perpetuate the FBR. One of the major

theories that is gaining traction in the field is that perpetuation is due to a mismatch in mechanical properties between the stiff implanted material and the softer brain tissue, leading to repetitive, micromotion-induced damage at the biotic/abiotic interface [133, 159]. While better mechanical matching between our soft hydrogel and the surrounding brain tissue may contribute to reductions in the FBR surrounding our 400μm thick alginate coatings, the similarities of findings of the FBR to stiff semipermeable silicon devices suggests that mechanical matching is not the only factor involved. Additionally, these similarities in the FBR to devices of varying stiffness could suggest that micromotion may not play as large a role in perpetuating the FBR as previously hypothesized. Or, alternatively, these findings could indicate that while micromotion induced damage perpetuates the FBR that these semipermeable materials sufficiently reduce the impact of macrophage-released factors on the surrounding tissue to a degree that resulting hallmarks of the FBR are marginalized.

As described earlier, a key feature of the FBR to conventional microelectrode array designs is persistent inflammation at the biotic-abiotic interface signaled by biomarkers for activated microglia and macrophages [105, 108-111, 189]. This observation is supported by studies showing persistent inflammation surrounding other devices implanted into the central nervous system including deep brain stimulating electrodes and hydrocephalic shunts [36, 72-80, 87-89]. We have previously described that the distribution of $CD68^+$ immunoreactivity does not change from four to 12 weeks postimplantation [109, 111]. The similarity between our 16-week results and the distribution of $CD68^+$ immunoreactivity surrounding

identical devices at eight-weeks postimplantation [189] further supports the theory that chronic inflammation persists through the entire indwelling duration of implant.

Despite having a large penetrating profile, we observed a reduction in the $CD68^+$ and IBA^+ immunoreactivity surrounding our devices that received a thick coating of alginate. As we described in Chapters 2 and 3, we believe that presented surface area can play a large role in the severity of the FBR. The fact that our devices with a thick alginate coating, which effectively doubled their presented surface area, showed a decreased FBR further indicates the power of permeable cytokine sinks or other methods of antagonizing macrophage-released factors to modulate the FBR.

Another specific feature of the brain FBR we examined in this work was blood brain barrier integrity. Recent studies from our lab have described disruption of blood brain barrier integrity, indicated by the presence of autologous IgG in the brain parenchyma, surrounding both microwire and planar silicon recording devices [109, 111, 189]. Under normal conditions autologous IgG is excluded from the brain parenchyma but has been observed following BBB disruption [152, 153]. This disruption of the BBB alters the local ionic milieu and may influence chronic recording consistency through neuronal silencing. Similar to previous studies from our group we observed significant BBB disruption, indicated by the presence of autologous IgG in the brain parenchyma, surrounding both uncoated solid arrays and those that received a nanoscale coating with significantly less disruption surrounding planar microelectrodes with reduced surface area [189].

In accordance with our previous findings, the observed immunoreactivity for autologous IgG surrounding both styles of implanted arrays roughly colocalized with CD68 immunoreactivity [109, 111]. This observation and that of decreased BBB disruption surrounding the lattice implants that also exhibited reduced macrophage activation, further support our idea that macrophage-released factors and macrophage trafficking to and from the implant though adjacent postcapillary venules [184, 185] may underlie changes in BBB integrity, as well as explain some observations labeled as recording inconsistency.

In addition to other hallmarks that indicate a reduction in the FBR to our thick alginate coated devices, we also found a significant reduction in the relative GFAP intensity surrounding these devices compared to our other two cohorts. The relative intensity and spatial distribution of GFAP immunoreactivity was similar to that seen with other types of devices implanted in the CNS [105, 108, 110, 133-135, 137-139]. Astrocyte hypertrophy surrounding implanted microelectrodes has been put forward as a major contributor to chronic recording inconsistencies and failure [100] though recent work from our lab has shown evidence that this earlier hypothesis may not play as large a role as previously thought [109, 111].

Consistent with previous studies of neuronal viability surrounding recording devices, we observed a reduction in neuronal nuclei within the recoding zone surrounding solid arrays [105, 108-111, 133, 135, 137, 138]. We found a more normal distribution of neuronal nuclei surrounding the microelectrode arrays that received a 400μm thick alginate coating compared to solid devices with or

without a nanoscale alginate coating. This correlation between improved neuronal density surrounding implants with a reduced inflammatory response supports our group's hypothesis that implant design can be used to reduce the amount of macrophage activation at the biotic-abiotic interface and reduce the impact of their released factors, which should improve recording consistency and the lifetime of implanted microelectrode arrays.

While we have shown the usefulness of thick hydrogel coatings to reduce the FBR to microelectrodes, there are still questions concerning the impact that these types of coatings would have on the ability of the device to record from nearby neurons. Recent work by Rao et al. suggests that these permeable hydrogel coatings may not significantly impact device function, as ion transport is significantly higher through these materials compared to the highly tortuous tissue surrounding the device [192]. This increased ion transport in the gel would extend the effective recording range further than the well accepted 50-140μm maximum recording range for electrodes in direct contact with tissue. If recording ability is impacted there are also a number of strategies that could be implemented to utilize permeable cytokine sinks in recording applications including designing devices with recordings sites placed in proximity to the permeable gel surface using silicon spines (Figure 4-12) or creating permeable membrane electrode arrays that have a similar structure to a HFM with recording sites and leads placed in desired locations along a permeable wall structure surrounding a sufficiently large hollow lumen.

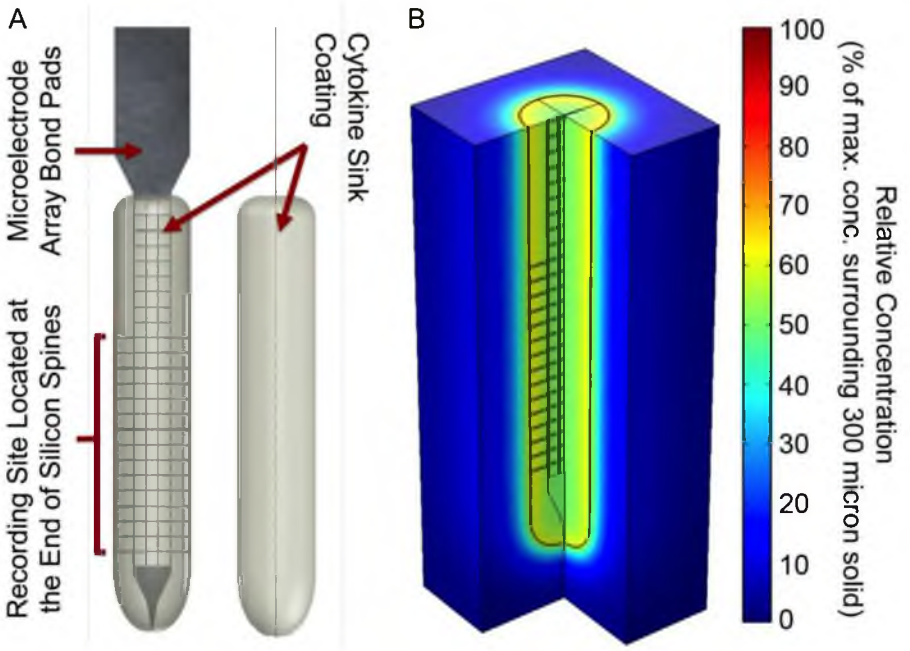

Figure 4-12: (A) Example SolidWork© designs of a novel electrode incorporating a cytokine sink coating while also placing recording sites near neuronal targets using silicon spines that extend toward the gel surface. (B) Predicted distribution of TNF-α surrounding the virtual device. Even though the electrode recording sites are located near the gel surface where activated macrophages would be expected, by maintaining a large permeable volume around the spines we predict that we can minimize the FBR using a cytokine sink strategy.

4.5 Conclusion

In this study we have described a new strategy to reduce the FBR to implanted microelectrodes using permeable cytokine sinks. These sinks were designed to passively reduce the concentration of macrophage-released factors impacting the surrounding tissue by allowing them to diffuse into the device for a sufficient length of time so that they become inactive via hydrolysis and other mechanisms. Our findings provide further evidence that macrophage-released factors are key drivers of the FBR to implanted microelectrodes and that strategies to antagonize their impact on the surrounding tissue will improve this response. Beyond the use of cytokine sinks to improve the FBR to

microelectrode arrays and their recording ability, we believe similar methods could be used to improve the FBR and functionality of a number of device implanted in the CNS.

CHAPTER 5

ASTROCYTE AND GLIAL RESTRICTED PRECURSOR-DERIVED BIOMATERIALS TO IMPROVE THE INTEGRATION OF MEDICAL DEVICES WITH THE CNS

5.1 Introduction

Neural interface devices have the potential to dramatically improve the lives of individuals suffering from a wide range of conditions, including paralysis and sensory and motor deficits. However, the foremost limitation to the clinical implementation of these devices is their failure to achieve high-quality recordings over extended periods of time. The poor recording quality and longevity of microelectrodes is widely believed to be due to poor wound healing and the chronic foreign body response (FBR) surrounding the synthetic materials currently used to fabricate these devices.

In contrast, cell-derived biomaterials composed of extracellular matrix (ECM) components exhibit superior biocompatibility and facilitate improved healing compared to synthetics [193, 194]. A number of ECM products have been developed to repair and regenerate tissues such as myocardium, kidney and

bladder. However, with the exception of the dura, similar materials have not been extensively developed for central nervous system (CNS) regeneration.

When attempting to adapt these materials from the field of regenerative medicine to use as coatings for more classic medical devices, there are a number of concerns that need addressing. For example, while the majority of proteins found in the ECM are well conserved between animals and humans, interspecies differences do exist. As a result, the implantation of even decellularized, xenogenic ECM components elicits an adaptive immune response that could negatively impact device function and health of the surrounding tissue [195-197]. Therefore, the development of approaches for producing autologous or allogenic materials may prove key to improving the clinical success of these types of products [198].

There is also evidence in the field of regenerative medicine that although ECM from various tissues share common protein and glycosoaminoglycan (GAG) components, subtle differences in ECM composition exist that may impact regenerative outcomes and device integration for specific tissues [199]. A number of studies have shown that culturing cells on tissue-specific ECM improves infiltrating cell proliferation rates and increases expression of desired phenotypic cell and tissue characteristics [200-204]. In contrast, other studies have shown that implantation of nontissue specific ECM materials induces the formation of undesired, phenotypically irregular tissue at the implantation site [205, 206].

Adapting regenerative medicine approaches to limit the FBR to microelectrodes has been attempted previously. A number of groups have shown that coating devices with single, isolated components of CNS ECM, such as the proteoglycan laminin (LN) that is produced by astrocytes and other cells, limits the FBR to some degree [164]. However, we believe that presenting a more intact ECM that contains a similar profile of proteins, proteoglycans and gylcosoaminoglycans (GAGs) will improve the efficacy of these types of coatings in reducing the FBR. Work by Tanaka et al. demonstrated that activated microglia cultured on intact monolayers of astrocyte ECM displayed a ramified phenotype similar to the resting phenotype in healthy CNS tissue [207]. In contrast, this group observed that this ramification was greatly diminished in microglia cultured on single isolated ECM components such as fibronectin (FN) or LN. These findings indicate that multiple ECM components help to regulate macrophage activation and that developing coatings that mimic this biocomplexity could further improve the FBR to microelectrode arrays.

To investigate the potential of improving upon this earlier work that used isolated single bioactive molecules and to address the concerns raised with the use of xenogenic and nontissue-specific ECM, we have developed both a novel approach to harvest ECM produced by CNS cells and techniques to covalently immobilize and coat these materials onto silicon microelectrodes. Young immature astrocytes, which are the primary support cell in the CNS, and GRPs, an immature progenitor cell capable of differentiating into astrocytes and oligodendrocytes, were used for ECM production and harvest in this study.

These cells and their produced ECM play important roles in nervous system development, and have been shown to promote regeneration following transplantation into spinal cord injury (SCI) models, and as stated assist in regulating the activation state of microglia [208, 209].

5.2 Methods

5.2.1 Sacrificial substrate preparation

Open-celled polymeric foams (Figure 5-1) were fabricated as previously described [210-212]. In brief, we dissolved pellets of a medical grade poylurethane elastomer (Tecoflex SG-80, Thermedics) in dimethyacetamide (DMAC) (10% w/v) overnight at 60°C. We then added a poloxamer solution (Pluronic 10R5, BASF, Germany) to the dissolved PU (1:2 v/v) and thoroughly mixed the resulting solution. We then cooled the solution to its cloud point at 46°C, and pipetted it into plastic molds. To cause the PU to undergo phase inversion, we rapidly cooled the molds for 2.5mins through surface contact with a dry-ice/ethanol bath, followed by overnight precipitation in DI H_2O. Following phase inversion, the material was removed from the molds, rinsed with multiple washes of DI H_2O for 48hrs, frozen to -80°C, and lyophilized. We sectioned the lyophilized scaffolds into strips (30mm x 10mm X 2mm) and attached them to Mylar mounts using a medical grade, UV curable adhesive (MD 1180-M, Dymax, Torrington, CT). Mounted foams were sterilized using ethylene oxide (EtO). Following EtO sterilization we soaked the foams for 20mins in 70% ethanol to promote wetting, following which we rinsed the foams in sterile DI H_2O. To

promote cellular attachment, we incubated the foams in a fibronectin (FN) solution (20µg/ml in PBS) overnight.

5.2.2 Astrocyte and GRP seeding and culture

Following FN incubation, we seeded PU substrates with either primary astrocytes or GRPs, harvested from Sprague Dawley rats as described previously, at two million cells/cm^3 [208, 213-215]. Astrocyte seeded substrates were cultured for three weeks in DMEM F12 supplemented with 10% fetal bovine serum (FBS) while GRP-seeded substrates were cultured for three weeks in SATO$^-$. We exchanged the culture media every two-three days.

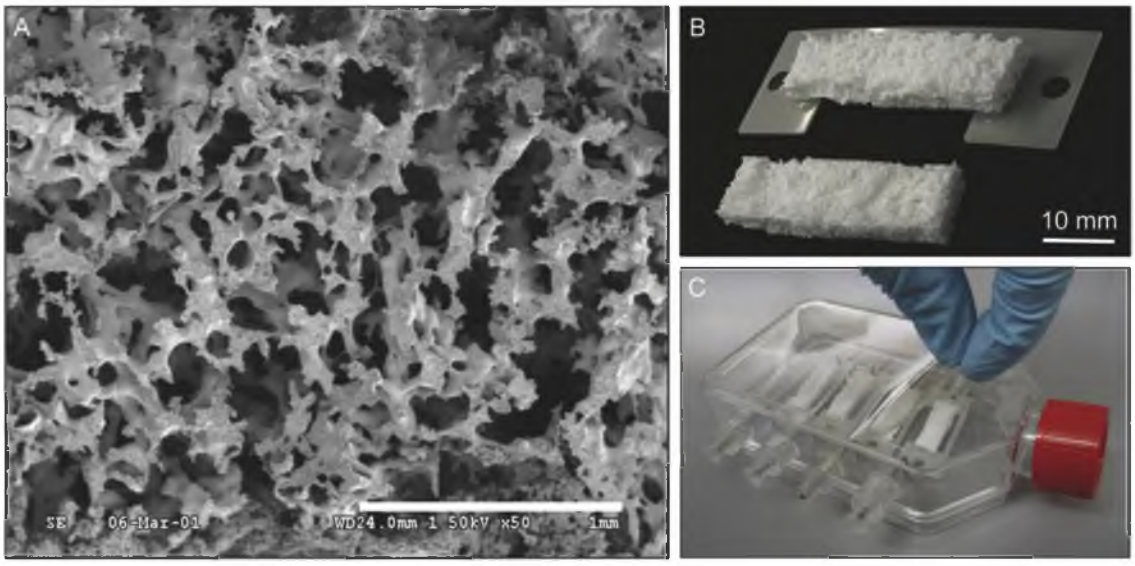

Figure 5-1: (A) SEM Image of porous culture substrates fabricated from medical grade polyurethane. The substrates are soft, elastic, open-celled foams with a 70% void volume. (B) The substrates were formed into strips (30mm x 10mm x 2mm) and attached to Mylar mounts using a UV curable adhesive and (C) mounted into custom modified T-flasks, and cultured for three weeks.

5.2.3 Cell-derived material extraction

Following culture, samples were rinsed in DI H_2O and frozen to -80°C. PU removal was performed as described previously with samples being weighed and then soaked in the solvent DMAC for 72hrs [212]. We exchanged the solvent seven times during the 72hr period, three times on the first day and then twice daily thereafter. An overview of the cell-derived material extraction process is shown in Figure 5-2.

5.2.4 Characterization of extracted material

Following PU removal, the remaining material was rinsed seven times in DI H_2O, frozen, and then lyophilized. We calculated the yield of cell-derived material relative to the initial weight of the PU substrate (n=10 samples/cell type). To characterize the material's bulk architecture, we imaged lyophilized samples using a dissection microscope and a Coolsnap digital camera.

We assessed the effectiveness of PU foam removal using Fourier transform infrared spectroscopy (FTIR). IR spectra were obtained in attenuated total reflection mode (Bio-Rad). PU and cell derived material samples were analyzed in the 900 to 1800cm^{-1} range with a resolution of one cm^{-1}. To verify removal of the PU from cell-derived samples, we examined the FTIR spectra for the presence of urethane and amine absorbance peaks.

To identify extracellular matrix components present in the extracted materials, astrocyte and GRP-derived material samples were processed using indirect immunocytochemistry for fibronectin (CFN 1:500; Sigma), laminin (LN

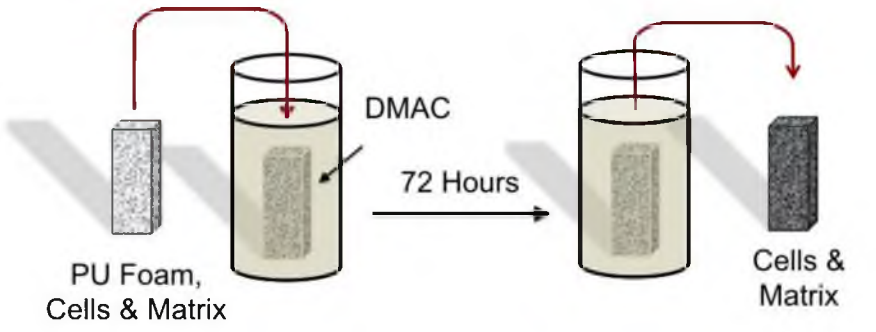

Figure 5-2: Schematic overview of the ECM extraction process. PU foams cultured for three weeks with either astrocytes or GRPs are exposed to the hydrophilic, aprotic solvent DMAC. Following solvent treatment to remove the PU foam we are able to harvest a synthetic free cell-derived material composed of the cultured cells and their ECM.

antibodies in a detergent-free blocking solution consisting of 4% (v/v) goat serum (Invitrogen, Carlsbad CA) and 0.1% (w/v) sodium azide in PBS. Free-floating material samples were batch treated for 1hr in a detergent-free, blocking solution at room temperature, followed by incubation with primary antibodies overnight at 4°C. After three washes in PBS to remove excess antibodies (1hr/rinse), appropriate fluorescently labeled secondary antibodies (Molecular Probes) were applied in block for 1hr at room temperature, followed by three washes in PBS (1hr/rinse). Fluorescent images were captured with a Coolsnap digital camera and a Nikon Eclipse E600 microscope.

We analyzed a representative sample of each type of material with tandem mass spectroscopy (MS/MS), as described previously to more broadly determine their proteomic compositions. The cell derived material sample was washed with 50mM ammonium bicarbonate, denatured (Protease Max, Promega, Madison, WI) for 30mins at room temperature, trypsin (20ng/µl) digested overnight at 37°C, and purified (Ziptip, Milipore, Billerica, MA). The MS/MS

analysis was performed at the University of Utah proteomic core facility using a hybrid mass spectrometer (LTQ-FT, Thermo Scientific, Waltham, MA). Primary peptide molecular mass spectra were acquired by Fourier transform ion cyclotron resonance. The sequencing of individual peptide spectra was performed by collision-induced dissociation in the linear ion trap. Sample proteins were identified by comparison of MS/MS measured peptide sequences to a trypsin-cut specific protein database (Mascot ver. 2.2.1, Matrix Science Inc., Boston, MA).

5.2.5 Cytotoxicity and in vitro compatibility studies

Prior to seeding samples with either primary rat dorsal root ganglion cells (DRGs) or primary P2 rat microglia, we first decellularized the samples as described previously. In brief, cell-derived material samples were placed in hypotonic Tris-Hcl buffer (10 mM, pH 8.0) with 0.1% EDTA and 10 KIU/ml aprotinin (Sigma) for 1-2hrs at room temperature (R.T.) to disrupt integrin-ECM interactions and deactivate proteases that were released due to cell lysis. To remove lipids, we then immersed samples in Tris-Hcl buffer containing 0.1% SDS (10mM, pH 8.0) on a rocker at 100 rpm at R.T. overnight. Following lipid removal, we rinsed the samples three times, 30mins each, in PBS on a rocker. Lastly, to remove nuclear material, we treated samples with Tri-Hcl buffer (50 mM, pH 7.5) containing ribonuclease (1 U/ml, Sigma) and deoxyribonuclease (50 U/ml, Sigma) on a rocker at 37°C for 3hrs. Following nuclear material digestion, we again rinsed samples with three, 30min, PBS washes on a rocker. To assess the effectiveness of our decellularization process, we treated the control and decellularized material with the nucleic acid stain DAPI.

Following decellularization, we seeded primary rat DRGs or primary P2 rat microglia on control glass coverslips or decellularized astrocyte and GRP-derived material samples at a density of 50k cells/cm^2 (DRGs) or 100k cells/cm^2 (microglia) in DMEM/F12 + 10% FBS. We treated six of the 12 samples for neurite outgrowth studies with chondroitinase ABC (ChABC, 0.1 unit/ml in tris acetate buffer) for 4hrs at 37°C prior to seeding. We assessed neuronal viability and outgrowth with Calcein AM and indirect immunohistochemistry for NeuroFilament 160 (NF 160) respectively. Microglia morphology was assessed with indirect immunohistochemistry for Iba-1 and CD-68 using similar protocols as described above with the addition of 0.5% Triton X-100 to blocking and anti-body solutions to expose the intracellular antigens. We morphologically classified microglia as either ramified or amoeboid as described previously [207].

5.2.6 Cell-derived biomaterial coatings for Si microelectrode arrays

300μm-wide planar lattice microelectrode arrays were supplied by the Center for Wireless Integrated Microsystems at the University of Michigan. To covalently tether harvested cell-derived material to SiO_2 electrode surface, we first functionalized the surface with an epoxy silane, glycidoxypropyl-trimethoxy silane (GPS), via chemical vapor deposition under vacuum at 110°C in an N2 atmosphere [187, 188]. Following epoxy-functionalization, electrodes were exposed to astrocyte or GRP-derived material suspensions overnight. Following covalent coupling of the cell-derived material to the electrode surface, we sequentially exposed devices to a 2% (w/v) $CaCl_2/H_2O$ solution and then a cell-

derived material suspension. To test the robustness of the coating we implanted coated devices into an agar gel followed by immediate explantation.

5.2.7 Preparation of injectable, cell-derived biomaterials

Decellularized, cryo-ground astrocyte or GRP-derived material was solubilized over 48hrs in a 0.1N HCl/pepsin solution. Following solubilization, we brought the digested cell-derived material to pH 7.4 with addition of a 0.1N NaOH/PBS solution. Finally, we induced gelation by bringing the pH-balanced solution back to body temperature (37°C) [204].

5.3 Results

5.3.1 Characterization of extracted material

Similar to material derived from other cell types using similar harvesting methods, the isolated material from both astrocytes and GRPs was white, lacey and porous (Figure 5-3). The derived material had a shape and microstructure similar to the arrangement of the pores and cavities of the original sacrificial open-cell foam. Following a three-week culture period, astrocyte and GRP samples yielded 18±1.3 and 44±14mg of extracted material per gram of seeded foam, respectively (Figure 5-3).

PU foam FTIR spectra contained two distinct peaks centered at 1700 cm^{-1} and 1100 cm^{-1} that is characteristic of the C-O-C stretching found within urethane bonds. We did not observe these characteristic urethane linkage peaks within the FTIR spectra of the cell-derived constructs after DMAC treatment. However, similar to the FTIR spectra of tissue [216, 217], the spectra of cell-derived

constructs contained several distinct peaks corresponding to primary, secondary, and tertiary amines (Figure 5-4). We did not observe these amine peaks within the FTIR spectra of control PU foams.

To identify ECM components present in the extracted materials, astrocyte and GRP-derived material samples were processed using indirect immunocytochemistry for various ECM components found in the CNS. The cell-derived material was immunoreactive to antibodies against fibronectin, laminin and chondroitin sulfate gycosoaminoglycans (CS GAGs). Representative fluorescent images of these ECM components found in astrocyte and GRP-derived material are shown in Figure 5-5.

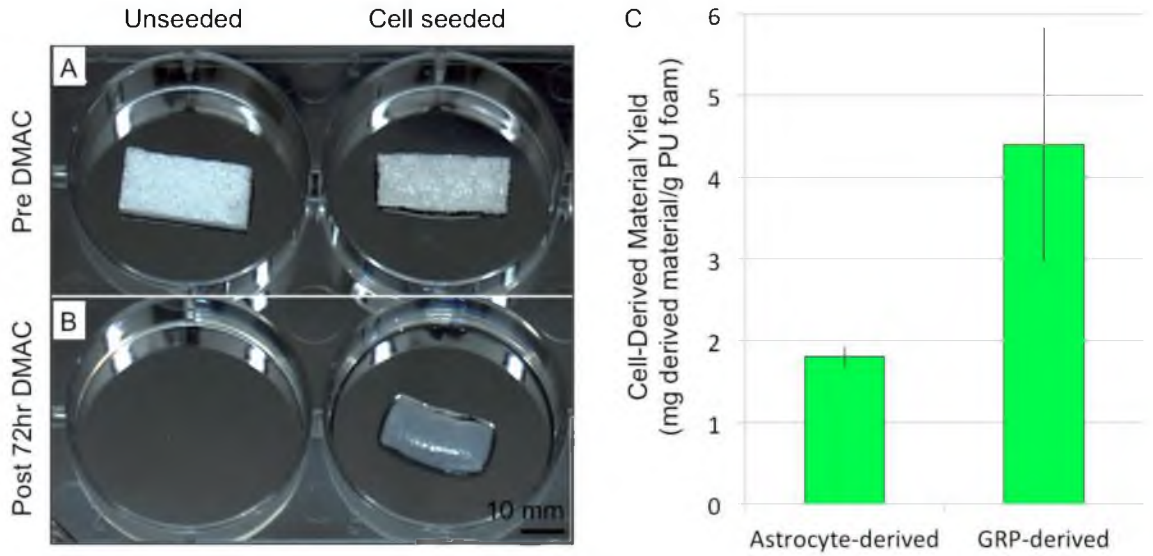

Figure 5-3: (A and B) Representative images from pre- and post-DMAC treatment of unseeded and cell-seeded constructs. Cell-free control foams were completely dissolved (B-left well), however, substantial material remained following DMAC treatment of cell-seeded samples (B-right well). (C) Astrocyte and GRP seeded samples yielded approx. 1.8 and 4.4mg of material for every substrate, respectively.

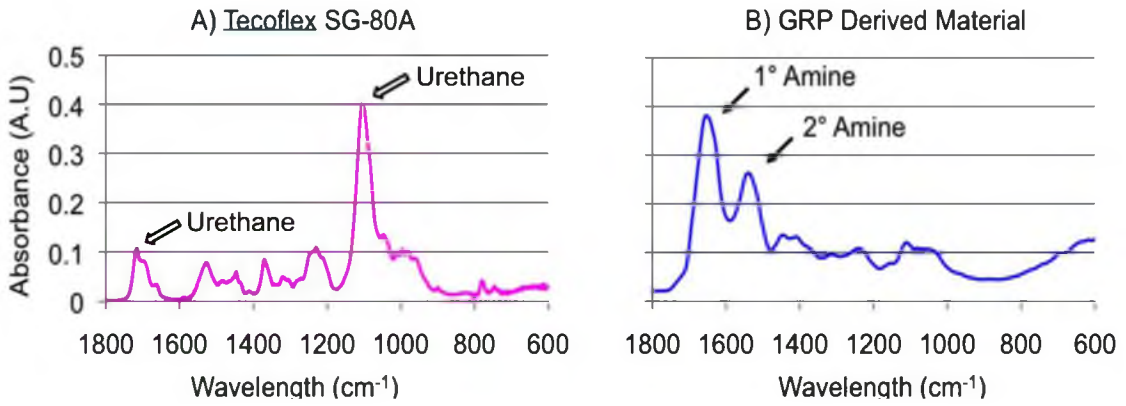

Figure 5-4: Representative FITR-ATR spectra of A) Tecoflex SG-80A PU and B) GRP cell derived biomaterial. We did not observe strong characteristic polyurethane linkage peaks (open arrows in A) within the FTIR spectra of cell-derived biomaterials. However, we did observe increased absorption corresponding to amine chemistries in the cell-derived biomaterials (solid arrows in B).

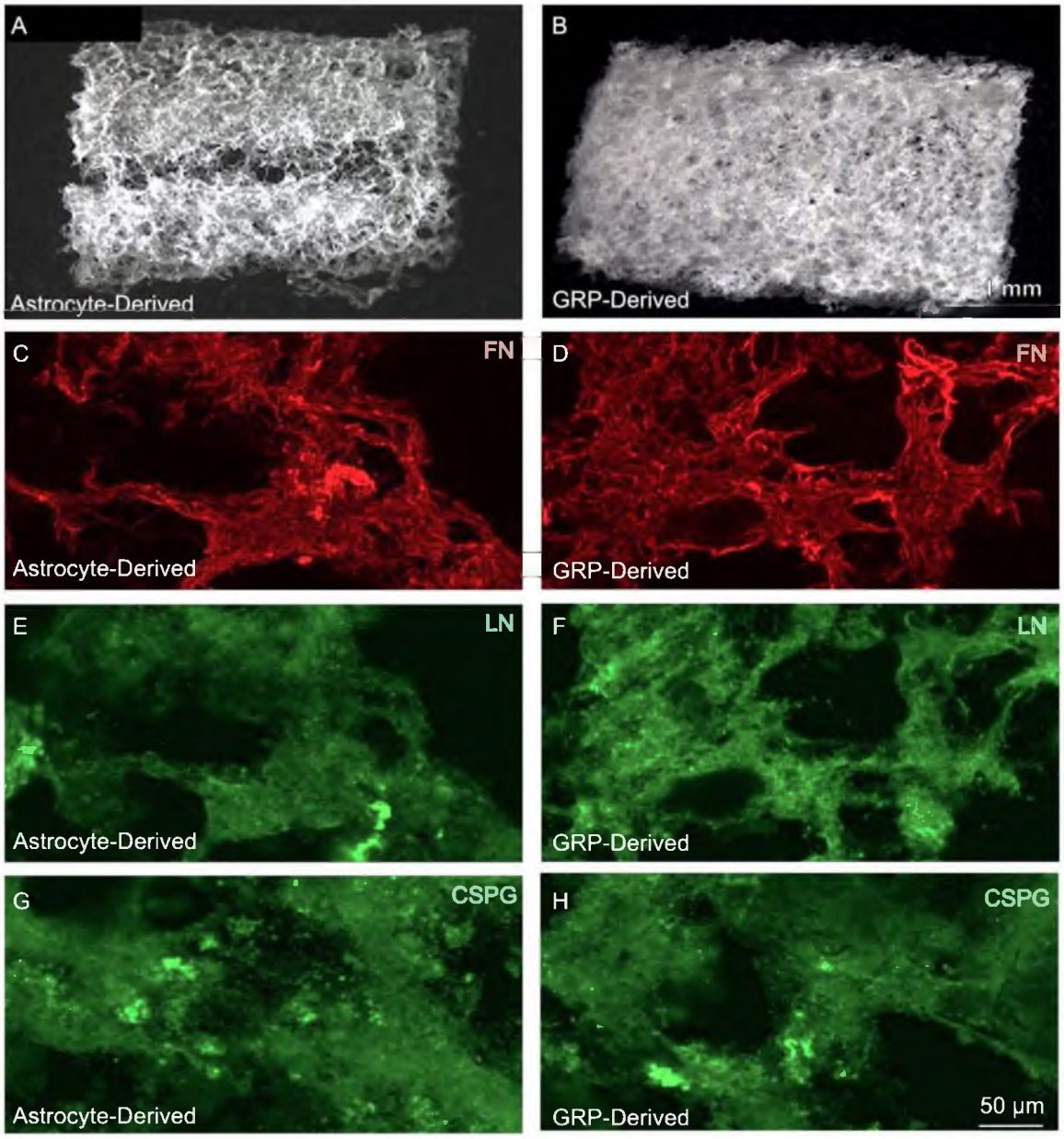

Figure 5-5: (A and B) Representative light micrographs of astrocyte and GRP-derived biomaterials after dissolution of the culture substrate. Isolated material from both cell types was white, lacy and porous. Panels (C,E,G) and (D,F,H) show confocal images of astrocyte and GRP derived material stained for FN, LN and CSPG respectively.

To examine the effectiveness of our decellularization protocol, we examined the cell-derived materials for the presence of nuclear material and cytoskeletal components such as GFAP and actin. Following decellularization we observed no cell nuclei or cytoskeletal components within the astrocyte or GRP-derived materials indicating the successfulness of our protocols. Furthermore, all ECM components investigated with immunohistochemistry as described above remained following decellularization.

5.3.2 In vitro compatibility of cell-derived materials

Cytocompatibilty studies showed the cell-derived material to be nontoxic and adhesive to further cell culture with primary CNS cells. Figure 5-6 shows representative Calcien AM viability staining of P1 rat primary DRGs cultivated for 48hrs on cell-derived biomaterials. Furthermore, using NF160 staining of P1 rat primary DRGs cultivated on non-ChABC treated or ChABC treated samples, we observed that digestion of chondroitin sulfate improved neurite outgrowth compared to outgrowth on control samples.

To categorize the activation state of microglia cultured on our cell-derived material, we used immunohistochemistry against Iba-1. Figure 5-7 shows representative microglial morphology cultured on glass, astrocyte-derived or GRP-derived biomaterials. Similar to studies examining microglial morphology on fixed astrocyte monolayers, a significant number of microglia cultured on our cell-derived biomaterials showed a more ramified, resting phenotype than those cultured on glass, even in the presence of serum [207].

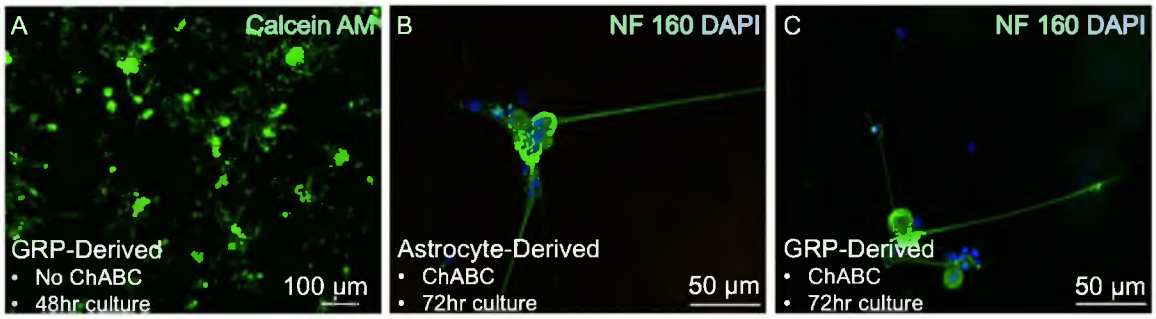

Figure 5-6: Cytocompatibilty studies showed the cell derived material to be nontoxic and adhesive to further cell culture. (A) Representative Calcien AM viability staining of P1 rat primary DRGs cultivated for 48hrs on GRP-derived biomaterial that was not treated with ChABC. Under these conditions living cells were well distributed throughout the material and sent out short, unbranched bipolar neurites. (B and C) Representative NF 160 staining of P1 rat primary DRGs cultivated for 72hrs on ChABC treated samples. ChABC treatment qualitatively improved neurite outgrowth compared to those on non-ChABC treated samples.

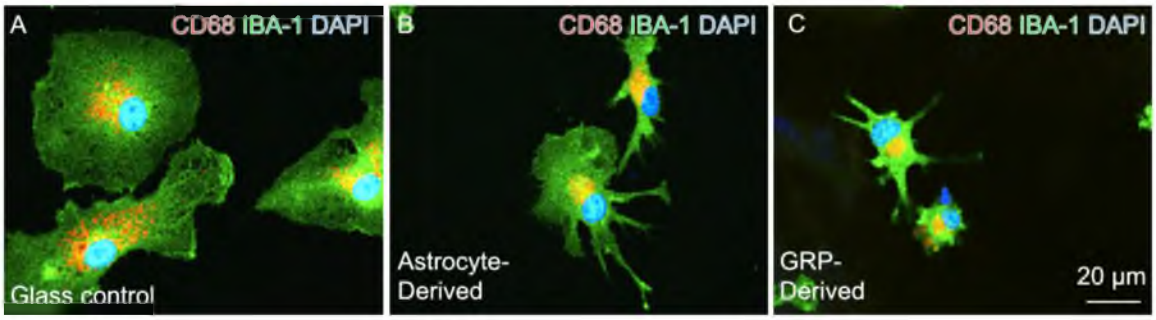

Figure 5-7: Representative microglial morphology cultured on (A) glass, (B) astrocyte-derived biomaterial and (C) GRP-derived biomaterial. Cells were stained with antisera against CD-68 (a lysosomal enzyme found in mononuclear phagocytes), Iba-1 (a calcium binding molecule expressed in all macrophages and microglia) to visualize cell morphology, and counterstained with DAPI to label cell nuclei. (D) Similar to studies examining microglial morphology on fixed astrocyte monolayers, a significant number of microglia cultured on our cell-derived biomaterials showed a more ramified, resting phenotype than those on glass, even in the presence of serum.

5.3.3 Astrocyte and GRP-derived ECM coatings for microelectrodes

We investigated whether we could use the cell-derived material as a coating for biomedical devices such as silicon microelectrode arrays with the end goal of improving their integration into CNS tissue. To accomplish this we covalently coupled the cell-derived material to the device's SiO_2 surface using the epoxy silane GPS. Figure 5-8 shows a representative 300μm wide silicon microelectrode array coated with our derived material. The resulting coating was robust enough to withstand implantation into an agar gel suggesting that the coatings can withstand surgical implantation into the CNS.

5.3.4 Other potential applications

The harvested astrocyte and GRP-derived material sheets were mechanically resilient and could be easily handled with hand-held forceps when lyophilized. Furthermore, upon rehydration when placed in contact with tissue, the material adhered well without the need for suturing suggesting that the constructs could be applied surgically as a regenerative scaffold or graft.

Lastly, we also investigated the potential of delivering the harvested cell-derived material in a solubilized form that is capable of spontaneous gelation under physiological conditions. Similar to methods used to create gels from collagen and other types of ECM, we found that we could digest the harvested ECM using a pepsin digest at low pH and induce gelation upon raising the pH, ionic concentrations and temperature to physiological conditions [204]. Figure 5-8 shows the solubilized ECM prior to and following gelation. This minimally

invasive delivery form has vast potential as an alternative method for device coating as well as a cavity-filling agent or an injectable cell delivery vehicle for treatment of conditions ranging from traumatic brain and spinal cord injury (TBI & SCI) to stroke or Parkinson's disease.

5.4 Discussion

The foremost limitation to the clinical implementation of microelectrode recording devices for use in brain machine interfaces is their failure to achieve high-quality recordings over clinically relevant time frames. The poor recording longevity of microelectrodes is widely believed to be due to poor wound healing

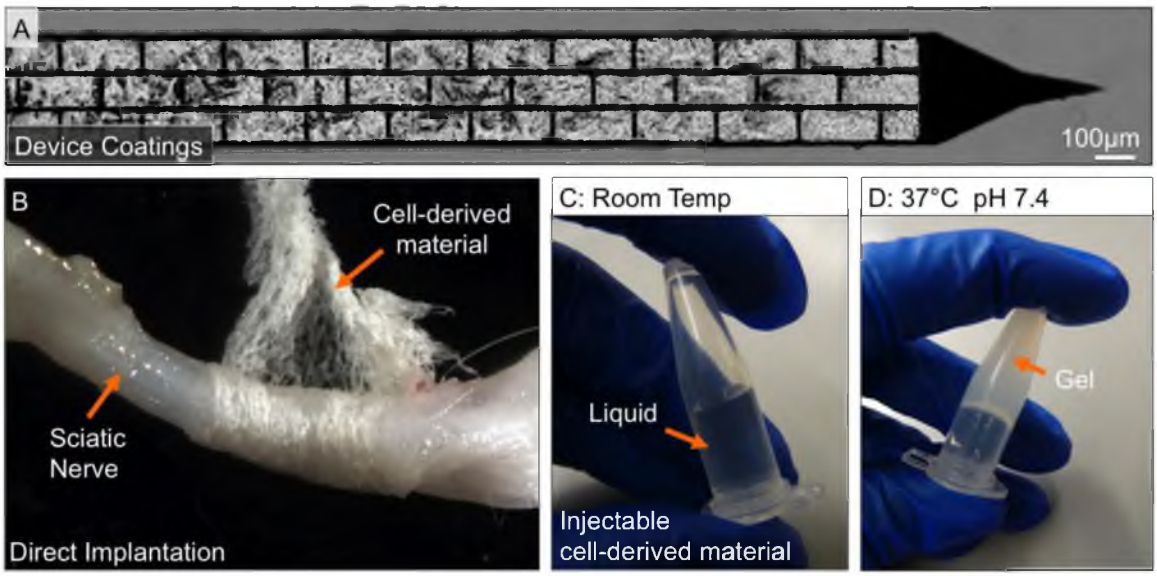

Figure 5-8: Cell-derived biomaterials can be prepared in various therapeutic formulations including (A) coatings of microelectrode arrays and other medical devices, (B) 'as prepared' decellularized sheets used in this case as a novel nerve cuff as well as (C & D) injectable solutions that gel at biological pH and 37°C for use as injectable scaffold or hemostat or as a cell delivery vehicle.

and the chronic FBR surrounding the synthetic materials currently used for recording microelectrodes. In this study we have taken a regenerative medicine approach to reduce the FBR to microelectrode arrays by developing both approaches to harvest ECM produced by CNS cells, including immature astrocytes and glial restricted precursors (GRPs), and techniques to covalently immobilize and coat these materials onto silicon microelectrodes. Similar cell-derived biomaterials have previously been shown to exhibit superior biocompatibility and facilitate improved healing compared to synthetics in regenerative medicine applications [193, 194].

Our harvesting technique improves upon these traditional regenerative medicine approaches and other cell-derived products. Aside from donated human tissues and organs, to date the majority of cell-derived products that have been developed come from animal, primarily bovine and porcine, sources. These products range from simple grafts and powders to decellularized whole animal organs that maintain the complex structure needed for proper organ function. While the majority of proteins and GAGs found in the ECM are well conserved between animals and humans, interspecies differences do exist. As a result, although less vigorous than the response to similar cellularized materials, published studies indicate that chronic inflammation and graft rejection mediated by an adaptive immune response can occur with cross species implantation of even acellular ECM [195-197]. Therefore, while the implantation of readily available ECM from xenogeneic sources has clear value, the development of

approaches for producing autologous or allogeneic materials may prove key for improving the clinical success of these products [198].

We have previously found that our method is not only compatible with various cell types, but also with cells from various species [212]. Thus, our method permits the creation of materials that are species-matched to the intended host, be it rat, rabbit, or human. Previous studies have found that allogeneic human ECM proteins are well tolerated by the host and do not appear to elicit either a cell mediated or humoral immune response [197, 198]. Therefore, allogeneic ECM materials harvested using our method may offer therapeutic advantages above and beyond xenogeneic ECM materials. Alternatively, a patient's own biopsied cells could also be used to create autograft material using our method, however, the production of an autograft material would require preoperative cell harvest followed by a moderate cultivation period indicating the use of autograft material to clinical applications where time is not a critical factor.

Another limitation of a number of current cell-derived products is that they are not derived from the same type of tissue as that in which they are to be used. Although ECM from different tissues share common constituents, growing evidence suggests that subtle differences in ECM composition may influence the regenerative outcomes for specific tissues. A number of studies have shown that culturing cells on tissue-specific ECM improves infiltrating cell proliferation rates and increases expression of desired phenotypic cell and tissue characteristics [200-204]. In contrast, other studies have shown that implantation of nontissue

specific ECM materials induces the formation of undesired, phenotypically irregular tissue at the implantation site [205, 206].

Our method allows for harvesting of tissue-specific matrix produced by any type of adherent cell seeded onto the original sacrificial foam substrate. In this study, with the goal of incorporating regenerative and antinflammatory properties found in ECM to microelectrode arrays that are implanted in the CNS, we have chosen to investigate the matrix harvested from astrocytes, the primary support cell in the CNS, as well as GRPs, an immature progenitor that can develop into astrocytes or oligodendrocytes. Importantly, these cells and particularly their produced matrix have been shown to play a number of important roles in the developing and adult CNS. In particular, it has been shown that the ECM produced by astrocytes may be involved in neuronal guidance during development as well as the regulation of the activation state of resident microglial cells in the adult CNS [207]. Additionally, the transplantation of immature GRPs into the lesion site has been shown to facilitate regeneration following SCI [208, 209].

One obvious tissue-specific role that these materials must be able to perform in a CNS regeneration application is to support neuronal growth. Not surprisingly, our in vitro assays verified that both types of cell-derived biomaterials were nontoxic and promoted neurite outgrowth in primary neurons. In addition, similar to regeneration following SCI, improved outgrowth was observed following digestion of chondroitin sulfate glycosaminoglycans (CS GAGs) [218]. These GAGs have historically been considered to be neuroinhibitory [219-225], however,

recent studies have shown that certain isoforms of CS actually facilitate neuronal outgrowth [226, 227]. Further studies that remove and modify only certain isoforms of CS using xylosides or other strategies may improve our materials further [228-233].

Another important tissue-specific role of the astrocyte is to assist in regulating the activation state of microglial cells, the resident macrophage of the CNS. While astrocytes are known to secrete a number of soluble factors that assist in microglial regulation, studies have shown that their secreted ECM also plays an intricate role. For example, Tanaka et al. showed that microglia cultured on fixed astrocyte monolayers, even in the presence of serum (a potent inflammogen), displayed a resting phenotype, indicating that cues presented by the astrocyte ECM are sufficient to regulate these potent inflammatory cells [207]. Additionally, these intact fixed ECMs showed a greater ability to induce this resting, ramified phenotype compared to single isolated ECM components such as the proteoglycan LN, which has previously been used as a microelectrode coating [164]. These findings indicate that multiple ECM components found in the astrocyte ECM help to regulate macrophage activation and that developing coatings that mimic this complexity could further improve the FBR to microelectrode arrays.

Excitingly, material harvested from both types of cells that was dried onto glass coverslips (a similar substrate to that used in planar MI arrays as well as UEAs) also demonstrated the ability to down regulate microglial activation. This finding further indicates that the bioactivity of the ECM was maintained following

solvent exposure and subsequent processing steps. Additionally, this finding indicates another way in which our materials could improve CNS regeneration as well as opening up possible applications as coatings to reduce the FBR to traditional biomedical devices.

A limited number of alternative methods have been developed in our lab and others that can also create synthetic-free, nonxenogeneic, tissue matched ECM. One such approach is the fabrication of engineered multilayered cell sheets from planar surfaces [234-237]. The use of these materials has been directed towards the repair of cardiac, corneal, peripheral nerve and spinal cord tissues. However, we have observed that these methods produce limited amounts of ECM indicating that they may not be as well suited for large-scale development as the ECM harvesting technique described in this study.

The increased accumulation of ECM in our open celled foams may be explained by the increased surface to volume ratio of our foams compared to the planar substrates used in cell sheet engineering. The increased surface area may make available additional surfaces on which cells can accumulate and produce ECM. It is important to note that the accumulation of ECM within porous foams may also be the consequence of a molecular crowding phenomenon [238, 239]. On planar tissue culture surfaces much of the secreted ECM diffuses away and is subsequently eliminated while exchanging the culture media. The tortuous architecture of the substrate likely facilitates this molecular crowding by reducing diffusive dispersion and subsequent loss of ECM. This suggests that foam design

may be further optimized to accelerate ECM accumulation by developing new foam structures.

The approach introduced here is not limited to the open cell, PU foams as described herein. A wide range of thermoplastics whose structure consists of amorphous chain entanglements that can be overcome with polar aprotic solvents should make successful sacrificial scaffolds. Most hydrolytically degradable polymers could be used as well, as long as they have sufficiently short degradation times. For example, work by Lu et al. describes the use of PLGA in a similar method for harvesting ECM from human mesenchymal stem cells, articular chondrocytes and dermal fibroblasts [240]. Additionally, the fabrication techniques for the sacrificial substrate need not be limited to those produced by phase inversion. Other techniques that could be employed include, but are not limited to, gas foaming, particle leaching, hollow fiber extrusion and electrospinning [241-244].

5.5 Conclusion

In this study we have investigated novel methods to adapt regenerative medicine approaches for use in improving the integration of recording microelectrodes implanted in the CNS and limiting the FBR that occurs with chronic device implantation. To do this we have developed a simple method to harvest synthetic-free ECM material from astrocyte and GRP cells cultured within sacrificial polymer substrates. This approach represents a new method to create autologous and allogeneic cell-derived biomaterials for a variety of applications. In vitro cytocompatibility studies showed the material to be nontoxic and

adhesive to various CNS cell types. Furthermore, in vitro assays indicated that these cell-derived biomaterials may improve neural regeneration or device integration by promoting neurite outgrowth of primary neurons and by down regulating the activation state of inflammatory microglia. Studies in progress are examining the usefulness of these materials in a wide range of regenerative medicine and neural engineering applications.

CHAPTER 6

SUMMARY, CONCLUSION AND FUTURE WORK

6.1 Summary of presented work

There is near consensus in the field that the foreign body response (FBR) to implanted microelectrodes contributes to recording inconsistency and may limit the functional lifetime of these devices. Available evidence suggests that soluble factors secreted by activated macrophages and/or microglia at the device-tissue interface mediate the cellular-level changes underlying the FBR. To explore this hypothesis and identify strategies that engineers can utilize to improve next generation devices, we have taken a comprehensive approach by first investigating implant designs that passively reduce the impact of these cells and their released soluble factors and secondly creating bioactive coatings to promote regeneration and down regulate inflammation in the surrounding tissue.

To facilitate the design and testing of our passive strategies for reducing the FBR, in Chapter 2 we developed a computational model to predict the steady-state distribution of macrophage-released soluble factors surrounding traditional and novel device designs. Due to the difficulty of analyzing the spatial distribution of macrophage-released factors in tissue, we validated the usefulness of our models using indirect methods such as comparing the predicted soluble factor

distributions to the structure and spatial distribution of well documented, downstream responses associated with the FBR to traditional electrode designs. Our predicted distributions align well with the shape and structure of the FBR to traditional, commercially available microelectrodes including planar MI-style microelectrodes, cylindrical microwires and more complex devices like the Utah Electrode Array (UEA). Based on our underlying hypothesis that macrophage released soluble factors drive other aspects of the FBR, the observed alignment between our predictions and FBR hallmarks indicates that our model is in fact useful for predicting the FBR to devices implanted in the CNS.

Expanding on our models, we virtually tested whether manipulation of a number of design parameters could reduce the FBR. Two of the most useful design changes indicated by our predictions include (1) reducing device surface area to limit the number of macrophages at the device tissue interface (and thus the concentration of their secreted pro-inflammatory factors) as well as (2) incorporating cytokine sinks to passively absorb pro-inflammatory factors into the device and away from adjacent brain tissue.

To further validate the usefulness of our model and to investigate whether reducing device surface area lowers the brain FBR, in Chapter 3 we studied the brain tissue reaction to planar silicon microelectrode arrays with identical penetrating profiles but different amounts of exposed surface implanted in rat brain for eight weeks. We found that altering the exposed surface area of an implanted microelectrode array while maintaining a similar penetrating profile is sufficient to significantly change the classic hallmarks of the chronic FBR

including reducing the degree of inflammation, blood brain barrier leakiness and the amount of neuronal cell body loss.

Once again, building on the predictions from our models and the reduced FBR to semipermeable hollow fiber membranes (HFMs), in Chapter 4 we studied the chronic brain tissue response to planar solid silicon microelectrode arrays with thick hydrogel coatings (cytokine permeability sinks) designed to passively absorb pro-inflammatory factors that are released by reactive immune cells into the device and away from adjacent brain tissue. When compared to the response surrounding uncoated cohorts as well as arrays with a thin nanoscale hydrogel coating, serving as a surface chemistry and functional sink control, we observed a reduced degree of inflammation, improved blood brain barrier integrity, diminished astrocyte hypertrophy and reduced neuronal cell body loss.

Taken together the findings from these two in vivo studies show that it is possible for electrode developers to modulate specific aspects of the brain tissue FBR by intentionally manipulating device design. Additionally, these findings further validate the usefulness of our predictive model to drive future device designs that integrate into the body and avoid the FBR. On a broader level, these results support our theory that the FBR to implanted electrode arrays, and likely other devices, can be explained by the persistence of activated macrophages at the biotic-abiotic interface, which act as a sustained delivery source of bioactive agents that diffuse into the adjacent tissue and shape other features of the FBR.

Beyond these passive design strategies we also explored the possibility of adapting regenerative medicine approaches to improve the FBR to implanted

devices by creating bioactive coatings that may promote regeneration and may down regulate inflammation at the device interface. To do this we developed a simple method to harvest synthetic-free ECM material from astrocyte and GRP cells cultured within sacrificial polymer substrates. This approach represents a new method to create autologous and allogeneic cell-derived biomaterials for a variety of applications. In vitro cytocompatibility studies showed the material to be nontoxic and adhesive to various CNS cell types. Furthermore, in vitro assays indicated that these cell-derived biomaterials may improve neural regeneration or device integration by promoting neurite outgrowth of primary neurons and by down regulating the activation state of inflammatory microglia.

6.2. Future work

As described previously in this work, a number of other strategies have been investigated to reduce the FBR to microelectrodes; however, using traditional materials and device designs, isolating the impact of each of these strategies is difficult at best. For example, another major strategy in the field for reducing the FBR is the creation of soft polymer-based microelectrodes that better match the mechanical properties of the surrounding tissue. It is believed that this improved mechanical matching will limit repetitive, micromotion-induced damage at the biotic/abiotic interface, thus reducing a potential mechanism for propagation of the FBR.

While we believe that the reduced FBR achieved via either of our passive design strategies is primarily due to a reduction of activated macrophages and their released factors (discussed in Chapters 2-4), our findings are confounded to

some degree by the difference in mechanical properties of the implanted cohorts. Conversely, many of the polymers used to create flexible, soft electrodes absorb a significant degree of water and are likely permeable to small molecules, adding the possibility that the findings in these studies have been influenced by improved clearance of macrophage secreted factors. Due to the potential that well established strategies for reducing the FBR could have, not only on recording microelectrodes, but also on all chronically implanted devices, studies aimed at characterizing the response field for the FBR to a variety of potential explanatory design variables are needed.

Central to this set of studies are novel test devices that isolate individual design elements; facilitating the examination of the ranges where specific property changes modulate the FBR. Additionally, these devices should allow for a number of explanatory variables to be manipulated in conjunction so that interactions between variables such as stiffness, permeability, roughness, surface chemistry, severity of iatrogenic injury, and architecture can also be investigated once the most promising explanatory variables are determined. One possibility for this type of device is shown in Figure 6-1. This design is based on elements from hollow fiber membrane (HFM) technology as well as planar MI-technology and allows for the examination of interaction between stiffness, permeability and roughness while controlling for differences in the severity of iatrogenic injury and surface chemistry.

Though our findings from the in vivo studies described in Chapters 2 and 3 help to validate our model's predictions as well as our underlying hypothesis that

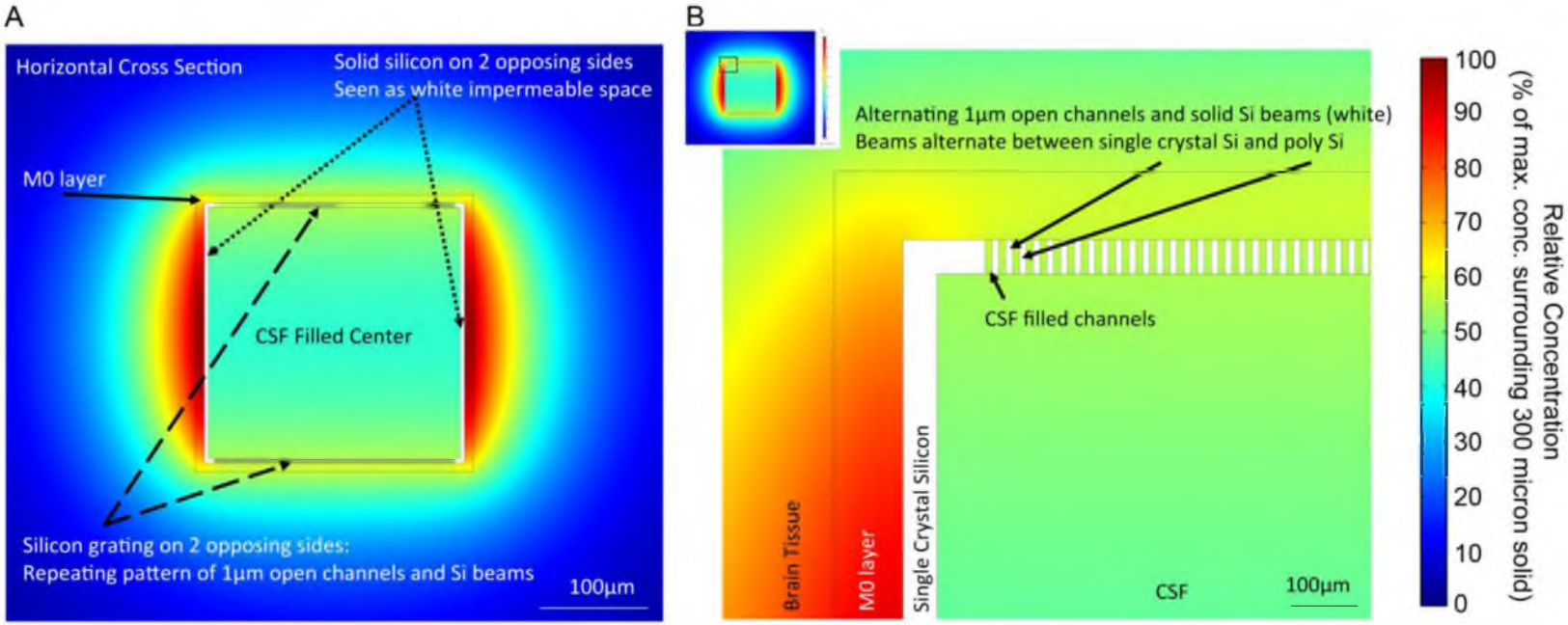

Figure 6-1: (A) Cross section of a novel test device to allow for the examination of the impact of both device mechanics and permeability on the FBR. (B) Expanded view of cross section in (A) showing the semipermeable wall structure of the top and bottom walls shown in (A) created using similar methods to those used by Lopez et al. [190, 191]. By making the structure from both silicon as well as adapting methods used by Seymor and Kipke [136] to make the device from soft polymers, both mechanics and permeability can be tested in designs that create similar penetrating injuries. Controlling wall thickness as well as the number and size of the grating channels permits tailoring the wall structures permeability.

macrophage-secreted factors are the primary drivers of the FBR, additional work remains to be done to validate our predictions and to verify the mechanism or mechanisms underlying these reductions. One key aspect of this future work is to better validate our model by measuring in vivo cytokine profile surrounding implanted devices and to refine our model parameters based on these findings. We have investigated a number of methods to measure and profile cytokine distribution in tissue, including immunohistochemically labeling cytokines of interest as well as detecting cytokine mass fragments using imaging MALDI mass spectroscopy. Once more fully established, these methods for profiling cytokine distributions in tissue will provide information not only to validate our diffusion models but will be extremely useful in other areas, such as the study of neuroinflammatory conditions like MS and Alzheimer's disease that share many commonalities with the inflammatory response surrounding implanted devices.

There are a number of other methods that could provide supplemental information regarding the role of macrophages and their released soluble factors in the FBR including laser capture microdissection (LCμD) in conjunction with quantitative PCR. LCμD enables the isolation of single labeled cells or populations of cells from a tissue section or in vitro culture (i.e. activated macrophages at the biotic-abiotic interface). Following isolation both gene expression and protein translation can be detected using quantitative PCR and SELDI-TOF mass spectroscopy as a means to further characterize the initial creation of soluble factors within inflammatory cells. While not a direct method toprofile soluble factor distribution in vivo, this method will add to the mounting

evidence that macrophages at the device interface chronically produce inflammatory and cytotoxic factors that could play a primary role in the FBR to implanted devices.

Another macrophage/microglia area of research that needs further investigation and development deals with the physiology, basic functions and activation states of cells surrounding implanted devices. To date we are one of the few groups who use a marker specific for activated macrophages (the lysosomal enzyme CD-68) in place of, or in combination with pan-macrophage markers (IBA-1 or OX-42) to describe the FBR. However, an expanding field of literature has shown that the activation state of these cells is even more detailed and complex than can be observed with just CD-68. This range of activation states is commonly broken down into three categories: resting resident macrophages (M0) that are in a constant state of surveying their surroundings for possible stimuli such as pathogens or tissue damage, classically activated inflammatory macrophages (M1) that release a variety of proinflammatory cytokines and effector molecules, and prohealing macrophages (M2) that release a variety of growth factors to induce regeneration and tissue growth [123]. Further characterization of macrophages surrounding implanted devices using the evolving macrophage classification schemes will further help us to understand their role in various stages of the FBR and may better elucidate specific mechanisms that influence device performance as well as intervention strategies.

Information regarding the state of macrophages/microglia at the implant interface would also be useful when analyzing our astrocyte and GRP ECM coatings. To date we have shown that these materials induce a ramified phenotype in microglia even in the presence of known inflamogens such as serum. This morphology change has traditionally been classified as an indicator of down regulated macrophage activity [207, 245]. However, implementing a more detailed analysis into macrophage activation could help us determine if these cells have merely been coaxed back into a resting M0 phenotype or if they may actually have led these cells to a prohealing M2 phenotype.

In addition to the local impact of inflammation and the FBR, there is also growing evidence that these responses impact vulnerable tissues and cell processes at considerable distance from the implant site. In, as of yet, unpublished work from our lab we have observed that chronic electrode implantation, even solely in the cortex, is accompanied by decreased neurogenesis in the subventricular zone of the dentate gyrus (DG). This zone has been shown to play a key role in learning and memory. Similar to our findings regarding BBB dysfunction, decreases in neurogenesis have been observed in neuroinflammatory diseases such as Alzheimer's disease. In these conditions it is widely believed that these phenomena are caused by activated macrophages/microglia and their released soluble factors.

Though we have shown that device implantation impacts neurogenesis, and other groups have shown that inflammation in various disease states associated with various implanted devices correlates with cognitive dysfunction,

further work needs to be done to more fully determine device related inflammation's impact on end cognitive deficits, which would be of primary clinical concern. One method to bridge this gap would be the use of the novel object recognition tests in conjunction with device implantation. In these types of tests cognitive function is measured based on the difference in the amount of time an animal spends exploring a novel object compared to a familiar object. Other tests could also be used including Morris water mazes and episodic memory tests.

Encouragingly, unpublished work from our lab has shown that chronic implantation of lattice devices that were roughly half the overall size of the lattice devices described in Chapters 2 and 3 of this work did not induce a significant decrease in neurogenesis. Combining these observations with the results presented in this work indicates that a device's influence on neurogenesis may be dependent on its inflammatory footprint. This assumption increases the need for strategies, such as those described in this work, to reduce the FBR and the importance of further investigations into detrimental systemic impacts of the FBR.

While we have shown the potential of our passive strategies to reduce the FBR to microelectrodes, there are still a number of ways that we could modify these strategies to further enhance their impact. For example, our permeable hydrogel coatings could be used to deliver therapeutic agents such as anti-inflammatory drugs. As described in the introduction, systemic applications of these molecules have been used previously to improve recording function. However, a sustained, systemic delivery of these agents may have undesirable long-term-effects. In addition to the delivery of pharmaceutics, primary cells could

also be encapsulated and delivered using semipermeable hydrogels. The potential of using delivered cells as a source of therapeutics to reduce the FBR has been proven in previous work from our lab where we encapsulated immature astrocytes in a HFM system. These astrocyte-filled HFMs elicited a very minimal FBR that was even lower than the limited FBR to control empty HFMs.

When discussing the potential of various strategies to reduce the FBR and improve recording performance it should be noted that there are a number of discrepancies between the methods used by groups focused on device biocompatibility and those used by groups focused on the development of BMI applications. To date, the majority of studies examining the FBR have used single-shank devices such as planar MI-arrays or single cylindrical microwires. These simple devices have facilitated quantitative analysis of the FBR and the creation of several strategies to reduce the FBR. However, the BMI field uses more complex multitine arrays in order to gather a sufficient number of useful signals to drive their neuroprosthetic applications. There is minimal information regarding the FBR to these devices. To provide the most relevant information to improve these more complex and clinically relevant devices, specifically now that a number of strategies have been presented to improve the FBR to single-shank implants, further effort must be given to analyzing the FBR to the multitine devices used in the BMI field and to translate what we have learned from single-shank implants to improve these clinically targeted devices.

To bridge this gap, we have begun to analyze the FBR to both a limited cohort of 10x10 UEAs implanted in cat cortex as well as 4x4 UEAs implanted in

rats. Additionally, we have created models, as described in Figure 2-6 and below in Figure 6-2, to verify that our model can explain unique features that we have observed in the FBR to the UEA. This model and our FBR data indicate that there is a minimal reaction near the recording tips of these devices. However, there is a very severe reaction underneath the base of the array that may reduce device performance or lead to device failure by disrupting cortical column circuitry, inducing extravastion of the device through the build up of fibrous tissue beneath the devices base, or device settling via chronic tissue necrosis and erosion. Encouragingly our model indicates that similar strategies used to reduce the FBR to single planar implants, reducing device surface area or incorporating permeable coatings, may reduce the severity of the FBR below the devices base. Figure 6-2 depicts the predicted distribution of macrophage-secreted factors below a 4x4 UEA with a solid base and one with a lattice base. Figure 6-3 compares the predicted maximum concentration of released soluble factors surrounding these solid and lattice based UEAs with the 300μm planar and lattice devices as a function of depth into tissue.

Finally, one area that also needs to be addressed is the impact of these new design strategies on recording function. While there is evidence promoting the theory that the FBR impacts device function, showing that we can proactively improve performance will further verify and establish this theory and the importance of reducing the FBR to future device designs. To accomplish this we are collaborating with groups at the University of Michigan and with Blackrock microsystems.

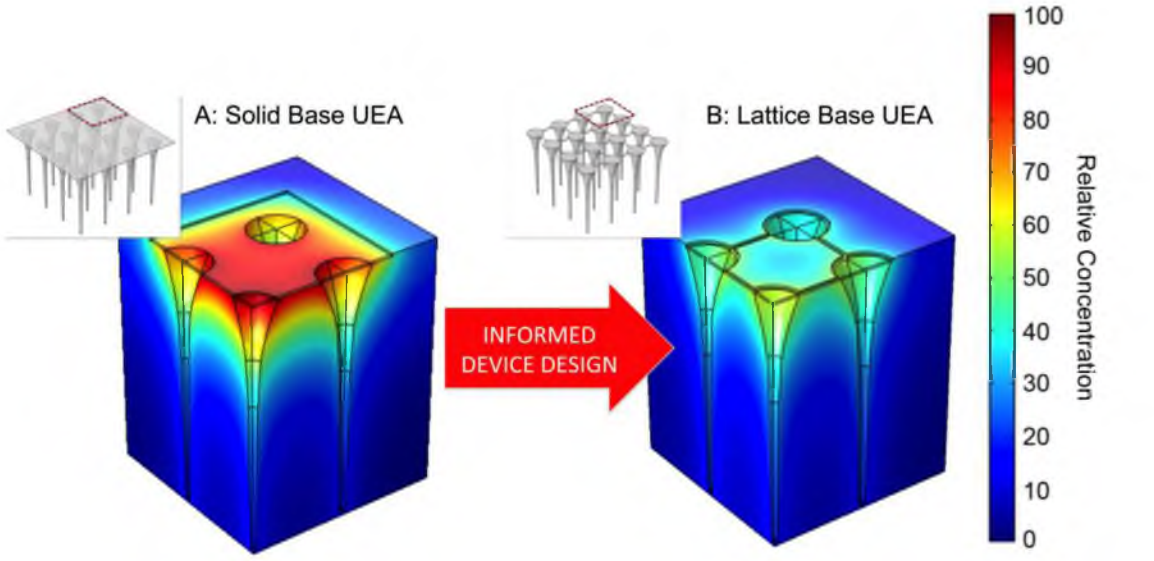

Figure 6-2: (A) Cross section of diffusion model for a 4x4 traditional solid base UEA. Concentrations are set relative to maximum in this model, not the 300µm solid as in other models. Similar to the graded severity of the FBR to traditional UEA designs, our model predicts greater concentrations of macrophage released factors underneath the base of the array and reduced concentrations near the recording tips. (B) Diffusion modeling predicts a significant reduction in the relative concentration of cytokines or other soluble factors surrounding a lattice base variant of the UEA.

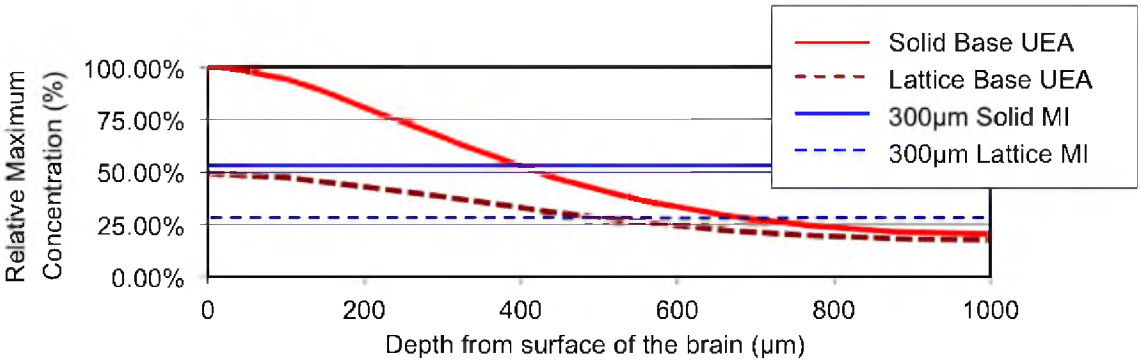

Figure 6-3: Comparison of the relative maximum concentration surrounding the solid and lattice based UEAs and MI arrays described in this work. Our model predicts significantly higher concentrations in superficial regions of the cortex. This increased concentration is a likely cause for a number of documented failure mechanisms of the UEA. However, due to the decreased profile and adequate tine spacing our model predicts a reduced distribution of macrophage released soluble factors at the recording tips even compared to our 300µm planar lattice design. By removing the majority of base material using a lattice design, our model predicts that we can significantly reduce the concentration of macrophage-secreted factors in this region, which should improve device function.

REFERENCES

[1] Dorsey ER, Constantinescu R, Thompson JP, Biglan KM, Holloway RG, Kieburtz K, et al. Projected number of people with Parkinson disease in the most populous nations, 2005 through 2030. Neurology 2007;68:384-6.

[2] Huse DM, Schulman K, Orsini L, Castelli-Haley J, Kennedy S, Lenhart G. Burden of illness in Parkinson's disease. Movement Disord 2005;20:1449-54.

[3] Lees AJ, Hardy J, Revesz T. Parkinson's disease. Lancet 2009;373:2055-66.

[4] Cummings JL. Alzheimer's disease. New Engl J Med 2004;351:56-67.

[5] Ernst RL, Hay JW. The US economic and social costs of Alzheimer's disease revisited. Am J Public Health 1994;84:1261-4.

[6] Hebert LE, Beckett LA, Scherr PA, Evans DA. Annual incidence of Alzheimer disease in the United States projected to the years 2000 through 2050. Alzheimer Dis Assoc Disord 2001;15:169-73.

[7] Anderson DW, Ellenberg JH, Leventhal CM, Reingold SC, Rodriguez M, Silberberg DH. Revised estimate of the prevalence of multiple sclerosis in the United States. Ann Neurol 1992;31:333-6.

[8] Noseworthy JH, Lucchinetti C, Rodriguez M, Weinshenker BG. Multiple sclerosis. New Engl J Med 2000;343:938-52.

[9] Whetten-Goldstein K, Sloan FA, Goldstein LB, Kulas ED. A comprehensive assessment of the cost of multiple sclerosis in the United States. Mult Scler 1998;4:419-25.

[10] Patwardhan RV, Nanda A. Implanted ventricular shunts in the United States: the billion-dollar-a-year cost of hydrocephalus treatment. Neurosurgery 2005;56:139-44; discussion 44-5.

[11] Simon TD, Riva-Cambrin J, Srivastava R, Bratton SL, Dean JM, Kestle JR. Hospital care for children with hydrocephalus in the United States: utilization, charges, comorbidities, and deaths. J Neurosurg Pediatr 2008;1:131-7.

[12] Runyan DK. The challenges of assessing the incidence of inflicted traumatic brain injury: a world perspective. Am J Prev Med 2008;34:S112-5.

[13] Selassie AW, Zaloshnja E, Langlois JA, Miller T, Jones P, Steiner C. Incidence of long-term disability following traumatic brain injury hospitalization, United States, 2003. J Head Trauma Rehab 2008;23:123-31.

[14] Rutland-Brown W, Langlois JA, Thomas KE, Xi YL. Incidence of traumatic brain injury in the United States, 2003. J Head Trauma Rehab 2006;21:544-8.

[15] Sekhon LH, Fehlings MG. Epidemiology, demographics, and pathophysiology of acute spinal cord injury. Spine 2001;26:S2-12.

[16] van den Berg ME, Castellote JM, Mahillo-Fernandez I, de Pedro-Cuesta J. Incidence of spinal cord injury worldwide: a systematic review. Neuroepidemiology 2010;34:184-92; discussion 92.

[17] Evans AH, Lawrence AD, Lees AJ. Changes in psychomotor effects of L-dopa and methylphenidate after sustained dopaminergic therapy in Parkinson's disease. J Neurol Neurosurg Psychiatry 2009;80:267-72.

[18] Lim SY, O'Sullivan SS, Kotschet K, Gallagher DA, Lacey C, Lawrence AD, et al. Dopamine dysregulation syndrome, impulse control disorders and punding after deep brain stimulation surgery for Parkinson's disease. J Clin Neurosci 2009;16:1148-52.

[19] Pierson J, Norris JL, Aerni HR, Svenningsson P, Caprioli RM, Andren PE. Molecular profiling of experimental Parkinson's disease: direct analysis of peptides and proteins on brain tissue sections by MALDI mass spectrometry. J Proteome Res 2004;3:289-95.

[20] Selikhova M, Williams DR, Kempster PA, Holton JL, Revesz T, Lees AJ. A clinico-pathological study of subtypes in Parkinson's disease. Brain 2009;132:2947-57.

[21] Cummings JL. Treatment of Alzheimer's disease: current and future therapeutic approaches. Rev Neurol Dis 2004;1:60-9.

[22] Cummings JL, Schneider L, Tariot PN, Kershaw PR, Yuan W. Reduction of behavioral disturbances and caregiver distress by galantamine in patients with Alzheimer's disease. Am J Psychiatry 2004;161:532-8.

[23] Adlard PA, Cummings BJ. Alzheimer's disease--a sum greater than its parts? Neurobiol Aging 2004;25:725-33; discussion 43-6.

[24] Bartzokis G, Sultzer D, Lu PH, Nuechterlein KH, Mintz J, Cummings JL. Heterogeneous age-related breakdown of white matter structural integrity:

implications for cortical "disconnection" in aging and Alzheimer's disease. Neurobiol Aging 2004;25:843-51.

[25] Swanberg MM, Tractenberg RE, Mohs R, Thal LJ, Cummings JL. Executive dysfunction in Alzheimer disease. Arch Neurol 2004;61:556-60.

[26] Waltz JA, Knowlton BJ, Holyoak KJ, Boone KB, Back-Madruga C, McPherson S, et al. Relational integration and executive function in Alzheimer's disease. Neuropsychology 2004;18:296-305.

[27] Wynn ZJ, Cummings JL. Cholinesterase inhibitor therapies and neuropsychiatric manifestations of Alzheimer's disease. Dement Geriatr Cogn Disord 2004;17:100-8.

[28] Beer S, Khan F, Kesselring J. Rehabilitation interventions in multiple sclerosis: an overview. J Neurol 2012.

[29] Johnston J, So TY. First-line disease-modifying therapies in paediatric multiple sclerosis: a comprehensive overview. Drugs 2012;72:1195-211.

[30] Kurtuncu M, Tuzun E, Turkoglu R, Petek-Balci B, Icoz S, Pehlivan M, et al. Effect of short-term interferon-beta treatment on cytokines in multiple sclerosis: significant modulation of IL-17 and IL-23. Cytokine 2012;59:400-2.

[31] Lee S, Baxter DC, Limone B, Roberts MS, Coleman CI. Cost-effectiveness of fingolimod versus interferon beta-1a for relapsing remitting multiple sclerosis in the United States. J Med Econ 2012.

[32] Marta M, Giovannoni G. Disease Modifying Drugs in Multiple Sclerosis: mechanisms of action and new drugs in the horizon. Curr Drug Targets: CNS Neurol Disord 2012.

[33] Meuth SG, Gobel K, Wiendl H. Immune therapy of multiple sclerosis - future strategies. Curr Pharm Des 2012.

[34] Pikoulas TE, Fuller MA. Dalfampridine: a medication to improve walking in patients with multiple sclerosis (July/August). Ann Pharmacother 2012.

[35] Eskandari R, Harris CA, McAllister JP, 2nd. Reactive astrocytosis in feline neonatal hydrocephalus: acute, chronic, and shunt-induced changes. Childs Nerv Syst 2011;27:2067-76.

[36] Harris CA, McAllister JP, 2nd. What we should know about the cellular and tissue response causing catheter obstruction in the treatment of hydrocephalus. Neurosurgery 2012;70:1589-601; discussion 601-2.

[37] Jones HC, Harris NG, Rocca JR, Andersohn RW. Progressive changes in cortical metabolites at three stages of infantile hydrocephalus studied by in vitro NMR spectroscopy. J Neurotrauma 1997;14:587-602.

[38] Jones HC, Harris NG, Rocca JR, Andersohn RW. Progressive tissue injury in infantile hydrocephalus and prevention/reversal with shunt treatment. Neurol Res 2000;22:89-96.

[39] Manning FA, Harrison MR, Rodeck C. Catheter shunts for fetal hydronephrosis and hydrocephalus. Report of the International Fetal Surgery Registry. New Engl J Med 1986;315:336-40.

[40] O'Brien MS, Harris ME. Long-term results in the treatment of hydrocephalus. Neurosurg Clin N Am 1993;4:625-32.

[41] Pena A, Harris NG, Bolton MD, Czosnyka M, Pickard JD. Communicating hydrocephalus: the biomechanics of progressive ventricular enlargement revisited. Acta Neurochir Suppl 2002;81:59-63.

[42] Cameron KL, Marshall SW, Sturdivant RX, Lincoln AE. Trends in the incidence of physician-diagnosed mild traumatic brain injury among active duty U.S. military personnel between 1997 and 2007. J Neurotrauma 2012;29:1313-21.

[43] Theadom A, Barker-Collo S, Feigin VL, Starkey NJ, Jones K, Jones A, et al. The spectrum captured: a methodological approach to studying incidence and outcomes of traumatic brain injury on a population level. Neuroepidemiology 2012;38:18-29.

[44] Leibson CL, Brown AW, Ransom JE, Diehl NN, Perkins PK, Mandrekar J, et al. Incidence of traumatic brain injury across the full disease spectrum: a population-based medical record review study. Epidemiology 2011;22:836-44.

[45] Nicholl J, LaFrance WC, Jr. Neuropsychiatric sequelae of traumatic brain injury. Semin Neurol 2009;29:247-55.

[46] Fehlings MG, Sekhon LH. Acute interventions in spinal cord injury: what do we know, what should we do? Clin Neurosurg 2001;48:226-42.

[47] Young RF, Brechner T. Electrical stimulation of the brain for relief of intractable pain due to cancer. Cancer 1986;57:1266-72.

[48] Lakhan SE, Callaway E. Deep brain stimulation for obsessive-compulsive disorder and treatment-resistant depression: systematic review. BMC Res Notes 2010;3:60.

[49] Baru JS, Bloom DA, Muraszko K, Koop CE. John Holter's shunt. J Am Coll Surg 2001;192:79-85.

[50] Joosten EA. Biodegradable biomatrices and bridging the injured spinal cord: the corticospinal tract as a proof of principle. Cell Tissue Res 2012;349:375-95.

[51] Chow WN, Simpson DG, Bigbee JW, Colello RJ. Evaluating neuronal and glial growth on electrospun polarized matrices: bridging the gap in percussive spinal cord injuries. Neuron Glia Biol 2007;3:119-26.

[52] Yoshii S, Oka M, Shima M, Akagi M, Taniguchi A. Bridging a spinal cord defect using collagen filament. Spine 2003;28:2346-51.

[53] Iannotti C, Li H, Yan P, Lu X, Wirthlin L, Xu XM. Glial cell line-derived neurotrophic factor-enriched bridging transplants promote propriospinal axonal regeneration and enhance myelination after spinal cord injury. Exp Neurol 2003;183:379-93.

[54] Bunge MB. Bridging the transected or contused adult rat spinal cord with Schwann cell and olfactory ensheathing glia transplants. Prog Brain Res 2002;137:275-82.

[55] Bartolomei JC, Greer CA. Olfactory ensheathing cells: bridging the gap in spinal cord injury. Neurosurgery 2000;47:1057-69.

[56] Liu S, Bodjarian N, Langlois O, Bonnard AS, Boisset N, Peulve P, et al. Axonal regrowth through a collagen guidance channel bridging spinal cord to the avulsed C6 roots: functional recovery in primates with brachial plexus injury. J Neurosci Res 1998;51:723-34.

[57] Liu S, Peulve P, Jin O, Boisset N, Tiollier J, Said G, et al. Axonal regrowth through collagen tubes bridging the spinal cord to nerve roots. J Neurosci Res 1997;49:425-32.

[58] Xu XM, Chen A, Guenard V, Kleitman N, Bunge MB. Bridging Schwann cell transplants promote axonal regeneration from both the rostral and caudal stumps of transected adult rat spinal cord. J Neurocytol 1997;26:1-16.

[59] Houle JD, Ziegler MK. Bridging a complete transection lesion of adult rat spinal cord with growth factor-treated nitrocellulose implants. J Neural Transplant Plast 1994;5:115-24.

[60] Schwartz AB. Cortical neural prosthetics. Annu Rev Neurosci 2004;27:487-507.

[61] Nicolelis MA, Ribeiro S. Multielectrode recordings: the next steps. Curr Opin Neurobiol 2002;12:602-6.

[62] Kennedy PR, Bakay RA, Moore MM, Adams K, Goldwaithe J. Direct control of a computer from the human central nervous system. IEEE Trans Rehabil Eng 2000;8:198-202.

[63] Kellis S, Miller K, Thomson K, Brown R, House P, Greger B. Decoding spoken words using local field potentials recorded from the cortical surface. J Neural Eng 2010;7:056007.

[64] Strumwasser F. Long-term recording' from single neurons in brain of unrestrained mammals. Science 1958;127:469-70.

[65] Hubel DH. Tungsten Microelectrode for recording from single units. Science 1957;125:549-50.

[66] Campbell PK, Jones KE, Huber RJ, Horch KW, Normann RA. A silicon-based, three-dimensional neural interface: manufacturing processes for an intracortical electrode array. IEEE Trans Biomed Eng 1991;38:758-68.

[67] Jones KE, Campbell PK, Normann RA. A glass/silicon composite intracortical electrode array. Ann Biomed Eng 1992;20:423-37.

[68] Wise KD, Angell JB, Starr A. An integrated-circuit approach to extracellular microelectrodes. IEEE Trans Biomed Eng 1970;17:238-47.

[69] BeMent SL, Wise KD, Anderson DJ, Najafi K, Drake KL. Solid-state electrodes for multichannel multiplexed intracortical neuronal recording. IEEE Trans Biomed Eng 1986;33:230-41.

[70] Drake KL, Wise KD, Farraye J, Anderson DJ, BeMent SL. Performance of planar multisite microprobes in recording extracellular single-unit intracortical activity. IEEE Trans Biomed Eng 1988;35:719-32.

[71] Ratner BD. The biocompatibility manifesto: biocompatibility for the twenty-first century. J Cardiovasc Transl Res 2011;4:523-7.

[72] Burbaud P, Vital A, Rougier A, Bouillot S, Guehl D, Cuny E, et al. Minimal tissue damage after stimulation of the motor thalamus in a case of chorea-acanthocytosis. Neurology 2002;59:1982-4.

[73] Caparros-Lefebvre D, Ruchoux MM, Blond S, Petit H, Percheron G. Long-term thalamic stimulation in Parkinson's disease: postmortem anatomoclinical study. Neurology 1994;44:1856-60.

[74] Chou KL, Forman MS, Trojanowski JQ, Hurtig HI, Baltuch GH. Subthalamic nucleus deep brain stimulation in a patient with levodopa-responsive multiple system atrophy. Case report. J Neurosurg 2004;100:553-6.

[75] Haberler C, Alesch F, Mazal PR, Pilz P, Jellinger K, Pinter MM, et al. No tissue damage by chronic deep brain stimulation in Parkinson's disease. Ann Neurol 2000;48:372-6.

[76] Henderson JM, Pell M, O'Sullivan DJ, McCusker EA, Fung VS, Hedges P, et al. Postmortem analysis of bilateral subthalamic electrode implants in Parkinson's disease. Movement Disord 2002;17:133-7.

[77] Jarraya B, Bonnet AM, Duyckaerts C, Houeto JL, Cornu P, Hauw JJ, et al. Parkinson's disease, subthalamic stimulation, and selection of candidates: a pathological study. Movement Disord 2003;18:1517-20.

[78] Moss J, Ryder T, Aziz TZ, Graeber MB, Bain PG. Electron microscopy of tissue adherent to explanted electrodes in dystonia and Parkinson's disease. Brain 2004;127:2755-63.

[79] Nielsen MS, Bjarkam CR, Sorensen JC, Bojsen-Moller M, Sunde NA, Ostergaard K. Chronic subthalamic high-frequency deep brain stimulation in Parkinson's disease--a histopathological study. Eur J Neurol 2007;14:132-8.

[80] Pilitsis JG, Chu Y, Kordower J, Bergen DC, Cochran EJ, Bakay RA. Postmortem study of deep brain stimulation of the anterior thalamus: case report. Neurosurgery 2008;62:E530-2; discussion E2.

[81] Dujardin K, Defebvre L, Krystkowiak P, Blond S, Destee A. Influence of chronic bilateral stimulation of the subthalamic nucleus on cognitive function in Parkinson's disease. J Neurol 2001;248:603-11.

[82] Lueken U, Schwarz M, Hertel F, Schweiger E, Wittling W. Impaired performance on the Wisconsin Card Sorting Test under left- when compared to right-sided deep brain stimulation of the subthalamic nucleus in patients with Parkinson's disease. J Neurol 2008;255:1940-8.

[83] Trepanier LL, Kumar R, Lozano AM, Lang AE, Saint-Cyr JA. Neuropsychological outcome of GPi pallidotomy and GPi or STN deep brain stimulation in Parkinson's disease. Brain Cognit 2000;42:324-47.

[84] Witt K, Daniels C, Reiff J, Krack P, Volkmann J, Pinsker MO, et al. Neuropsychological and psychiatric changes after deep brain stimulation for Parkinson's disease: a randomised, multicentre study. Lancet Neurol 2008;7:605-14.

[85] York MK, Dulay M, Macias A, Levin HS, Grossman R, Simpson R, et al. Cognitive declines following bilateral subthalamic nucleus deep brain stimulation for the treatment of Parkinson's disease. J Neurol Neurosurg Psychiatry 2008;79:789-95.

[86] Enchev Y, Oi S. Historical trends of neuroendoscopic surgical techniques in the treatment of hydrocephalus. Neurosurg Rev 2008;31:249-62.

[87] Del Bigio MR. Biological reactions to cerebrospinal fluid shunt devices: a review of the cellular pathology. Neurosurgery 1998;42:319-25; discussion 25-6.

[88] Ellis MJ, Kazina CJ, Del Bigio MR, McDonald PJ. Treatment of recurrent ventriculoperitoneal shunt failure associated with persistent cerebrospinal fluid eosinophilia and latex allergy by use of an "extracted" shunt. J Neurosurg Pediatr 2008;1:237-9.

[89] Thomale UW, Hosch H, Koch A, Schulz M, Stoltenburg G, Haberl EJ, et al. Perforation holes in ventricular catheters--is less more? Childs Nerv Syst 2010;26:781-9.

[90] Woodruff WW, Jr., Yeates AE, Dent GA. Ventricular shunt therapy of the brain: long-term rubber-catheter-induced inflammation. Radiology 1986;158:171-4.

[91] Hommet C, Billard C, Gillet P, Barthez MA, Lourmiere JM, Santini JJ, et al. Neuropsychologic and adaptive functioning in adolescents and young adults shunted for congenital hydrocephalus. J Child Neurol 1999;14:144-50.

[92] Iddon JL, Pickard JD, Cross JJ, Griffiths PD, Czosnyka M, Sahakian BJ. Specific patterns of cognitive impairment in patients with idiopathic normal pressure hydrocephalus and Alzheimer's disease: a pilot study. J Neurol Neurosurg Psychiatry 1999;67:723-32.

[93] Lacy M, Pyykkonen BA, Hunter SJ, Do T, Oliveira M, Austria E, et al. Intellectual functioning in children with early shunted posthemorrhagic hydrocephalus. Pediatr Neurosurg 2008;44:376-81.

[94] Hochberg LR, Serruya MD, Friehs GM, Mukand JA, Saleh M, Caplan AH, et al. Neuronal ensemble control of prosthetic devices by a human with tetraplegia. Nature 2006;442:164-71.

[95] Kennedy PR, Kirby MT, Moore MM, King B, Mallory A. Computer control using human intracortical local field potentials. IEEE Trans Neural Syst Rehabil Eng 2004;12:339-44.

[96] Musallam S, Corneil BD, Greger B, Scherberger H, Andersen RA. Cognitive control signals for neural prosthetics. Science 2004;305:258-62.

[97] Nicolelis MA, Dimitrov D, Carmena JM, Crist R, Lehew G, Kralik JD, et al. Chronic, multisite, multielectrode recordings in macaque monkeys. Proc Natl Acad Sci U S A 2003;100:11041-6.

[98] Burns BD, Stean JP, Webb AC. Recording for several days from single cortical neurons in completely unrestrained cats. Electroencephalogr Clin Neurophysiol 1974;36:314-8.

[99] Liu X, McCreery DB, Bullara LA, Agnew WF. Evaluation of the stability of intracortical microelectrode arrays. IEEE Trans Neural Syst Rehabil Eng 2006;14:91-100.

[100] Liu X, McCreery DB, Carter RR, Bullara LA, Yuen TG, Agnew WF. Stability of the interface between neural tissue and chronically implanted intracortical microelectrodes. IEEE Trans Rehabil Eng 1999;7:315-26.

[101] Schmidt EM, Bak MJ, McIntosh JS. Long-term chronic recording from cortical neurons. Exp Neurol 1976;52:496-506.

[102] Schmidt EM, McIntosh JS, Bak MJ. Long-term implants of Parylene-C coated microelectrodes. Med Biol Eng Comput 1988;26:96-101.

[103] Barrese JC NR, Triebwasser C, Paroo K, Vargas-Irwin C, Franquemont L, Donoghue J. Failure mode analysis of silicon-based intracortical microelectrode arrays in non-human primates. Neural Interfaces Conf 2012.

[104] Rennaker RL, Miller J, Tang H, Wilson DA. Minocycline increases quality and longevity of chronic neural recordings. J Neural Eng 2007;4:L1-5.

[105] Collias JC, Manuelidis EE. Histopathological changes produced by implanted electrodes in cat brains; comparison with histopathological changes in human and experimental puncture wounds. J Neurosurg 1957;14:302-28.

[106] Tang L. Mechanisms of fibrinogen domains: biomaterial interactions. J Biomater Sci, Polym Ed 1998;9:1257-66.

[107] Nilsson B, Ekdahl KN, Mollnes TE, Lambris JD. The role of complement in biomaterial-induced inflammation. Mol Immunol 2007;44:82-94.

[108] Biran R, Martin DC, Tresco PA. Neuronal cell loss accompanies the brain tissue response to chronically implanted silicon microelectrode arrays. Exp Neurol 2005;195:115-26.

[109] Winslow BD, Christensen MB, Yang WK, Solzbacher F, Tresco PA. A comparison of the tissue response to chronically implanted Parylene-C-coated and uncoated planar silicon microelectrode arrays in rat cortex. Biomaterials 2010.

[110] Biran R, Martin DC, Tresco PA. The brain tissue response to implanted silicon microelectrode arrays is increased when the device is tethered to the skull. J Biomed Mater Res A 2007;82:169-78.

[111] Winslow BD, Tresco PA. Quantitative analysis of the tissue response to chronically implanted microwire electrodes in rat cortex. Biomaterials 2010;31:1558-67.

[112] Gehrmann J, Matsumoto Y, Kreutzberg GW. Microglia: intrinsic immuneffector cell of the brain. Brain Res Rev 1995;20:269-87.

[113] Betjes MG, Tuk CW, Struijk DG, Krediet RT, Arisz L, Beelen RH. Antigen-presenting capacity of macrophages and dendritic cells in the peritoneal cavity of patients treated with peritoneal dialysis. Clin Exp Immunol 1993;94:377-84.

[114] Gregerson DS, Sam TN, McPherson SW. The antigen-presenting activity of fresh, adult parenchymal microglia and perivascular cells from retina. J Immunol 2004;172:6587-97.

[115] Shaked I, Porat Z, Gersner R, Kipnis J, Schwartz M. Early activation of microglia as antigen-presenting cells correlates with T cell-mediated protection and repair of the injured central nervous system. J Neuroimmunol 2004;146:84-93.

[116] Mack CL, Vanderlugt-Castaneda CL, Neville KL, Miller SD. Microglia are activated to become competent antigen presenting and effector cells in the inflammatory environment of the Theiler's virus model of multiple sclerosis. J Neuroimmunol 2003;144:68-79.

[117] Carson MJ, Reilly CR, Sutcliffe JG, Lo D. Mature microglia resemble immature antigen-presenting cells. Glia 1998;22:72-85.

[118] Poltorak M, Freed WJ. Immunological reactions induced by intracerebral transplantation: evidence that host microglia but not astroglia are the antigen-presenting cells. Exp Neurol 1989;103:222-33.

[119] Block ML, Zecca L, Hong JS. Microglia-mediated neurotoxicity: uncovering the molecular mechanisms. Nat Rev Neurosci 2007;8:57-69.

[120] Chao CC, Hu S, Peterson PK. Glia, cytokines, and neurotoxicity. Crit Rev Neurobiol 1995;9:189-205.

[121] Hanisch UK, Kettenmann H. Microglia: active sensor and versatile effector cells in the normal and pathologic brain. Nat Neurosci 2007;10:1387-94.

[122] Henze DA, Borhegyi Z, Csicsvari J, Mamiya A, Harris KD, Buzsaki G. Intracellular features predicted by extracellular recordings in the hippocampus in vivo. J Neurophysiol 2000;84:390-400.

[123] Mantovani A, Sozzani S, Locati M, Allavena P, Sica A. Macrophage polarization: tumor-associated macrophages as a paradigm for polarized M2 mononuclear phagocytes. Trends Immunol 2002;23:549-55.

[124] Quagliarello VJ, Wispelwey B, Long WJ, Jr., Scheld WM. Recombinant human interleukin-1 induces meningitis and blood-brain barrier injury in the rat. Characterization and comparison with tumor necrosis factor. J Clin Invest 1991;87:1360-6.

[125] Clark IA, Alleva LM, Vissel B. The roles of TNF in brain dysfunction and disease. Pharmacol Ther 2010;128:519-48.

[126] Feuerstein GZ, Liu T, Barone FC. Cytokines, inflammation, and brain injury: role of tumor necrosis factor-alpha. Cerebrovasc Brain Metab Rev 1994;6:341-60.

[127] Ghirnikar RS, Lee YL, Eng LF. Inflammation in traumatic brain injury: role of cytokines and chemokines. Neurochem Res 1998;23:329-40.

[128] Gosselin D, Rivest S. Role of IL-1 and TNF in the brain: twenty years of progress on a Dr. Jekyll/Mr. Hyde duality of the innate immune system. Brain Behav Immun 2007;21:281-9.

[129] Stamatovic SM, Keep RF, Kunkel SL, Andjelkovic AV. Potential role of MCP-1 in endothelial cell tight junction 'opening': signaling via Rho and Rho kinase. J Cell Sci 2003;116:4615-28.

[130] Stamatovic SM, Shakui P, Keep RF, Moore BB, Kunkel SL, Van Rooijen N, et al. Monocyte chemoattractant protein-1 regulation of blood-brain barrier permeability. J Cereb Blood Flow Metab 2005;25:593-606.

[131] Sugama S, Takenouchi T, Cho BP, Joh TH, Hashimoto M, Kitani H. Possible roles of microglial cells for neurotoxicity in clinical neurodegenerative diseases and experimental animal models. Inflamm Allergy Drug Targets 2009;8:277-84.

[132] Yadav A, Saini V, Arora S. MCP-1: chemoattractant with a role beyond immunity: a review. Clin Chim Acta 2010;411:1570-9.

[133] Edell DJ, Toi VV, McNeil VM, Clark LD. Factors influencing the biocompatibility of insertable silicon microshafts in cerebral cortex. IEEE Trans Biomed Eng 1992;39:635-43.

[134] Schmidt S, Horch K, Normann R. Biocompatibility of silicon-based electrode arrays implanted in feline cortical tissue. J Biomed Mater Res 1993;27:1393-9.

[135] Schultz RL, Willey TJ. The ultrastructure of the sheath around chronically implanted electrodes in brain. J Neurocytol 1976;5:621-42.

[136] Seymour JP, Kipke DR. Neural probe design for reduced tissue encapsulation in CNS. Biomaterials 2007;28:3594-607.

[137] Stensaas SS, Stensaas LJ. The reaction of the cerebral cortex to chronically implanted plastic needles. Acta Neuropathol 1976;35:187-203.

[138] Stensaas SS, Stensaas LJ. Histopathological evaluation of materials implanted in the cerebral cortex. Acta Neuropathol 1978;41:145-55.

[139] Szarowski DH, Andersen MD, Retterer S, Spence AJ, Isaacson M, Craighead HG, et al. Brain responses to micro-machined silicon devices. Brain Res 2003;983:23-35.

[140] Thelin J, Jorntell H, Psouni E, Garwicz M, Schouenborg J, Danielsen N, et al. Implant size and fixation mode strongly influence tissue reactions in the CNS. PLoS One 2011;6:e16267.

[141] Huang YH, Sinha SR, Tanaka K, Rothstein JD, Bergles DE. Astrocyte glutamate transporters regulate metabotropic glutamate receptor-mediated excitation of hippocampal interneurons. J Neurosci 2004;24:4551-9.

[142] Andjelkovic AV, Kerkovich D, Pachter JS. Monocyte: astrocyte interactions regulate MCP-1 expression in both cell types. J Leukoc Biol 2000;68:545-52.

[143] Abbott NJ. Astrocyte-endothelial interactions and blood-brain barrier permeability. J Anat 2002;200:629-38.

[144] Goldstein GW. Endothelial cell-astrocyte interactions. A cellular model of the blood-brain barrier. Ann NY Acad Sci 1988;529:31-9.

[145] Schmid-Brunclik N, Burgi-Taboada C, Antoniou X, Gassmann M, Ogunshola OO. Astrocyte responses to injury: VEGF simultaneously modulates cell death and proliferation. Am J Physiol Regul Integr Comp Physiol 2008;295:R864-73.

[146] Aschner M, Sonnewald U, Tan KH. Astrocyte modulation of neurotoxic injury. Brain Pathol 2002;12:475-81.

[147] Louw DF, Masada T, Sutherland GR. Ischemic neuronal injury is ameliorated by astrocyte activation. Can J Neurol Sci 1998;25:102-7.

[148] Guenard V, Frisch G, Wood PM. Effects of axonal injury on astrocyte proliferation and morphology in vitro: implications for astrogliosis. Exp Neurol 1996;137:175-90.

[149] Norenberg MD. Astrocyte responses to CNS injury. J Neuropathol Exp Neurol 1994;53:213-20.

[150] Burbaud P, Rougier A, Ferrer X, Guehl D, Cuny E, Arne P, et al. Improvement of severe trunk spasms by bilateral high-frequency stimulation of the motor thalamus in a patient with chorea-acanthocytosis. Movement Disord 2002;17:204-7.

[151] Aihara N, Tanno H, Hall JJ, Pitts LH, Noble LJ. Immunocytochemical localization of immunoglobulins in the rat brain: relationship to the blood-brain barrier. J Comp Neurol 1994;342:481-96.

[152] Azzi G, Bernaudin JF, Bouchaud C, Bellon B, Fleury-Feith J. Permeability of the normal rat brain, spinal cord and dorsal root ganglia microcirculations to immunoglobulins G. Biol Cell 1990;68:31-6.

[153] Seitz RJ, Heininger K, Schwendemann G, Toyka KV, Wechsler W. The mouse blood-brain barrier and blood-nerve barrier for IgG: a tracer study by use of the avidin-biotin system. Acta Neuropathol 1985;68:15-21.

[154] Lassmann H. A dynamic view of the blood-brain barrier in active multiple sclerosis lesions. Ann Neurol 2011;70:1-2.

[155] Larochelle C, Alvarez JI, Prat A. How do immune cells overcome the blood-brain barrier in multiple sclerosis? FEBS Lett 2011;585:3770-80.

[156] Mu Y, Gage FH. Adult hippocampal neurogenesis and its role in Alzheimer's disease. Mol Neurodegener 2011;6:85.

[157] Biscaro B, Lindvall O, Tesco G, Ekdahl CT, Nitsch RM. Inhibition of microglial activation protects hippocampal neurogenesis and improves cognitive deficits in a transgenic mouse model for Alzheimer's disease. Neurodegener Dis 2012;9:187-98.

[158] Stice P, Gilletti A, Panitch A, Muthuswamy J. Thin microelectrodes reduce GFAP expression in the implant site in rodent somatosensory cortex. J Neural Eng 2007;4:42-53.

[159] Goldstein SR, Salcman M. Mechanical factors in the design of chronic recording intracortical microelectrodes. IEEE Trans Biomed Eng 1973;20:260-9.

[160] Harris JP, Capadona JR, Miller RH, Healy BC, Shanmuganathan K, Rowan SJ, et al. Mechanically adaptive intracortical implants improve the proximity of neuronal cell bodies. J Neural Eng 2011;8:066011.

[161] Harris JP, Hess AE, Rowan SJ, Weder C, Zorman CA, Tyler DJ, et al. In vivo deployment of mechanically adaptive nanocomposites for intracortical microelectrodes. J Neural Eng 2011;8:046010.

[162] Kim YT, Hitchcock RW, Bridge MJ, Tresco PA. Chronic response of adult rat brain tissue to implants anchored to the skull. Biomaterials 2004;25:2229-37.

[163] Leung BK, Biran R, Underwood CJ, Tresco PA. Characterization of microglial attachment and cytokine release on biomaterials of differing surface chemistry. Biomaterials 2008;29:3289-97.

[164] He W, McConnell GC, Bellamkonda RV. Nanoscale laminin coating modulates cortical scarring response around implanted silicon microelectrode arrays. J Neural Eng 2006;3:316-26.

[165] Azemi E, Stauffer WR, Gostock MS, Lagenaur CF, Cui XT. Surface immobilization of neural adhesion molecule L1 for improving the biocompatibility of chronic neural probes: in vitro characterization. Acta Biomater 2008;4:1208-17.

[166] Azemi E, Lagenaur CF, Cui XT. The surface immobilization of the neural adhesion molecule L1 on neural probes and its effect on neuronal density and gliosis at the probe/tissue interface. Biomaterials 2011;32:681-92.

[167] Moxon KA, Kalkhoran NM, Markert M, Sambito MA, McKenzie JL, Webster JT. Nanostructured surface modification of ceramic-based microelectrodes to enhance biocompatibility for a direct brain-machine interface. IEEE Trans Biomed Eng 2004;51:881-9.

[168] Moxon KA, Leiser SC, Gerhardt GA, Barbee KA, Chapin JK. Ceramic-based multisite electrode arrays for chronic single-neuron recording. IEEE Trans Biomed Eng 2004;51:647-56.

[169] Moxon KA, Hallman S, Aslani A, Kalkhoran NM, Lelkes PI. Bioactive properties of nanostructured porous silicon for enhancing electrode to neuron interfaces. J Biomater Sci, Polym Ed 2007;18:1263-81.

[170] Zhong Y, Bellamkonda RV. Dexamethasone-coated neural probes elicit attenuated inflammatory response and neuronal loss compared to uncoated neural probes. Brain Res 2007;1148:15-27.

[171] Kruger J, Caruana F, Volta RD, Rizzolatti G. Seven years of recording from monkey cortex with a chronically implanted multiple microelectrode. Front Neuroeng 2010;3:6.

[172] Shain W, Spataro L, Dilgen J, Haverstick K, Retterer S, Isaacson M, et al. Controlling cellular reactive responses around neural prosthetic devices using peripheral and local intervention strategies. IEEE Trans Neural Syst Rehabil Eng 2003;11:186-8.

[173] Cheong R, Bergmann A, Werner SL, Regal J, Hoffmann A, Levchenko A. Transient IkappaB kinase activity mediates temporal NF-kappaB dynamics in response to a wide range of tumor necrosis factor-alpha doses. J Biol Chem 2006;281:2945-50.

[174] Hoffmann A, Levchenko A, Scott ML, Baltimore D. The IkappaB-NF-kappaB signaling module: temporal control and selective gene activation. Science 2002;298:1241-5.

[175] Francis K, Palsson BO. Effective intercellular communication distances are determined by the relative time constants for cyto/chemokine secretion and diffusion. Proceedings of the National Academy of Sciences of the United States of America 1997;94:12258-62.

[176] Goodhill GJ. Diffusion in axon guidance. Eur J Neurosci 1997;9:1414-21.

[177] Kim YT, Bridge MJ, Tresco PA. The influence of the foreign body response evoked by fibroblast transplantation on soluble factor diffusion in surrounding brain tissue. J Control Release 2007;118:340-7.

[178] Vorisek I, Sykova E. Evolution of anisotropic diffusion in the developing rat corpus callosum. J Neurophysiol 1997;78:912-9.

[179] Vorisek I, Sykova E. Ischemia-induced changes in the extracellular space diffusion parameters, K+, and pH in the developing rat cortex and corpus callosum. J Cereb Blood Flow Metab 1997;17:191-203.

[180] Xiao F, Nicholson C, Hrabe J, Hrabetova S. Diffusion of flexible random-coil dextran polymers measured in anisotropic brain extracellular space by integrative optical imaging. Biophys J 2008;95:1382-92.

[181] Liu T, Clark RK, McDonnell PC, Young PR, White RF, Barone FC, et al. Tumor necrosis factor-alpha expression in ischemic neurons. Stroke 1994;25:1481-8.

[182] Branner A, Stein RB, Fernandez E, Aoyagi Y, Normann RA. Long-term stimulation and recording with a penetrating microelectrode array in cat sciatic nerve. IEEE Trans Biomed Eng 2004;51:146-57.

[183] Sanders JE, Stiles CE, Hayes CL. Tissue response to single-polymer fibers of varying diameters: evaluation of fibrous encapsulation and macrophage density. J Biomed Mater Res 2000;52:231-7.

[184] Crane IJ, Xu H, Manivannan A, McKillop-Smith S, Lamont G, Wallace C, et al. Effect of anti-macrophage inflammatory protein-1alpha on leukocyte trafficking and disease progression in experimental autoimmune uveoretinitis. Eur J Immunol 2003;33:402-10.

[185] Xu H, Forrester JV, Liversidge J, Crane IJ. Leukocyte trafficking in experimental autoimmune uveitis: breakdown of blood-retinal barrier and upregulation of cellular adhesion molecules. Invest Ophth Vis Sci 2003;44:226-34.

[186] Biran R NM, Tresco PA. Directed nerve outgrowth is enhanced by engineered glial substrates. Exp Neurol 2003;184:141-52. .

[187] Elender G KM, Sackmann E. Functionalisation of Si/Si02 and glass surfaces with ultrathin dextran films and deposition of lipid bilayers. Biosens Bioelectron 1996;11:565-77.

[188] Luzinov I DJ, Liebmann-Vinson A, Cregger T, Foster MD, Tsukruk VV. Epoxy-terminated self-assembled monolayers: molecular glues for polymer layers. Langmuir 2000;16:504-16.

[189] Skousen JL, Merriam SM, Srivannavit O, Perlin G, Wise KD, Tresco PA. Reducing surface area while maintaining implant penetrating profile lowers the brain foreign body response to chronically implanted planar silicon microelectrode arrays. Prog Brain Res 2011;194:167-80.

[190] Lopez CA, Fleischman AJ, Roy S, Desai TA. Evaluation of silicon nanoporous membranes and ECM-based microenvironments on neurosecretory cells. Biomaterials 2006;27:3075-83.

[191] La Flamme KE, Popat KC, Leoni L, Markiewicz E, La Tempa TJ, Roman BB, et al. Biocompatibility of nanoporous alumina membranes for immunoisolation. Biomaterials 2007;28:2638-45.

[192] Rao L, Zhou H, Li T, Li C, Duan YY. Polyethylene glycol-containing polyurethane hydrogel coatings for improving the biocompatibility of neural electrodes. Acta Biomater 2012;8:2233-42.

[193] Kim MS, Ahn HH, Shin YN, Cho MH, Khang G, Lee HB. An in vivo study of the host tissue response to subcutaneous implantation of PLGA- and/or porcine small intestinal submucosa-based scaffolds. Biomaterials 2007;28:5137-43.

[194] Fujihara Y, Takato T, Hoshi K. Immunological response to tissue-engineered cartilage derived from auricular chondrocytes and a PLLA scaffold in transgenic mice. Biomaterials 2010;31:1227-34.

[195] Allman AJ, McPherson TB, Badylak SF, Merrill LC, Kallakury B, Sheehan C, et al. Xenogeneic extracellular matrix grafts elicit a TH2-restricted immune response. Transplantation 2001;71:1631-40.

[196] Allaire E, Bruneval P, Mandet C, Becquemin JP, Michel JB. The immunogenicity of the extracellular matrix in arterial xenografts. Surgery 1997;122:73-81.

[197] Allaire E, Mandet C, Bruneval P, Bensenane S, Becquemin JP, Michel JB. Cell and extracellular matrix rejection in arterial concordant and discordant xenografts in the rat. Transplantation 1996;62:794-803.

[198] Allaire E, Guettier C, Bruneval P, Plissonnier D, Michel JB. Cell-free arterial grafts: morphologic characteristics of aortic isografts, allografts, and xenografts in rats. J Vasc Surg 1994;19:446-56.

[199] McClelland R, Wauthier E, Uronis J, Reid L. Gradients in the liver's extracellular matrix chemistry from periportal to pericentral zones: influence on human hepatic progenitors. Tissue Eng Pt A 2008;14:59-70.

[200] Huet C, Pisselet C, Mandon-Pepin B, Monget P, Monniaux D. Extracellular matrix regulates ovine granulosa cell survival, proliferation and steroidogenesis: relationships between cell shape and function. The J Endocrinol 2001;169:347-60.

[201] Sellaro TL, Ravindra AK, Stolz DB, Badylak SF. Maintenance of hepatic sinusoidal endothelial cell phenotype in vitro using organ-specific extracellular matrix scaffolds. Tissue Eng 2007;13:2301-10.

[202] Zhang Y, He Y, Bharadwaj S, Hammam N, Carnagey K, Myers R, et al. Tissue-specific extracellular matrix coatings for the promotion of cell proliferation and maintenance of cell phenotype. Biomaterials 2009;30:4021-8.

[203] Stern MM, Myers RL, Hammam N, Stern KA, Eberli D, Kritchevsky SB, et al. The influence of extracellular matrix derived from skeletal muscle tissue on the proliferation and differentiation of myogenic progenitor cells ex vivo. Biomaterials 2009;30:2393-9.

[204] Singelyn JM, DeQuach JA, Seif-Naraghi SB, Littlefield RB, Schup-Magoffin PJ, Christman KL. Naturally derived myocardial matrix as an injectable scaffold for cardiac tissue engineering. Biomaterials 2009;30:5409-16.

[205] Badylak S, Obermiller J, Geddes L, Matheny R. Extracellular matrix for myocardial repair. Heart Surg Forum 2003;6:E20-6.

[206] Brown BN, Valentin JE, Stewart-Akers AM, McCabe GP, Badylak SF. Macrophage phenotype and remodeling outcomes in response to biologic scaffolds with and without a cellular component. Biomaterials 2009;30:1482-91.

[207] Tanaka J, Maeda N. Microglial ramification requires nondiffusible factors derived from astrocytes. Exp Neurol 1996;137:367-75.

[208] Davies JE, Huang C, Proschel C, Noble M, Mayer-Proschel M, Davies SJ. Astrocytes derived from glial-restricted precursors promote spinal cord repair. J Biol 2006;5:7.

[209] Davies JE, Proschel C, Zhang N, Noble M, Mayer-Proschel M, Davies SJ. Transplanted astrocytes derived from BMP- or CNTF-treated glial-restricted precursors have opposite effects on recovery and allodynia after spinal cord injury. J Biol 2008;7:24.

[210] Mulder MM, Hitchcock RW, Tresco PA. Skeletal myogenesis on elastomeric substrates: implications for tissue engineering. J Biomater Sci, Polym Ed 1998;9:731-48.

[211] Webb K, Li W, Hitchcock RW, Smeal RM, Gray SD, Tresco PA. Comparison of human fibroblast ECM-related gene expression on elastic three-

dimensional substrates relative to two-dimensional films of the same material. Biomaterials 2003;24:4681-90.

[212] Wolchok JC, Tresco PA. The isolation of cell derived extracellular matrix constructs using sacrificial open-cell foams. Biomaterials 2010;31:9595-603.

[213] Biran R, Noble MD, Tresco PA. Directed nerve outgrowth is enhanced by engineered glial substrates. Exp Neurol 2003;184:141-52.

[214] Campanelli JT, Sandrock RW, Wheatley W, Xue H, Zheng J, Liang F, et al. Expression profiling of human glial precursors. BMC Dev Biol 2008;8:102.

[215] McCarthy KD, de Vellis J. Preparation of separate astroglial and oligodendroglial cell cultures from rat cerebral tissue. J Cell Biol 1980;85:890-902.

[216] West PA, Bostrom MP, Torzilli PA, Camacho NP. Fourier transform infrared spectral analysis of degenerative cartilage: an infrared fiber optic probe and imaging study. Appl Spectrosc 2004;58:376-81.

[217] David-Vaudey E, Burghardt A, Keshari K, Brouchet A, Ries M, Majumdar S. Fourier Transform Infrared Imaging of focal lesions in human osteoarthritic cartilage. Eur Cell Mater 2005;10:51-60; discussion

[218] Bradbury EJ, Moon LD, Popat RJ, King VR, Bennett GS, Patel PN, et al. Chondroitinase ABC promotes functional recovery after spinal cord injury. Nature 2002;416:636-40.

[219] Kuffler DP, Sosa IJ, Reyes O. Schwann cell chondroitin sulfate proteoglycan inhibits dorsal root ganglion neuron neurite outgrowth and substrate specificity via a soma and not a growth cone mechanism. J Neurosci Res 2009;87:2863-71.

[220] Gopalakrishnan SM, Teusch N, Imhof C, Bakker MH, Schurdak M, Burns DJ, et al. Role of Rho kinase pathway in chondroitin sulfate proteoglycan-mediated inhibition of neurite outgrowth in PC12 cells. J Neurosci Res 2008;86:2214-26.

[221] Hynds DL, Snow DM. Neurite outgrowth inhibition by chondroitin sulfate proteoglycan: stalling/stopping exceeds turning in human neuroblastoma growth cones. Exp Neurol 1999;160:244-55.

[222] Yamada H, Fredette B, Shitara K, Hagihara K, Miura R, Ranscht B, et al. The brain chondroitin sulfate proteoglycan brevican associates with astrocytes ensheathing cerebellar glomeruli and inhibits neurite outgrowth from granule neurons. J Neurosci 1997;17:7784-95.

[223] Friedlander DR, Milev P, Karthikeyan L, Margolis RK, Margolis RU, Grumet M. The neuronal chondroitin sulfate proteoglycan neurocan binds to the neural

cell adhesion molecules Ng-CAM/L1/NILE and N-CAM, and inhibits neuronal adhesion and neurite outgrowth. J Cell Biol 1994;125:669-80.

[224] Snow DM, Letourneau PC. Neurite outgrowth on a step gradient of chondroitin sulfate proteoglycan (CS-PG). J Neurobiol 1992;23:322-36.

[225] Iijima N, Oohira A, Mori T, Kitabatake K, Kohsaka S. Core protein of chondroitin sulfate proteoglycan promotes neurite outgrowth from cultured neocortical neurons. J Neurochem 1991;56:706-8.

[226] Nakanishi K, Aono S, Hirano K, Kuroda Y, Ida M, Tokita Y, et al. Identification of neurite outgrowth-promoting domains of neuroglycan C, a brain-specific chondroitin sulfate proteoglycan, and involvement of phosphatidylinositol 3-kinase and protein kinase C signaling pathways in neuritogenesis. J Biol Chem 2006;281:24970-8.

[227] Faissner A, Clement A, Lochter A, Streit A, Mandl C, Schachner M. Isolation of a neural chondroitin sulfate proteoglycan with neurite outgrowth promoting properties. J Cell Biol 1994;126:783-99.

[228] Carrino DA, Caplan AI. The effects of beta-D-xyloside on the synthesis of proteoglycans by skeletal muscle: lack of effect on decorin and differential polymerization of core protein-bound and xyloside-linked chondroitin sulfate. Matrix Biol 1994;14:121-33.

[229] Fichard A, Verna JM, Olivares J, Saxod R. Involvement of a chondroitin sulfate proteoglycan in the avoidance of chick epidermis by dorsal root ganglia fibers: a study using beta-D-xyloside. Dev Biol 1991;148:1-9.

[230] Klein DJ, Brown DM, Moran A, Oegema TR, Jr., Platt JL. Chondroitin sulfate proteoglycan synthesis and reutilization of beta-D-xyloside-initiated chondroitin/dermatan sulfate glycosaminoglycans in fetal kidney branching morphogenesis. Dev Biol 1989;133:515-28.

[231] Rosamond S, Brown L, Gomez C, Braciale TJ, Schwartz BD. Xyloside inhibits synthesis of the class II-associated chondroitin sulfate proteoglycan and antigen presentation events. J Immunol 1987;139:1946-51.

[232] Stevens RL, Razin E, Austen KF, Hein A, Caulfield JP, Seno N, et al. Synthesis of chondroitin sulfate E glycosaminoglycan onto p-nitrophenyl-beta-D-xyloside and its localization to the secretory granules of rat serosal mast cells and mouse bone marrow-derived mast cells. J Biol Chem 1983;258:5977-84.

[233] Stearns K, Goetinck PF. Stimulation of chondroitin sulfate synthesis by beta-D-xyloside in chondrocytes of the proteoglycan deficient mutant nanomelia. J Cell Physio 1979;100:33-8.

[234] Okano T, Yamada N, Okuhara M, Sakai H, Sakurai Y. Mechanism of cell detachment from temperature-modulated, hydrophilic-hydrophobic polymer surfaces. Biomaterials 1995;16:297-303.

[235] Kushida A, Yamato M, Konno C, Kikuchi A, Sakurai Y, Okano T. Decrease in culture temperature releases monolayer endothelial cell sheets together with deposited fibronectin matrix from temperature-responsive culture surfaces. J Biomed Mater Res 1999;45:355-62.

[236] Shimizu T, Sekine H, Isoi Y, Yamato M, Kikuchi A, Okano T. Long-term survival and growth of pulsatile myocardial tissue grafts engineered by the layering of cardiomyocyte sheets. Tissue Eng 2006;12:499-507.

[237] Nishida K, Yamato M, Hayashida Y, Watanabe K, Yamamoto K, Adachi E, et al. Corneal reconstruction with tissue-engineered cell sheets composed of autologous oral mucosal epithelium. New Engl J Med 2004;351:1187-96.

[238] Lareu RR, Arsianti I, Subramhanya HK, Yanxian P, Raghunath M. In vitro enhancement of collagen matrix formation and crosslinking for applications in tissue engineering: a preliminary study. Tissue Eng 2007;13:385-91.

[239] Lareu RR, Subramhanya KH, Peng Y, Benny P, Chen C, Wang Z, et al. Collagen matrix deposition is dramatically enhanced in vitro when crowded with charged macromolecules: the biological relevance of the excluded volume effect. FEBS Lett 2007;581:2709-14.

[240] Lu H, Hoshiba T, Kawazoe N, Chen G. Autologous extracellular matrix scaffolds for tissue engineering. Biomaterials 2011;32:2489-99.

[241] Gorna K, Gogolewski S. Biodegradable porous polyurethane scaffolds for tissue repair and regeneration. J Biomed Mater Res A 2006;79:128-38.

[242] Montjovent MO, Mathieu L, Schmoekel H, Mark S, Bourban PE, Zambelli PY, et al. Repair of critical size defects in the rat cranium using ceramic-reinforced PLA scaffolds obtained by supercritical gas foaming. J Biomed Mater Res A 2007;83:41-51.

[243] Thorvaldsson A, Stenhamre H, Gatenholm P, Walkenstrom P. Electrospinning of highly porous scaffolds for cartilage regeneration. Biomacromolecules 2008;9:1044-9.

[244] Wen X, Tresco PA. Fabrication and characterization of permeable degradable poly(DL-lactide-co-glycolide) (PLGA) hollow fiber phase inversion membranes for use as nerve tract guidance channels. Biomaterials 2006;27:3800-9.

[245] Fujita H, Tanaka J, Toku K, Tateishi N, Suzuki Y, Matsuda S, et al. Effects of GM-CSF and ordinary supplements on the ramification of microglia in culture: a morphometrical study. Glia 1996;18:269-81.